

1-1-2010

Finite element analysis of a single conductor with a Stockbridge damper under Aeolian vibration

Oumar Barry
Ryerson University

Follow this and additional works at: <http://digitalcommons.ryerson.ca/dissertations>

 Part of the [Mechanical Engineering Commons](#)

Recommended Citation

Barry, Oumar, "Finite element analysis of a single conductor with a Stockbridge damper under Aeolian vibration" (2010). *Theses and dissertations*. Paper 826.

FINITE ELEMENT ANALYSIS OF A SINGLE CONDUCTOR WITH A STOCKBRIDGE DAMPER UNDER AEOLIAN VIBRATION

by

Oumar Barry

B.Eng., Mechanical Engineering

Ryerson University 2008

A thesis

presented to Ryerson University

in partial fulfillment of the
requirements for the degree of
Master of Applied Science
in the Program of
Mechanical Engineering

Toronto, Ontario, Canada, 2010

© Oumar Barry 2010

Author's Declaration

I hereby declare that I am the sole author of this thesis.

I authorize Ryerson University to lend this thesis to other institutions or individuals for the purpose of scholarly research.

Oumar Barry

I further authorize Ryerson University to reproduce this thesis by photocopying or by other means, in total or in part, at the request of other institutions or individuals for the purpose of scholarly research.

Oumar Barry

Abstract

FINITE ELEMENT ANALYSIS OF A SINGLE CONDUCTOR WITH A STOCKBRIDGE DAMPER UNDER AEOLIAN VIBRATION

© Oumar Barry, 2010
Master of Applied Science
in the Program of
Mechanical Engineering
Ryerson University

A finite element model is developed to predict the vibrational response of a single conductor with a Stockbridge damper. The mathematical model accounts for the two-way coupling between the conductor and the damper. A two-part numerical analysis using MATLAB is presented to simulate the response of the system. The first part deals with the vibration of the conductor without a damper. The results indicate that longer span conductors without dampers are susceptible to fatigue failure. In the second part, a damper is attached to the conductor and the effects of the excitation frequency, the damper mass, and the damper location are investigated. This investigation shows that the presence of a properly positioned damper on the conductor significantly reduces fatigue failure.

Acknowledgments

First of all, I would like to thank GOD for the blessings and gifts he has bestowed upon me. After all, it is because of his love and guidance that I made it so far in my life.

I am deeply grateful to my advisor Dr. Donatus Oguamanam for his guidance, unwavering support, constant encouragement, and insight throughout my work. I would also like to extend my sincere thanks to Dr. Der Chyan (Bill) Lin for influencing me in pursuing research in vibration and co-supervising my work.

I am extremely thankful to Hydro One, specially, Dr. Ibrahim Hathout and Mr. George Watt for their guidance in choosing this thesis topic. I am also very grateful to Dr. David Havard for sharing his expertise and resources.

I would also like to thank my parents for their love and support throughout my studies. Their encouragement convinced and motivated me to pursue graduate studies. Special gratitude goes to my love, Ry Long, and to all my friends.

I am very appreciative of the financial assistance from the Ontario Graduate Scholarship (OGS) and the National Science and Engineering Research Council Canada (NSERC) throughout my research.

Dedication

To my parents Amadou Barry and Kadiatou Bah

Table of Contents

Author's Declaration	ii
Abstract	iii
Acknowledgments	iv
Dedication	v
Table of Contents	vi
List of Figures	ix
List of Tables	xiii
Nomenclature	xiv
1 Introduction	1
1.1 Background	1
1.2 Motivation	3
1.3 Objective	5
1.4 Thesis Overview	5
2 Literature Review	7
2.1 Summary of Findings	7
2.2 Conductor	8
2.2.1 Materials and Construction	9

2.2.2	General Mathematical Model of The Conductor	9
2.2.3	Conductor Self-Damping	11
2.3	Damper	12
2.3.1	Types of Dampers	13
2.3.1.1	Stockbridge Dampers:	13
2.3.1.2	Torsional Dampers:	15
2.3.1.3	Hydro Quebec Dampers:	16
2.3.2	Dynamics of the Stockbridge Damper	17
2.3.3	Damper Location	19
2.3.4	Wind Modeling	20
2.4	Energy Balance Method	21
3	Mathematical Formulation	25
3.1	Modeling of the Conductor Without Damper	25
3.1.1	Conductor Equation of Motion	25
3.1.2	Theoretical Natural Frequency	28
3.2	Modeling the Conductor with a Stockbridge Damper	31
3.2.1	Position Vectors	32
3.2.2	Velocity Vectors	33
3.2.3	Kinetic Energy	34
3.2.4	Potential Energy	38
3.3	Finite Element Modeling	41
3.3.1	Finite Element Modeling of the Conductor Without Damper .	41
3.3.2	Finite Element Modeling of the Conductor With the Damper .	45
4	Dynamic of Single Conductor Without Damper	56
4.1	Description of the Matlab Codes	56
4.1.1	Modal Analysis	57
4.1.1.1	Description of the Conductor Characteristics	57
4.1.1.2	Methodology and Results	57
4.2	Forced Vibration Analysis	59

4.2.1	Conductors Selection and Transmission Lines Condition	59
4.2.2	Simulation Results	61
4.2.3	Bending Amplitude	65
5	Numerical Analysis of a Single Conductor Plus Dampers	66
5.1	Free Vibration Analysis	66
5.1.1	Validation of the Model	66
5.1.1.1	Simulation in ANSYS	67
5.1.1.2	Numerical Analysis in MATLAB	71
5.1.2	Effect of the Mass and the Location of the Damper on the Natural Frequency	72
5.2	Force Vibration Analysis	73
5.2.1	Response of the Conductor With One Damper	74
5.2.1.1	Effect of the Damper Mass	74
5.2.1.2	Effect of the Forcing Frequency on the Response	77
5.2.1.3	Effect of the Damper Location on the Response	80
5.3	Response of a Conductor with Two Dampers	87
6	Conclusion and Recommendation	90
6.1	Summary	90
6.1.1	Conclusion	94
6.2	Proposed Future Work	95
A	Appendix	96
A.1	ANSYS Vibration Modes	96
B	Appendix	101
B.1	MATLAB Codes	101
	Bibliography	114

List of Figures

1.1	Breakage of conductor on Hydro Quebec transmission lines [2].	2
1.2	Broken conductor strand and slippage of the messenger wire of the Stockbridge damper [6].	4
1.3	Sample of conductor and torsional damper failure on Cowal junction to Longwood TS in London [7].	4
2.1	Structure of a conductor [1].	9
2.2	Cross section of special conductors [1].	10
2.3	Stockbridge's original concrete block design [16].	14
2.4	Stockbridge damper [1].	15
2.5	Stockbridge damper cable [1].	15
2.6	Torsional damper [17].	16
2.7	Hydro Quebec damper [2].	17
3.1	Simply supported conductor.	25
3.2	A cut in the beam.	26
3.3	Conductor with damper diagram.	31
3.4	Close-up of damper.	32
3.5	Schematic of finite element of the conductor without damper.	41
3.6	Schematic of finite element of the conductor with damper.	45
4.1	Comparison of the analytical and experimental results.	59
4.2	Effect of the frequency on the vibration amplitude of 240/40 sq.mm conductor (20% RTS).	63

4.3	Effect of the frequency on the vibration amplitude of the 1840 kcmil conductor (20% RTS).	63
4.4	Normalized maximum displacement response of the 1840 Kcmil conductor for different span lengths.	64
4.5	Effect of the tension on the vibration amplitude at low forcing frequency.	64
4.6	Effect of tension on the amplitude of vibration at higher forcing frequency.	65
5.1	First mode of vibration of the conductor plus a damper.	68
5.2	Second mode of vibration of the conductor plus a damper.	68
5.3	Third mode of vibration of the conductor plus a damper.	69
5.4	Fifth mode with a closer look at the damper.	69
5.5	Tenth mode of vibration of the conductor plus a damper.	70
5.6	Fifteenth mode of vibration of the conductor plus a damper.	70
5.7	ANSYS and MATLAB natural frequencies comparison.	72
5.8	Effect of damper properties on the natural frequencies.	73
5.9	Effect of the total mass on the conductor response for $f = 9.53\text{Hz}$ and $L_d = 1.1\text{ m}$	76
5.10	Effect of the total damper mass on the damper response for $f = 9.53\text{ Hz}$ and $L_d = 1.1\text{ m}$	76
5.11	Normalized peak-to-peak displacement, as function of distance x_c along the conductor, for $f = 9.53\text{ Hz}$ and $L_d = 1.1\text{ m}$	77
5.12	Conductor peak-to-peak displacement, as function vibration frequency for $L_d = 0.898\text{ m}$	78
5.13	Damper peak-to-peak displacement, as function of vibration frequency for $L_d = 0.898\text{ m}$	78
5.14	Conductor peak-to-peak displacement, as function of vibration frequency for $L_d = 5\text{ m}$	79
5.15	Damper counterweights peak-to-peak displacement, as function of vibration frequency $L_d = 5\text{ m}$	79
5.16	Conductor peak-to-peak displacement as function of the damper location for $f = 9.53\text{ Hz}$	82

5.17	Conductor peak-to-peak displacement as function of the damper location for $f = 14.0$ Hz.	82
5.18	Conductor peak-to-peak displacement near span ends as function of the damper location, for $f = 14.0$ Hz.	83
5.19	Conductor peak-to-peak displacement as function of the damper location for $f = 41.45$ Hz.	83
5.20	Conductor peak-to-peak displacement near span ends as function of the damper location for $f = 41.45$ Hz.	84
5.21	Damper peak-to-peak displacement as function of the damper location for $f = 9.53$ Hz.	84
5.22	Damper peak-to-peak displacement as function of the damper location for $f = 14.0$ Hz.	85
5.23	Damper peak-to-peak displacement as function of the damper location for $f = 41.45$ Hz.	85
5.24	Conductor peak-to-peak displacement vs. damper location throughout the span length, for $f = 10.10$ Hz.	86
5.25	Damper peak-to-peak displacement vs. damper location throughout the span length, for $f = 10.10$ Hz.	86
5.26	Conductor peak-to-peak displacement vs. damper location for $f = 9.53$ Hz (2 Dampers).	88
5.27	Conductor peak-to-peak displacement vs. damper location for $f = 9.53$ Hz (2 Dampers).	88
5.28	Damper peak-to-peak displacement vs. damper location for $f = 9.53$ Hz (2 Dampers).	89
A.1	Fourth mode of vibration of the conductor plus a damper.	96
A.2	Fifth mode of vibration of the conductor plus a damper.	97
A.3	First mode of vibration with a closer look at the damper.	97
A.4	Second mode of vibration with a closer look at the damper.	98
A.5	Third mode of vibration with a closer look at the damper.	98
A.6	Fourth mode of vibration with a closer look at the damper.	99

A.7 Tenth mode of vibration with a closer look at the damper.	99
A.8 Fifteenth mode of vibration with a closer look at the damper.	100
A.9 Fifth mode of vibration of the conductor plus a damper.	100

List of Tables

2.1	Experimental conductor self-damping data.	12
4.1	Finite element (FE) and theoretical (exact) natural frequencies.	58
4.2	Experimental natural frequencies.	58
5.1	Comparison of MATLAB natural frequencies of the conductor with and without damper for $L = 13.375$ m and $T = 0$ N.	71
5.2	Comparison of ANSYS and MATLAB natural frequencies of the con- ductor with damper for $L = 13.375$ m and $T = 0$ N.	72

Nomenclature

A_c	Amplitude of vibration of the conductor
A	Conductor cross section area
$A_1, B_1, d_1, d_2, d_3, d_4$	Mathematical modeling constants
C_l	Lift coefficient
D	Conductor diameter
D_{cyl}	Cylinder diameter
E	Young's modulus
EI	Flexural rigidity
EI_{min}	Minimum value of flexural rigidity
EI_{max}	Maximum value of flexural rigidity
EI_{mr}	Right-side damper flexural rigidity
EI_{ml}	Left-side damper flexural rigidity
f	Vibration frequency (Hz)
F_l	Lift force
f_s	Strouhal frequency (Hz)
f_i	Natural frequency (Hz) for mode i
$f(x, t)$	Net transverse force per unit length
$F(t)$	Uniform wind force
F_0, F_1, F_1', F_2, F_3	Frames for conductor with damper modeling
g	Gravity constant
h	Length of the clamp plate (m)
K_{sd}	Constant of proportionality for conductor self-damping
K	Stiffness matrix

I	Inertia
L	Span length
L_d	Damper location
L_{gr}	Right-side messenger length
L_{gl}	Left-side messenger length
m	Conductor mass per unit length
m_{dr}	Right-end counterweight mass
m_{dl}	Left-end counterweight mass
M	Mass matrix
n	Mode number
P_c	Power dissipated by conductor self-damping
P_w	Power imparted by the wind
P_d	Power dissipated by the damper
q_c	Conductor nodal displacement matrix
q_{dr}	Right-side damper nodal displacement matrix
q_{dl}	Left-side damper nodal displacement matrix
\ddot{q}_c	Conductor nodal acceleration matrix
\ddot{q}_{dr}	Right-side damper nodal acceleration matrix
\ddot{q}_{dl}	Left-side damper nodal acceleration matrix
\vec{r}_c	Position vector of deformed differential of conductor
\vec{r}_c^*	Position vector of damper clamp
\vec{r}_{mr}	Position vector of right-end counterweight
\vec{r}_{ml}	Position vector of left-end counterweight
\vec{r}_{mmr}	Position vector of right-end messenger
\vec{r}_{mml}	Position vector of left-end messenger
$\dot{\vec{r}}_c$	Velocity vector of deformed differential of conductor
$\dot{\vec{r}}_c^*$	Velocity vector of damper clamp
$\dot{\vec{r}}_{mr}$	Velocity vector of right-end counterweight
$\dot{\vec{r}}_m$	Velocity vector of left-end counterweight
$\dot{\vec{r}}_{mmr}$	Velocity vector of right-end messenger

$\dot{\vec{r}}_{mml}$	Velocity vector of left-end messenger
s	Strouhal number
T	Tension in cable
T_c	Conductor kinetic energy
V	Wind speed
V_c	Conductor potential energy
V_{mr}	Right-side counterweight potential energy
V_{ml}	Left-side counterweight potential energy
V_{mmr}	Right-side messenger potential energy
V_{mml}	Left-side messenger potential energy
$w(x, t)$	Conductor transverse deformation
\dot{w}_c	Conductor velocity
w_{dr}	Right-side damper transverse deformation
\dot{w}_{dr}	Right-side damper velocity
w_{dr}^*	Right-side counterweight transverse deformation
w_{dl}	Left-side damper transverse deformation
\dot{w}_{dl}	Left-side damper velocity
w_{dl}^*	Left-side counterweight transverse deformation
W	Work done
Y	Normalized vibration displacement
y	Vibration displacement (mm)
ϵ	Strain
σ	Stress
ρ	Fluid density
ω_n	Natural frequency (rad)
ω	Forcing frequency (rad)
θ	Phase angle between response and wind force
θ_1	Rotation angle of frame F_1 with respect to F_0
θ_2	Rotation angle of frame F_2 with respect to F_0
θ_3	Rotation angle of frame F_3 with respect to F_0

ν	Kinematics viscosity
$\phi_1, \phi_2, \phi_3, \phi_4$	Hermite shape functions
ξ	Finite element field variable
δ	Variational
Ω	Driving frequency

Chapter 1

Introduction

1.1 Background

This thesis focuses on *Aeolian vibration* of transmission lines, the vibration caused by a wind force to a single conductor. This type of vibration, also known as wind-induced vibration, has a high frequency and small-amplitude motion, which arises from alternating forces caused by vortex shedding. Vortex shedding is associated with the flow of air across a bluff body. In addition to *Aeolian vibration*, there are two other types of conductor motion that are also caused by wind force. The first is galloping which is characterized by large amplitudes and low frequencies of vibration and the second is wake-induced oscillation. The latter is restricted to bundle conductor and it is distinguished by medium amplitude of vibration and higher natural frequencies, but its frequencies are usually lower than *Aeolian vibration* frequencies.

The term *Aeolian vibration* only refers to cases in which the fluid is air. Transmission lines are not the only structures that experience *Aeolian vibration*. Other examples of systems that also experience vortex induced vibration include bridges, heat exchangers, offshore platforms, and underwater cables. The frequency of *Aeolian vibration* ranges from 3 to 50 Hz and the wind speed ranges from 1 to 7 m/s. Usually the vibration of the conductor is not noticeable to an observer because the diameter of the conductor ranges from 6 to 50 mm, which in general is greater than the amplitude of vibration [1]. The maximum amplitude of vibration occurs at resonance and

this arises when some of the natural frequencies of the conductor coincide with the forcing frequency also known as Strouhal frequency.

Any type of vibration imperils the life of the structure. *Aeolian vibration* of transmission lines, if left uncontrolled, can result in serious accidents causing injuries and death, and/or considerable economical loss.

The vibration of the conductor produces alternating bending stresses and tensile stresses in the vicinity of the clamps. Eventually, this leads to fatigue damage of the conductor (Figure 1.1) in the form of broken strands in the outer layer, usually at the point of contact such as the suspension clamp.



Figure 1.1: Breakage of conductor on Hydro Quebec transmission lines [2].

Past field observations show that *Aeolian vibration* is most likely to occur in open fields and bodies of water (such as rivers, lakes, etc.) and usually in late evenings or early mornings. This is not surprising since light breezes occur during these periods. *Aeolian vibration* is sometimes detected when observing the conductor. However, this is not always the case; most often it is not noticeable until damage occurs. Examples of damages include breakage of conductor strands, insulator strings, and loosening of parts (i.e., suspension clamps).

Aeolian vibration can be controlled by dampers. The most popular damping device

used by transmission lines utilities is the Stockbridge damper. This damper is used to minimize or eliminate the vibration by reducing the induced strains of the conductor near the clamps to a safe level of $200 \mu\text{m}/\text{m}$. Past investigations have proven that a damper is more effective when it is designed to cover a wide range of frequencies and when it is appropriately positioned on the conductor [1][3][4].

1.2 Motivation

Power plants are generally located in remote areas, far from cities, and high voltage transmission lines are used to supply power to the cities. Power is transmitted through 151,848 km of overhead transmission and distribution lines across the province of Ontario [5]. The cost of installing these lines is very high, but it can be reduced by increasing the tension in the lines. However, increasing the tension increases the susceptibility of the conductor to vibration which eventually leads to fatigue failure. For safety reasons, transmission line engineers have imposed limitations on the maximum magnitude of the tension. This limitation is 20% and 25% of its rated tensile strength (RTS) in the summer and winter season, respectively [5].

Aeolian vibration is one of the most important of the many factors which limit the life of conductors of overhead lines by damaging the conductor through wire fatigue break usually at the suspension clamp where the maximum stress occurs. This failure could lead to power interruption, hence economic loss and personal discomfort. For instance, Hydro One residential and industrial customers in Sarnia experienced a blackout in 2005 due to the breakage of a conductor on the Sarnia-to-Scott transformer station. Later in 2008 another failure occurred on the transmission lines of the Cowal junction to Longwood TS in London. The damages to both lines were attributed to uncontrolled *Aeolian vibration*. Investigations concluded that the conductor tension was quite high (27% RTS) and the dampers on the lines were not effective. Some of the recommendations include adding more dampers to the transmission lines and positioning them at suitable locations [6]. Figures 1.2 and 1.3 show a broken conductor strand of the messenger wire of a Stockbridge damper, and a conductor and torsional

damper failure on Cowal junction to Longwood TS in London, respectively.



Figure 1.2: Broken conductor strand and slippage of the messenger wire of the Stockbridge damper [6].



Figure 1.3: Sample of conductor and torsional damper failure on Cowal junction to Longwood TS in London [7].

Furthermore, earlier in 1996, Manitoba Hydro Company reported wind damage of about 10 million USD due to the failure of 19 transmission towers [8]. At the CIGRE meeting in Toronto in 2009, *Electricité de France* reported the collapse of 45 towers

in the southern part of France due to *Aeolian vibration* [9].

In summary, the examples of transmission line and tower failures described in the previous paragraphs show that the problem with *Aeolian vibration* is still a challenge to transmission line engineers. Therefore, it is worthwhile to further study conductor vibration in order to predict the dynamic of the conductor, which will enable transmission line design engineers to justify increasing the tension in the conductor, and optimize the selection, number, and location of dampers.

1.3 Objective

As mentioned previously, this thesis is concerned with the *Aeolian vibration* of transmission lines. The main objective is to provide an alternate mathematical model of a single conductor vibration with Stockbridge dampers attached to it. Unlike the mathematical models found in the literature, this new model considers the two-way coupling between the conductor and the Stockbridge damper. A finite element code is written in MATLAB programming environment to assess the impact of the location of the damper and its properties on the system response.

1.4 Thesis Overview

The thesis is arranged in five chapters. The following chapter reviews the literature on *Aeolian vibration* of a single conductor. The modeling of the conductor and Stockbridge damper with external wind force excitation are presented. Also, the energy balance method is reviewed.

Chapter three presents the mathematical model of a single conductor with and without a damper. The equation of motion of a single conductor without a damper is first derived using Newton's law and the natural frequency equation was obtained through the separation of variable method. Furthermore, the kinetic and potential energies of the conductor and damper are obtained. The finite element method is employed to obtain the discretized governing equation.

In chapters four and five, a numerical analysis without and with a damper is presented, respectively. The validation of the mathematical model is established using the results in Ref. [10] and the results of the commercial finite element analysis software ANSYS.

Finally, chapter six contains a summary of the contributions of this research and suggestions for future work.

Chapter 2

Literature Review

2.1 Summary of Findings

A lot of research on *Aeolian vibration* was done in the 70's and 80's. Most authors agree that the location of the damper is crucial to the damper's effectiveness. In 1985 Nigol and Houston [11] studied the control of *Aeolian vibration* of a single conductor. They described the development of a general method for analyzing the combined response of various single conductor-damper arrangements, presented a summary of experimental verifications, and used the models to demonstrate optimum damping concepts.

Feldmann [12] from *Electricité de France* studied the effects of Stockbridge dampers using theoretical and experimental approach. He found that the Stockbridge dampers were remarkably efficient and observed that counterweights do not dissipate energy, but produce a coupling between the damper and the conductor, which makes them good disturbers of *Aeolian vibration* .

In 2000, Leblond and Hardy [13] described a probabilistic model for predicting *Aeolian vibration* of single conductors based on the conductor fatigue endurance limit approach and the linear fatigue damage accumulation. Both models are used to assess safe-design tensions. The endurance limit approach assesses conductor vibration severity by comparing the maximum bending stress amplitude with the fatigue endurance limit of the conductor at the suspension clamp. The cumulative damage

approach, however, assesses the severity of conductor vibration by calculating the anticipated lifetime of the conductor. Note that this approach requires S-N curves (cyclical stress, S, against the logarithmic scale of cycles to failure, N) for the different classes of conductors and some wind statistics. The authors determined that the safe-design tension is 11.1% RTS or $(H/w) = 811$ m and 13.2% RTS or $(H/w) = 961$ m for endurance limit and cumulative damage approach, respectively.

Another important paper on *Aeolian vibration* was published by Braga et al. [14]. The authors compared the values of fatigue endurance limits suggested by the IEEE (Institute of Electrical and Electronic Engineers), EPRI (Electric Power Research Institute), and CIGRE (International Council on Large Electric Systems). The IEEE and EPRI recommendations are based on the endurance limit approach, while the CIGRE recommendation is based on the cumulative damage approach.

An important finding from IEEE based on mechanical simulation is that the bending amplitude strain is related to the diameter of the last layer of the cable for a range of the stress loads from 15 to 30%. The IEEE posits that the value of $200 \mu\text{m}/\text{m}$ can meet the criteria of mechanical reliability.

EPRI provides a more elaborate formula for relating bending amplitude to the maximum cable strain and maximum bending stress. Due to the effect of the stiffness, the bending stress was found to be maximum in the region contiguous to the clamp.

2.2 Conductor

Aeolian vibration is characterized by the interaction of the conductor with the damper and wind force. The following section focuses on the construction and dynamic modeling of the conductor.

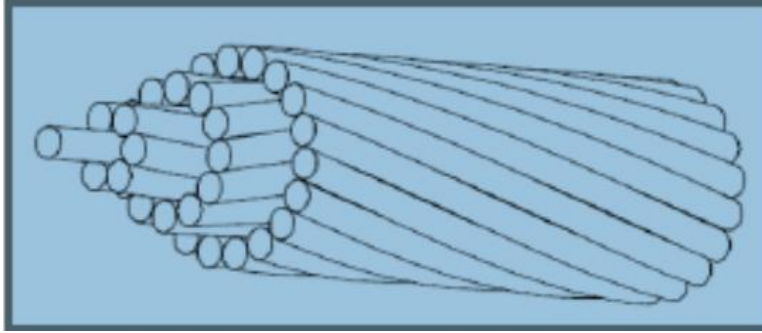


Figure 2.1: Structure of a conductor [1].

2.2.1 Materials and Construction

The conductor used in transmission lines are made of several layers of individual round wires packed tightly together in concentric counter-rotating helices (Figure 2.1 and 2.2). The most common conductor used in transmitting power is the aluminum conductor steel reinforced (ACSR) because of its high tensile-strength-to-weight ratio. Most of the power is transmitted through the aluminum outer layers. The inner layer of the ACSR is made of steel to increase the strength of the conductor. ACSR conductor is available for a wide range of steel alloys. The higher strength conductor is usually used for river crossing (longer span) since this requires more resistance.

Other types of conductors used in transmission lines include all aluminum conductor (AAC) and all aluminum alloy conductor (AAAC). AAC consists of a minimum purity of 99.5% of aluminium and is mostly used in urban areas and AAAC is made of aluminum-magnesium-silicon alloy and has an excellent corrosion resistance and strength-to-weight ratio.

2.2.2 General Mathematical Model of The Conductor

Claren and Diana [4] are among the first authors to develop a mathematical model of a single conductor. They showed that the physical model of the conductor is similar to an Euler-Bernoulli beam under the action of an axial load (design tension). If a

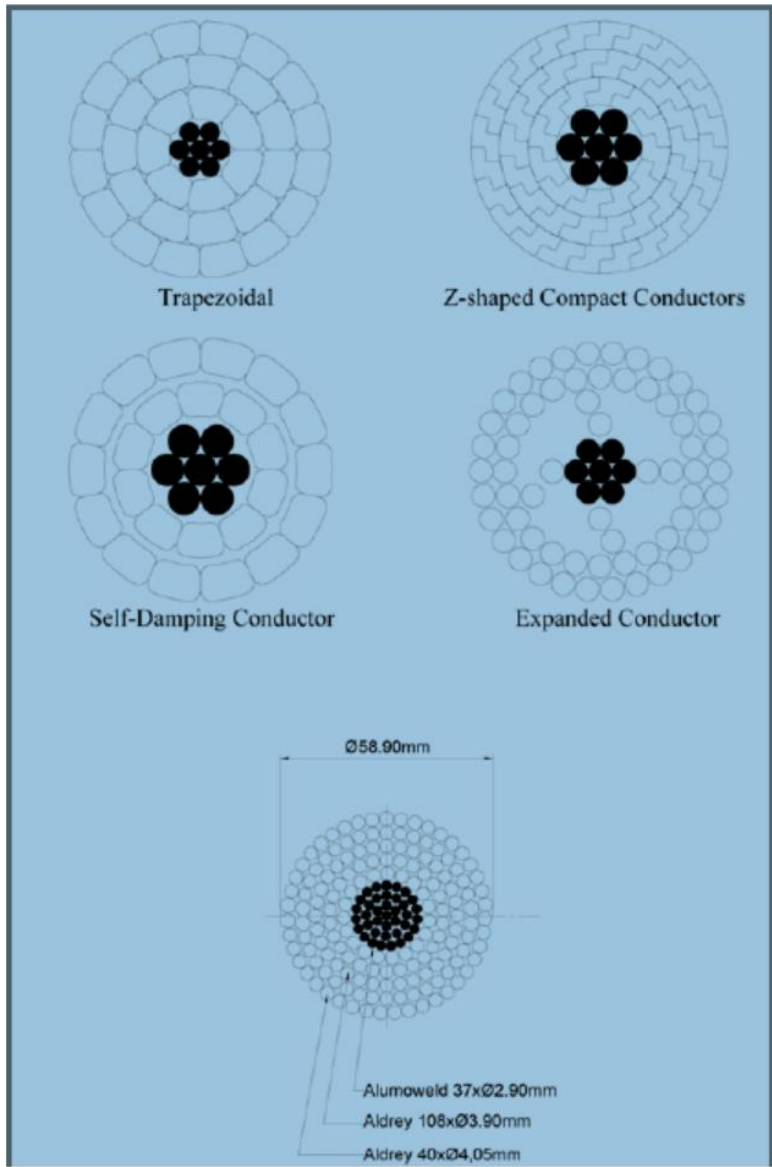


Figure 2.2: Cross section of special conductors [1].

constant flexural rigidity is assumed and damping is ignored, the equation of motion in the presence of the tension T may be written as:

$$EI \frac{\partial^4 w}{\partial x^4} - T \frac{\partial^2 w}{\partial x^2} = -m \frac{\partial^2 w}{\partial t^2} \quad (2.1)$$

where EI denotes the flexural rigidity, m is the mass per unit length, and w is the transverse displacement.

Using the mathematical model of Claren and Diana [4], a finite difference method was used by Dhotard and Ganesan [3] to examine the dynamics of a single conductor vibration with dampers. A close-form expression of the natural frequency of the conductor was determined for a simply supported end cable, a fixed end cable, and simply supported cable with flexural rigidity. The difference in the values of natural frequencies found in the simply supported end cable with and without flexural rigidity was less than 3%. The author hypothesized that for low frequency excitation (i.e., low wind speed), the location of the dampers have negligible effect on the strain. However, its effect is considerable in high frequencies excitation. Further, higher strains result with increasing length of the cable which calls for the use of more dampers. The effect of the number of dampers on the strain is negligible in low frequencies.

2.2.3 Conductor Self-Damping

When the conductor flexes the strands of the conductor slip against each other and frictional force is induced. This relative motion is the main source of conductor self-damping; a phenomenon when the conductor dissipates energy internally while vibrating. Conductor self-damping can be a major source of damping, especially for shorter span and lower tension system. Sometimes dampers are not needed for a short span with low tension because the conductor self-damping is able to dissipate most of the energy from the wind. However, when the tension of the conductor is increased, the strands tend to lock and slippage is reduced, thereby reducing the conductor self-damping. This explains why the conductor tension is usually kept low.

Past investigations on this topic have led to identification of empirical formulas

to predict the power dissipation of the conductor due to self-damping (P_{sd}). The relationship is in the exponential form and contains constants that depend on the conductor parameters [15]:

$$\frac{P_{sd}}{L} = \frac{K_{sd}Y^p f^u}{T^\nu} \quad (2.2)$$

where L is the span length, Y the amplitude of vibration corresponding to the natural frequency f , K_{sd} is a constant of proportionality, and T is the tension of the conductor. The parameters p , ν , and u are all exponential factors found experimentally as shown in Table 2.1.

The table below is a tabulation of the values of the constants obtained by different authors.

Table 2.1: Experimental conductor self-damping data.

Investigators	p	u	ν	L(m)
Tompkins et al.(1956)	2.3-2.6	5.0-6.0	1.9	36
Rawlins(1983)	2.2	5.4	-	36
Kraus and Hagedorn (1991)	2.47	5.38	2.8	30
Noiseux (1991)	2.44	5.63	2.76	63

Based on these values and the empirical formula, equation 2.2, it is obvious that the conductor dissipates less power when the tension is increased. This observation is in agreement with the remarks mentioned previously. Power dissipation increases in a scenario where the tension is constant while the frequency and amplitude of vibration are increasing.

2.3 Damper

The objective of vibration dampers is to eliminate or reduce *Aeolian vibration* by absorbing the energy from the wind in order to stabilize the motion of the conductor. Damping of the conductor is controlled by dampers that reduce the strain level to the safe strain limit of 200 $\mu\text{m}/\text{m}$ [14].

The effectiveness of a damper depends on its response within its frequency band.

Based on a rule of thumb, it was thought that dampers' locations will not coincide with a node provided the location is less than the loop length corresponding to the highest expected vibration frequency. This conclusion is realistic since conductor loop length increases with decreasing frequency.

2.3.1 Types of Dampers

There are various types of dampers, but the commonly used types in North America are the Stockbridge, torsional, and Hydro Quebec dampers.

2.3.1.1 Stockbridge Dampers:

Stockbridge damper, invented by George H. Stockbridge in 1925, is a dumbbell-shaped device with a mass at the ends of a short flexible cable or rod called the messenger cable. The damping mechanism is observed as vibrations of the conductor are transferred through the clamp to the messenger cable. The flexuring of the messenger causes slipping between its strands and consequently induces the weights at their ends to oscillate. By carefully choosing the parameters of the damper (such as the mass of the blocks, the length and the stiffness of the messenger), the impedance of the damper would coincide with that of the conductor. Thus, the energy imparted to the conductor from the wind is then greatly dissipated by the Stockbridge damper.

It is claimed in the Stockbridge damper patent that a shorter (i.e., 30 in or 75 cm) and very flexible messenger increases damping effectiveness. Furthermore, the use of concrete or similar material for the weights in lieu of metallic weight was recommended since no charging current is absorbed by concrete material [16]. This idea was quickly rejected because of the poor mechanical performance of concrete.

There are many types of Stockbridge dampers. The first Stockbridge damper as patented by George Stockbridge had a concrete block at each end of the messenger and it is shown in Figure 2.3.

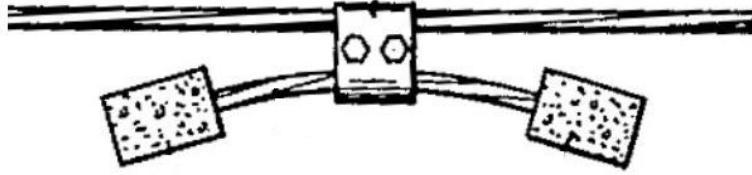


Figure 2.3: Stockbridge's original concrete block design [16].

Modern dampers use metal bell-shaped weights as shown in Figure 2.4. The bell is hollow and the damper cable is fixed internally to the distal end, which permits relative motion between the cable and damping weights. The modern Stockbridge damper has two types of dampers, the 2R damper and 4R damper. The former, 2R damper, is also known as the symmetric Stockbridge damper and it has identical weights and messengers at both ends. Given that this damper consists of two identical weights, the moment exerted by one is neutralized by the other. The 2R damper is characterized to possess two natural modes of vibration when the motion of the clamp is restricted to the vertical plane. The second type, 4R damper, also called the asymmetric Stockbridge damper, has weights and cable lengths that are different on both sides. Consequently, a resultant moment is induced by the unbalanced weights at the ends, which results in a wider range of frequencies that include four resonant frequencies.

The messenger of the Stockbridge damper as shown in Figure 2.5 is generally made of galvanized steel, but stainless steel is used in more polluted areas. Both materials result in the same damping capacity; however, stainless steel provides better fatigue resistance. The clamp is made of aluminum alloy in order to ensure that the weight is small enough to restrict its motion to the vertical plane for higher conductor vibration

frequencies. In the past, damper counterweights were made of zinc alloy, but due to the rise in cost of this material, forged steel weights or extruded steel rods are used instead.



Figure 2.4: Stockbridge damper [1].



Figure 2.5: Stockbridge damper cable [1].

2.3.1.2 Torsional Dampers:

Based on the patent of Buchanan and Tebo [17], a torsional damper consists of a sleeve carrying two weights and each weight is located at one end (Figure 2.6). The torsional damper is connected to the conductor through a rubber bushing. Each weight produces a moment since its center of gravity is eccentric to the axis of the

conductor and the combination of these two moments result in a torsional force at the end of the conductor. This torsional force being applied on the conductor converts the energy of the vibrating conductor into inter-strand frictional losses.

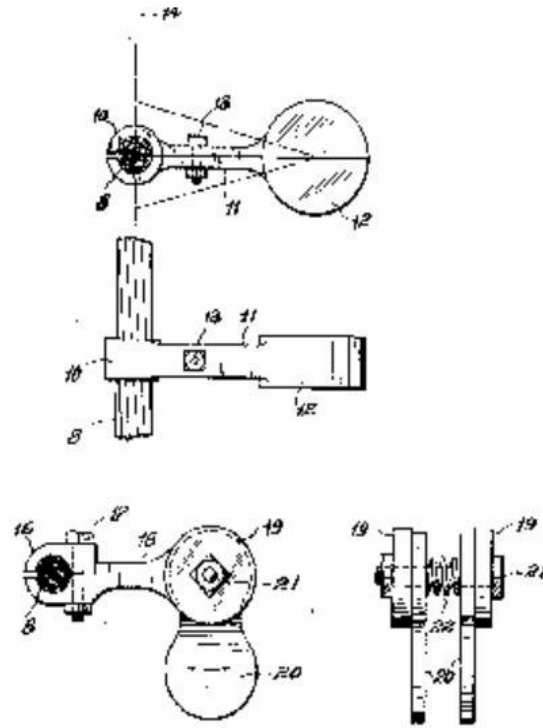


Figure 2.6: Torsional damper [17].

2.3.1.3 Hydro Quebec Dampers:

This type of damper is similar to the asymmetric Stockbridge damper except that the Hydro Quebec damper is devoid of a messenger and is not hollow in its counterweights (Figure 2.7). In this damper, the messenger wire is replaced by a dissipating and flexible element, which consists of an elastomeric cylinder.

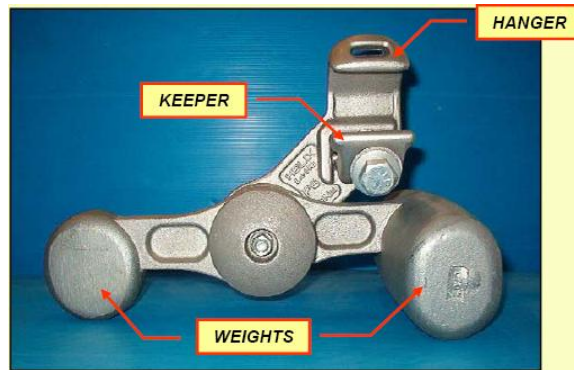


Figure 2.7: Hydro Quebec damper [2].

2.3.2 Dynamics of the Stockbridge Damper

Wagner et al. [18] studied the dynamic response of a Stockbridge damper. The authors assumed that the Stockbridge damper has a massless messenger and a rigid mass attached at the tip. Their assumption of a massless messenger is reasonable since the mass of the damper is much larger than the mass of the messenger. Only one mass was studied because the two masses of the damper were equal, so symmetry was used for simplification and the clamp motion was modeled as a base motion.

This paper presented the equation of motion of the Stockbridge damper (equation 2.3) and its response. Then, it validated the theoretical analysis through experiment. Both results were in agreement since their assumption of the Stockbridge damper being a two degree of freedom was justified experimentally by the existence of two distinct modes.

The equation of motion was given as:

$$M\ddot{x} + K\dot{x} + Cx = K\dot{y} + Cy \quad (2.3)$$

where M is the mass matrix, K is the damper coefficient matrix, C is the stiffness matrix, x is the vertical displacement of the messenger, and y is the displacement vector at the clamp.

Another investigation on the assessment of the dynamics of Stockbridge damper was conducted by Markiewicz [19]. In his paper, a method and a computational model were presented for the evaluation of the optimum dynamic characteristics of Stockbridge dampers to be mounted near tension insulator assemblies (dead end span). He suggested that Stockbridge dampers be designed so that their mechanical impedance matches as closely as possible to the determined optimum damper impedance for the cable to be protected. However, the optimum design is evaluated assuming that the cable is clamped at both ends. Therefore, the Stockbridge damper is only efficient for suspension span.

Futhermore, Krispin [20] outlined the advantage of a Stockbridge-type vibration damper with low mass clamp over a conventional Stockbridge vibration damper with bolted clamp. Using theoretical and experimental analysis, it was shown that the conventional Stockbridge has a shortcoming in damping high frequency vibrations of small diameter optical ground wires (OPGW) due to their high clamp mass. Therefore, *low clamp mass* dampers, compared to conventional *bolted clamp* dampers, improve power dissipation (damping performance) in the upper range frequencies.

Vecchiarelli [21] showed experimentally that the energy dissipated by a Stockbridge damper varies highly with the vibration frequency and the displacement amplitude of the damper clamp. The displacement of the damper clamp depends on the location of the damper. Therefore, the energy dissipated by the damper can be significantly affected by the positioning of the damper.

2.3.3 Damper Location

As mentioned earlier, the efficiency of the damper depends significantly on its positioning. A rule of thumb is used to determine this location and the most important point is to avoid positioning the damper at a node where the vibration amplitude is zero. Hence, the damper would not be efficient. This rule considers the location of the damper at a distance P (equation 2.4) between 70 and 80% of the loop length (equation 2.5), corresponding to the highest wind speed of 7 m/s [1].

$$P = 0.31d\sqrt{\frac{H}{w}} \quad (2.4)$$

where H and w are the conductor tension and mass per unit length, respectively. And d denotes the diameter of the conductor.

$$l = \frac{2.703}{V_w}d\sqrt{\frac{H}{w}} \quad (2.5)$$

where l = loop length (m), V_w = wind velocity (m/s), d = conductor diameter (m), w = conductor mass per meter (kg/m)

Nigol and Houston [11] established optimum locations of dampers and made recommendations to never place dampers at any point of symmetry along the conductor (i.e, 1/4, 1/3, 1/2, etc.). Otherwise the dampers fail to provide vibration protection at every 4th, 3rd, and 2nd harmonic [11]. One damper can be placed at a distance x_1 (1.2 to 1.8 m) for frequencies of 40-50 Hz and for normal design tensions. For longer span and/or higher tension, two dampers shall be used at distances x_1 (2.4 to 3.6 m) and x_2 (1.0 to 2.2 m) from the two terminals. When more than one damper is used the ratio x_2/x_1 shall be 0.4 or 0.6.

Dhotard, and Ganesan [3] showed that the amplitude of vibration does not depend on the cable length, but only on the location of the damper. An increase in the number of dampers leads to an increase in the displacement in the major frequency range. The authors also compared asymmetric and symmetric dampers. They concluded that unlike symmetric dampers, asymmetric dampers create a resultant moment due to the inequality or unbalance of its two masses, but this moment has negligible effect

on vibration of the cable.

2.3.4 Wind Modeling

Strouhal and Von Karman¹ are the first authors to investigate uniform flow of air across a rigid cylinder. The nature of the flow depends on the Reynolds number, which is defined as the ratio of inertial forces to viscous forces (equation 2.6). With respect to *Aeolian vibration*, Reynolds number varies between 2700 and 14000 [22].

$$Re = \frac{VD}{\nu} \quad (2.6)$$

where V is the wind velocity, D is the diameter of the conductor and ν is the kinematic viscosity of the fluid.

Aeolian vibration is caused by alternating vortices. As the vortices are shed from the surface of the conductor normal to the wind, they cause a resultant force that acts in the transverse direction. This force is periodic with a frequency f_s , which is related to the diameter of the conductor and the wind velocity as follows:

$$f_s = \frac{sV}{D} \quad (2.7)$$

where s is the Strouhal number and it varies from 0.15 to 0.25. In general the average Strouhal value is taken as 0.2. It is noted that the conductor becomes very excited as the Strouhal frequency approaches some of its natural frequencies and this phenomena is called resonance.

While studying the lift force that acts on a rigid cylinder during vibration, Diana and Falco [23] found that this force behaves similarly to the vibration response since they are both harmonic at steady state. This conclusion was verified by Bishop and Hassan [24] and by Bearman and Currie [25]. All the authors agreed that during resonance the lift force leads the displacement by a phase angle ranging from 0-180

¹Strouhal V. Strouhal. 1878. *Über Eine besondere Art der Tonerregung*. Ann. Phys. und Chemie, New Senes, Vol. 5, pp. 216-251.

degrees. Both the lift force and the cylinder response are represented as follows:

$$F(t) = F_l \sin(\omega t + \theta) \quad (2.8)$$

$$X(t) = A_c \sin(\omega t) \quad (2.9)$$

where F_l is the lift force and ω is the forcing frequency in rad/s. θ is the phase angle between the response $x(t)$ and wind force $F(t)$. It should be noted that the forcing frequency is the Strouhal frequency.

The lift force is defined as follows:

$$F_l = \frac{1}{2} \rho C_l D L V^2 \quad (2.10)$$

where D and L are the diameter and length of the cylinder, respectively. V and ρ is the velocity and density of the fluid, respectively. C_l is the lift coefficient.

Griffin and Koopmann [26] showed experimentally that this lift coefficient depends on the ratio of the maximum amplitude of vibration to the diameter of a rigid cylinder (A_c/D_{cyl}). Their conclusion was that a maximum lift of 0.55 experienced a maximum vibration amplitude of 0.55 diameters, peak-to-peak. And any cylinder with a maximum amplitude above or below this value experienced lift coefficient C_l of 0.28-0.33.

2.4 Energy Balance Method

The energy balance method is the most popular concept used to predict the vibration of transmission lines. This method states that the energy transferred by the wind to the conductor is dissipated by the conductor self-damping and the dampers. The mathematical interpretation is given below:

$$P_w = P_d + P_c \quad (2.11)$$

where P_w is the wind power, P_d is power dissipated in the damper, and P_c is power dissipated in the conductor.

Most researches on *Aeolian vibration* used the power method to solve for the amplitude of vibration. Kraus and Hagedorn [27] studied the level of vibration using the energy balance method and compared the results to those obtained from a wind tunnel experiment. It should be noted that the energy balance method is only valid when the conductor is vibrating at resonance. Therefore, the amplitude of vibration is maximum and it is determined when the forcing frequency is equal to the natural frequency of the conductor. Furthermore, this method ignores the flexural rigidity of the conductor and determines the wind power input and the power dissipated by the damper in terms of the antinodal displacement amplitude.

The power dissipated in the conductor is given as:

$$P_c = K_2 f^{(n+m)} \left[\frac{A}{D} \right]^m L \quad (2.12)$$

where K_2 , n , m are constants that are determined through experiment. A , D , and L , are the maximum amplitude of vibration, diameter of the conductor, and the span length, respectively.

From laboratory measurements on a rigid cylinder, the wind input is given by:

$$P_w = L f^3 D^4 F \left(\frac{A}{D} \right) \quad (2.13)$$

where $F(A/D)$ depends on the maximum amplitude of vibration and the diameter of the conductor.

The power dissipated by the damper is given in Ref. [3] as:

$$P_d = \frac{1}{2} F_a U_a \Omega \sin(\phi) \quad (2.14)$$

where F_a is the force transmitted to the cable by the damper. U_a is the maximum amplitude, so it is the same as A_c in equation 2.9. ϕ denotes the phase angle and Ω represents the driving frequency.

A well established energy balance method was implemented by Verma and Hagedorn [28] to optimize the position of Stockbridge dampers along the span. It was analytically determined that two successive dampers should be placed apart at a maximum distance of 1 m. This ensures that both dampers will not be simultaneously located on nodes for any natural frequency of the system under 50 Hz. It was also observed that the maximum strain and the amplitude of vibration are kept within the permissible limits when dampers are kept in the range of 0.22l to 0.25l% of the loop length.

Agamenon et al. [29] also developed a dynamic model of *Aeolian vibration* to predict the amplitude of steady-state motion of the conductor based on the energy balance principle and a direct method for solving the resulting time-dependent Navier-Stokes equation. They showed that numerical simulation will be more realistic if a correlation between the tension and equivalent damping of the conductor can be obtained.

The energy balance method is a very easy concept to implement with little computation once the combination of the dynamics of the conductor, damper, and wind is determined. However this method may lead to significant erroneous results because of its assumptions. One of the weaknesses of the energy method is the assumption of negligible flexural rigidity. This implies that the conductor is modeled as a string instead of a tensile beam. Consequently, it can considerably influence the amplitude of vibration for larger conductors which affects the bending stress at the clamps. Also, the maximum amplitude of vibration is always overestimated because of the negligible stiffness.

Another weakness is that the energy balance method can only be implemented at resonance. While the amplitude of vibration is maximum at resonance, it is desirable to know how non-resonant frequencies influence the conductor vibration. Further, modeling the Stockbridge damper as a lump mass imparts a vertical inertia force at the attachment of the damper. In reality, however, this force is not always vertical, but remains normal to the messenger cable. As it can be inferred from equation 2.14, the flexural rigidity of the messenger is neglected even though its inclusion can alter

the overall natural frequencies and mode shapes of the system. Hence, the scope for assessing the mechanical behaviour of the damper is beyond the capability of the energy balance method.

Chapter 3

Mathematical Formulation

3.1 Modeling of the Conductor Without Damper

3.1.1 Conductor Equation of Motion

The conductor is modeled as a simply supported beam with tension. The wind force per unit length $f(x, t)$ is assumed to be perpendicular to the conductor (Figure 3.1).

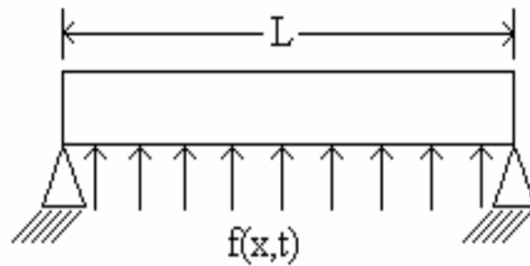


Figure 3.1: Simply supported conductor.

The following assumptions are employed in deriving the equation of motion of the conductor (equation 3.6):

1. Euler-Bernoulli beam theory is applicable since the ratio of the conductor length to its diameter is very small (L/D is greater than 20).

2. The mass per unit length, m , is uniform across the conductor span since its diameter is constant throughout the span.
3. The tension, T , is assumed to be uniform across the span for simplicity. It is known in practice that the tension varies from a maximum at the clamp ends to a minimum in the middle of the conductor. However, the variation is usually negligible for smaller and moderate span lengths.
4. The slope, θ , is very small since the amplitude of vibration is less than the conductor diameter. Hence the theory of small deformation is applicable.
5. The flexural rigidity, EI , is constant. This assumption is for mathematical simplicity because the flexural rigidity varies with the distance along the conductor. However, for most conductors the flexural rigidity is very small. Therefore, it does not have a significant effect on the conductor and hence the assumption of uniformity of the flexural rigidity is reasonable.

Figure 3.2 depicts the free-body diagram of a differential element of the conductor with original length dx , where $w(x, t)$ denote the transverse deflection. $V(x, t)$, $M(x, t)$, and $T(x, t)$ denote the shear force, bending moment, and the tension at the left-end of the conductor element, respectively. $V(x + dx, t)$, $M(x + dx, t)$, and $T(x + dx, t)$ are the shear force, bending moment, and tension of the element on the right-end of the element, respectively.

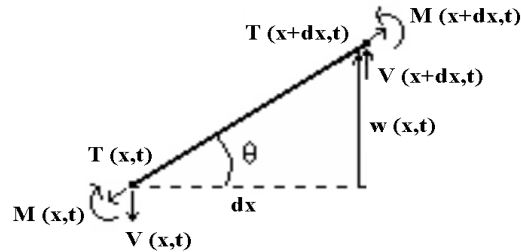


Figure 3.2: A cut in the beam.

Since the Euler-Bernoulli beam theory is applicable, the shear force, moment, and

slope are given by:

$$V(x, t) = -EI \frac{\partial^3 w}{\partial x^3} \quad M(x, t) = EI \frac{\partial^2 w}{\partial x^2} \quad \theta = \frac{\partial w}{\partial x} \quad (3.1)$$

Applying Newton's law of motion, $\sum F = ma$ leads to the following:

$$V(x + dx, t) + T(x + dx, t) \sin(\theta + d\theta) - V(x, t) - T(x, t) \sin \theta + f(x, t)dx = \rho A dx \frac{\partial^2 w}{\partial t^2} \quad (3.2)$$

Recall Taylor Series:

$$g(x + dx) = g(x) + (dx)g'(x) + (dx)^2 g''(x) \dots$$

where $g' = \frac{dg}{dx}$ and $g'' = \frac{d^2g}{dx^2}$.

Using the Taylor series expression, equation 3.2 can be written as:

$$\frac{dV(x, t)}{dx} + \frac{d(T(x, t) \sin \theta)}{dx} + f(x, t) = \rho A \frac{\partial^2 w}{\partial t^2} \quad (3.3)$$

Observe that $\rho A = m$, the mass per unit length, where A is the cross-sectional area and ρ is the density of the conductor.

Since θ is small $\Rightarrow \sin \theta \cong \theta$. Substituting this into equation 3.3 leads to:

$$\frac{dV(x, t)}{dx} + \frac{d(T(x, t)\theta)}{dx} + f(x, t) = m \frac{\partial^2 w}{\partial t^2} \quad (3.4)$$

For a constant tension in the beam, equation 3.4 becomes:

$$\frac{dV(x, t)}{dx} + T \frac{d\theta}{dx} + f(x, t) = m \frac{\partial^2 w}{\partial t^2} \quad (3.5)$$

Substituting (3.1) into (3.5) and multiplying (3.5) by (-1) leads to the fourth order differential equation below:

$$\Rightarrow EI \frac{\partial^4 w}{\partial x^4} - T \frac{\partial^2 w}{\partial x^2} - f(x, t) = -m \frac{\partial^2 w}{\partial t^2} \quad (3.6)$$

Equation 3.6 is the equation of motion of the conductor without dampers under *Aeolian vibration*.

3.1.2 Theoretical Natural Frequency

The natural frequency of the conductor is determined from a free vibration analysis. Assume that the transverse deformation $w(x, t)$ can be written as:

$$w(x, t) = y(t)g(x) \quad (3.7)$$

where

$$y(t) = A_1 \sin(\omega t + \phi) \quad (3.8)$$

and

$$g(x) = \phi e^{zx} \quad (3.9)$$

Substituting (3.8) and (3.9) into (3.7) yields:

$$\begin{aligned} y(t)EI \frac{d^4 g(x)}{dx^4} + mg(x) \frac{d^2 y(t)}{dt^2} - Ty(t) \frac{d^2 g(x)}{dx^2} &= 0 \\ \Rightarrow \frac{1}{mg(x)} \left[EI \frac{d^4 g(x)}{dx^4} - T \frac{d^2 g(x)}{dx^2} \right] &= -\frac{1}{y(t)} \frac{d^2 y(t)}{dt^2} \end{aligned} \quad (3.10)$$

Since the term on the right and the left side depend on t and x , respectively, both must equal a constant. Let the constant be ω^2 .

$$\begin{aligned} \frac{1}{y(t)} \frac{d^2 y(t)}{dt^2} &= \omega^2 \\ \Rightarrow \frac{d^2 y(t)}{dt^2} &= -y(t)\omega^2 \end{aligned}$$

$$y(t) = A_1 \sin \omega t + B_1 \sin \omega t$$

$$y(0) = 0 \rightarrow B_1 = 0$$

$$y(t) = A_1 \sin(\omega t)$$

Also:

$$\frac{1}{mg(x)} \left[EI \frac{d^4 g(x)}{dx^4} - T \frac{d^2 g(x)}{dx^2} \right] = \omega^2$$

Assuming $g(x) = \phi e^{zx}$: The above equation can be written as:

$$EI \phi z^4 e^{zx} - T \phi z^2 e^{zx} - \omega^2 m \phi e^{zx} = 0$$

$$\Rightarrow EI z^4 - T z^2 - \omega^2 m = 0$$

Hence.

$$z_{1,2}^2 = \frac{T \pm \sqrt{T^2 + 4\omega^4 m EI}}{2EI}$$

The above equation leads to four roots (two real $z_{1,2}$ and two imaginary $z_{3,4}$)

$$z_{1,2} = \pm \sqrt{\frac{-T \pm \sqrt{T^2 + 4\omega^4 m EI}}{2EI}} \quad (3.11)$$

$$z_{3,4} = \pm i \sqrt{\frac{T \pm \sqrt{T^2 + 4\omega^4 m EI}}{2EI}} \quad (3.12)$$

Alternatively, $g(x)$ can be written as follows:

$$g(x) = \phi e^{zx} = d_1 \sinh zx + d_2 \sin zx + d_3 \cosh zx + d_4 \cos zx$$

$$g'(x) = d_1 z \cosh zx + d_2 z \cos zx + d_3 z \sinh zx - d_4 z \sin zx$$

$$g''(x) = d_1 z^2 \sinh zx - d_2 z^2 \sin zx + d_3 z^2 \cosh zx - d_4 z^2 \cos zx$$

The pin-pin boundary conditions are that, there are no displacements and no moments at both ends, hence $g(0) = 0$, $g(L) = 0$, $g''(0) = 0$, and $g''(L) = 0$

Applying the boundary conditions yield:

$$\begin{bmatrix} 0 & 0 & 1 & 1 \\ \sinh zL & \sin zL & \cosh zL & \cos zL \\ 0 & 0 & z^2 & z^2 \\ z^2 \sinh zL & -z^2 \sin zL & z^2 \cosh zL & -z^2 \cos zL \end{bmatrix} \begin{bmatrix} d_1 \\ d_2 \\ d_3 \\ d_4 \end{bmatrix} = \begin{bmatrix} 0 \\ 0 \\ 0 \\ 0 \end{bmatrix}$$

Since d_1 , d_2 , d_3 , and d_4 are nonzero, hence the matrix must be singular and therefore its determinant is zero. The determinant of this matrix is called the characteristic equation and the roots of the equation are the natural frequencies, which correspond to the eigenvalues. Equating the determinant to zero implies that

$$\Rightarrow 2z^2 \sin zL \sinh zL = 0$$

Hence the characteristic equation is $\sin zL \sinh zL = 0$.

$$\text{For } \sin zL = 0 \quad \Rightarrow z = \frac{n\pi}{L} \quad (3.13)$$

Equating equation 3.13 to equation 3.11 yields:

$$\frac{n\pi}{L} = \sqrt{\frac{T \pm \sqrt{T^2 + 4\omega^2 mEI}}{2EI}}$$

Squaring both sides and rearranging leads to:

$$\begin{aligned} \left(\frac{n\pi}{L}\right)^2 &= \frac{T \pm \sqrt{-T^2 + 4\omega^2 mEI}}{2EI} \\ \Rightarrow \left(\frac{n\pi}{L}\right)^4 + \frac{T^2}{4(EI)^2} + T \left(\frac{n\pi}{L}\right)^2 \frac{T}{EI} &= \frac{T^2}{2(EI)^2} + \frac{4\omega^2 mEI}{4(EI)^2} \\ \Rightarrow \left(\frac{n\pi}{L}\right)^4 + \left(\frac{n\pi}{L}\right)^2 \frac{T}{EI} &= \frac{\omega^2 m}{EI} \end{aligned}$$

and

$$\omega_n = \frac{n\pi}{L} \sqrt{\frac{T}{m} + \left(\frac{n\pi}{L}\right)^2 \frac{EI}{m}} \quad (3.14)$$

Equation 3.14 is the theoretical natural frequency of a conductor without a damper.

3.2 Modeling the Conductor with a Stockbridge Damper

All the assumptions made in section 3.1 are also applicable in this section. The cable of the damper (messenger) is assumed to behave as an Euler-Bernoulli beam. The clamp is assumed to be rigid and fixed to the conductor, which means that the height, h (length of the clamp plate) is always perpendicular to the conductor at its point of attachment. Figures 3.3 and 3.4 show the positioning of all the points of interest for the derivation of kinetic energy and potential energy. The positioning of the counterweight of the damper on the right side is shown in Figure 3.4. That for the weight on the left-end is omitted for brevity, but both are similar except that the subscript r which denotes the right-side is replaced by l to denote the left-side.

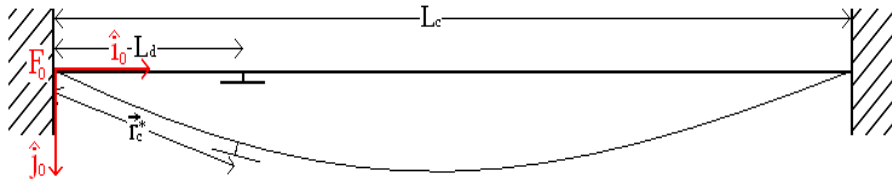


Figure 3.3: Conductor with damper diagram.

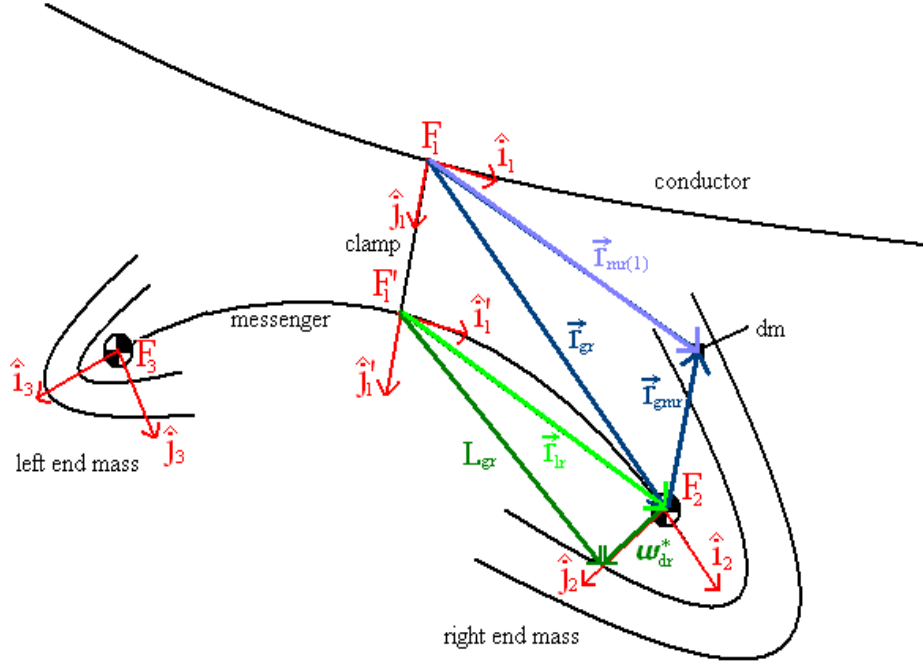


Figure 3.4: Close-up of damper.

3.2.1 Position Vectors

The position vectors of the conductor, the location of the damper, the mass of the damper, and the messenger are described below: The position vector of a deformed differential element of the conductor is written as:

$$\vec{r}_c(x, t) = x\hat{i}_0 + w(x, t)\hat{j}_0 \quad (3.15)$$

If the point of attachment of the damper is $x = L_d$, then

$$\vec{r}_c^* = L_d\hat{i}_0 + w(L_d, t)\hat{j}_0 \quad (3.16)$$

The position vector of the right-end counterweight with respect to the reference frame F_0 is described as:

$$\vec{r}_{mr(0)} = \vec{r}_{mr(1)} + \vec{r}_c^* \quad (3.17)$$

where

$$\begin{aligned}\vec{r}_{mr(1)} &= \vec{r}_{gr} + \vec{r}_{gmr} \\ \vec{r}_{gr} &= \vec{r}_h + \vec{r}_{lr} \\ \vec{r}_{lr} &= L_{gr}\hat{i}_1 + w_{dr}^*\hat{j}_1 \\ \vec{r}_{ll} &= -L_{gl}\hat{i}_1 + w_{dl}^*\hat{j}_1\end{aligned}$$

Note that $\vec{r}_{mr(1)}$ represents the position of the right-end counterweight with respect to frame 1, F_1 . Also, from Figure 3.4 it can be seen that \vec{r}_{lr} is the distance from frame 1, F_1 , to frame 2, F_2 , along \hat{i}_1 and that similarly \vec{r}_{ll} is from frame 1, F_1 , to frame 2, F_2 . The position vector $\vec{r}_{mr(0)}$ becomes:

$$\vec{r}_{mr(0)} = \vec{r}_{gr} + \vec{r}_{gmr} + \vec{r}_c^* \quad (3.18)$$

Similarly, the position vector of the counterweight on the left-side is as follows:

$$\vec{r}_{ml(0)} = \vec{r}_{gl} + \vec{r}_{gml} + \vec{r}_c^* \quad (3.19)$$

The position vectors of the messenger on the right and left sides are:

$$\vec{r}_{mmr} = \vec{r}_c^* + \vec{r}_h + x_{mm}\hat{i}_1 + w_{dr}(x_{mm}, t)\hat{j}_1 \quad (3.20)$$

$$\vec{r}_{mml} = \vec{r}_c^* + \vec{r}_h + x_{mm}\hat{i}_1 + w_{dl}(x_{mm}, t)\hat{j}_1 \quad (3.21)$$

3.2.2 Velocity Vectors

The velocity vectors are found by taking the derivative of the position vectors with respect to time.

$$\dot{\vec{r}}_c = \dot{w}_c(x, t)\hat{j}_0 \quad (3.22)$$

$$\dot{\vec{r}}_c^* = \dot{w}_c^*(x, t)\hat{j}_0 \quad (3.23)$$

Note that $\dot{\vec{r}}_h$ is the relative velocity vector of the clamp and it is defined as:

$$\dot{\vec{r}}_h = \dot{\theta}_1 \hat{k} \times h \hat{j}_1 = \dot{\theta}_1 h \hat{i}_1$$

where θ_1 is the rotation angle of frame 1, F_1 , with respect to F_0 . Hence the velocity vectors are expressed as:

$$\dot{\vec{r}}_{lr} = L_{gr} \dot{\theta}_1 \hat{j}_1 + \dot{w}_{dr}^* \hat{j}_1 + w_{dr}^* \dot{\theta}_1$$

$$\dot{\vec{r}}_{ll} = -L_{gl} \dot{\theta}_1 \hat{j}_1 + \dot{w}_{dl}^* \hat{j}_1 + w_{dl}^* \dot{\theta}_1$$

$$\dot{\vec{r}}_{gmr} = \vec{\omega}_r \times \vec{r}_{gmr}$$

$$\dot{\vec{r}}_{gml} = \vec{\omega}_l \times \vec{r}_{gml}$$

Using the equations above, the velocity vectors of the right and left side of the counterweights are as follows:

$$\dot{\vec{r}}_{mr(1)} = \dot{\theta}_1 h \hat{i}_1 + L_{gr} \dot{\theta}_1 \hat{j}_1 + \dot{w}_{dr}^* \hat{j}_1 + w_{dr}^* \dot{\theta}_1 + \vec{\omega}_r \times \vec{r}_{gmr} \quad (3.24)$$

$$\dot{\vec{r}}_{ml(1)} = \dot{\theta}_1 h \hat{i}_1 - L_{gl} \dot{\theta}_1 \hat{j}_1 + \dot{w}_{dl}^* \hat{j}_1 + w_{dl}^* \dot{\theta}_1 + \vec{\omega}_l \times \vec{r}_{gml} \quad (3.25)$$

$$\text{where } \vec{\omega}_r = (\dot{\theta}_1 + \dot{\theta}_2) \hat{k}$$

$$\text{and } \vec{\omega}_l = (\dot{\theta}_1 + \dot{\theta}_3) \hat{k}$$

Note that θ_2 and θ_3 are the rotation angles of frames F_2 and F_3 with respect to F_0 , respectively.

3.2.3 Kinetic Energy

The kinetic energy (KE) of the cable is expressed as follows:

$$T_c = \frac{1}{2} \int_m \dot{\vec{r}}_c \cdot \dot{\vec{r}}_c dm \quad (3.26)$$

Note that the velocity of the conductor is expressed with respect to the reference frame, F_0 . Therefore, the KE of the conductor becomes:

$$T_c = \frac{(\rho A)_c}{2} \int_0^{L_c} \dot{w}_c \cdot \dot{w}_c dx \quad (3.27)$$

The KE of the right-end mass is defined as:

$$T_{mr} = \frac{1}{2} \int_m \dot{\vec{r}}_{mr(o)} \cdot \dot{\vec{r}}_{mr(o)} dm \quad (3.28)$$

where $\dot{\vec{r}}_{mr(o)} \cdot \dot{\vec{r}}_{mr(o)}$.

$$\begin{aligned} \dot{\vec{r}}_{mr(o)} \cdot \dot{\vec{r}}_{mr(o)} &= (\dot{\vec{r}}_c^* + \dot{\vec{r}}_{mr(1)}) \cdot (\dot{\vec{r}}_c^* + \dot{\vec{r}}_{mr(1)}) \\ &= \dot{\vec{r}}_c^* \cdot \dot{\vec{r}}_c^* + 2\dot{\vec{r}}_c^* \cdot \dot{\vec{r}}_{mr(1)} + \dot{\vec{r}}_{mr(1)} \cdot \dot{\vec{r}}_{mr(1)} \end{aligned}$$

where $\dot{\vec{r}}_c^* \cdot \dot{\vec{r}}_c^* = \dot{w}_c^{*2}$ and

$$\begin{aligned} \dot{\vec{r}}_{mr(1)} \cdot \dot{\vec{r}}_{mr(1)} &= (\dot{\theta}_1 h)^2 + (L_{gr} \dot{\theta}_1)^2 + \dot{w}_{dr}^{*2} + (w_{dr}^* \dot{\theta}_1)^2 + (\vec{\omega}_r \times \vec{r}_{gmr}) \cdot (\vec{\omega}_r \times \vec{r}_{gmr}) \\ &\quad + 2\dot{\theta}_1^2 w_{dr}^* h + 2(\dot{\theta}_1 h) \hat{i}_1 \cdot (\vec{\omega}_r \times \vec{r}_{gmr}) + 2L_{gr} \dot{\theta}_1 w_d^* r \\ &\quad + 2(L_{gr} \dot{\theta}_1) \hat{j}_1 \cdot (\vec{\omega}_r \times \vec{r}_{gmr}) + 2(w_d^* r \dot{\theta}_1) \hat{i}_1 \cdot (\vec{\omega}_r \times \vec{r}_{gmr}) \end{aligned}$$

where w_c is the displacement of the conductor at $x_c = L_d$, w_{dr}^* is the vertical displacement of the messenger at $x_r = L_{gr}$ (L_{gr} is the length of the messenger on the right), and w_{dl}^* is the vertical displacement of the messenger at $x_l = L_{gl}$ (L_{gl} is the length of the messenger on the left).

Expressing unit vectors of frame 1, F_1 , with respect to those of frame 2, F_2 , leads to:

$$\begin{aligned} \hat{i}_1 &= \cos\theta_1 \hat{i}_0 - \sin\theta_1 \hat{j}_0 \\ \hat{j}_1 &= \sin\theta_1 \hat{i}_0 + \cos\theta_1 \hat{j}_0 \end{aligned}$$

Using these equations, $\dot{\vec{r}}_{mr(1)}$ can be expressed with respect to the fixed frame F_0 and

$$\begin{aligned}\dot{\vec{r}}_c^* \cdot \dot{\vec{r}}_{mr(1)} &= \dot{w}_c^* \hat{j}_o \cdot [\dot{\theta}_1 h (\cos\theta_1 \hat{i}_o + \sin\theta_1 \hat{j}_o) - L_{gr} \dot{\theta}_1 (-\sin\theta_1 \hat{i}_o + \cos\theta_1 \hat{j}_o) \\ &\quad + \dot{w}_{dr}^* (-\sin\theta_1 \hat{i}_o + \cos\theta_1 \hat{j}_o) + w_{dr}^* \dot{\theta}_1 (\cos\theta_1 \hat{i}_o + \sin\theta_1 \hat{j}_o) + (\vec{\omega} \times \vec{r}_{gmr})]\end{aligned}$$

Hence the coupling between the conductor and the right-end mass becomes:

$$\begin{aligned}\dot{\vec{r}}_c^* \cdot \dot{\vec{r}}_{mr(1)} &= \dot{w}_c^* \dot{\theta}_1 h \sin\theta_1 + \dot{w}_c^* L_{gr} \dot{\theta}_1 \cos\theta_1 + \dot{w}_c^* w_{dr}^* \cos\theta_1 + \dot{w}_c^* w_{dr}^* \dot{\theta}_1 \sin\theta_1 \\ &\quad + \dot{w}_c^* \hat{j}_o \vec{\omega} \times \vec{r}_{gmr}\end{aligned}$$

Now, substituting the equations above into $\dot{\vec{r}}_{mr(o)} \cdot \dot{\vec{r}}_{mr(o)}$ and taking the integration of the resultant equation yields the KE of the right-end mass which may be written as:

$$T_{mr} = \frac{1}{2} \int_m \dot{\vec{r}}_c^* \cdot \dot{\vec{r}}_c^* dm + \int_m \dot{\vec{r}}_c^* \cdot \dot{\vec{r}}_{mr(1)} dm + \frac{1}{2} \int_m \dot{\vec{r}}_{mr(1)} \cdot \dot{\vec{r}}_{mr(1)} dm \quad (3.29)$$

Note that $\int_m \vec{r}_{gm} dm = 0$ since this is the first moment about the centre of mass. Also, $\int_m (\vec{\omega}_r \times \vec{r}_{gmr}) \cdot (\vec{\omega}_r \times \vec{r}_{gmr}) dm = I\omega_r^2$. Where I is the moment of inertia. The next step is to evaluate each term in equation 3.29.

$$\int_m \frac{1}{2} \dot{\vec{r}}_c^* \cdot \dot{\vec{r}}_c^* dm = \frac{1}{2} m_c (\dot{w}_c^*)^2$$

$$\int_m (\dot{\vec{r}}_c^* \cdot \dot{\vec{r}}_{mr(1)}) dm = m_{dr} \dot{w}_c^* [\dot{\theta}_1 (h \sin\theta_1 + L_{gr} \cos\theta_1 + w_{dr}^* \sin\theta_1) + \dot{w}_{dr}^* \cos\theta_1]$$

$$\begin{aligned}\frac{1}{2} \int_m \dot{\vec{r}}_{mr(1)} \cdot \dot{\vec{r}}_{mr(1)} dm &= \frac{1}{2} m_{dr} [\dot{\theta}_1^2 (h^2 + L_{gr}^2 + w_{dr}^{*2} + 2hw_{dr}^*) + 2\dot{\theta}_1 L_{gr} \dot{w}_{dr}^* + \dot{w}_{dr}^{*2}] \\ &\quad + \frac{1}{2} I_{dr} (\dot{\theta}_1 + \dot{\theta}_2)^2\end{aligned}$$

Hence equation 3.29 becomes:

$$\begin{aligned}
T_{mr} = & \frac{1}{2}m_{mr}(\dot{w}_c^{*2} + (\dot{\theta}_1 h)^2 + 2\dot{w}_c^* \dot{\theta}_1 h) + \frac{1}{2}(\rho A)_{mr} \int_0^{L_{gr}} \{2\dot{w}_c^* [\dot{\theta}_1 (x_{mr} \cos \theta_1 \\
& + w_{dr} \sin \theta_1) + \dot{w}_{dr} \cos \theta_1] + \dot{\theta}_1^2 (x_{mr}^2 + w_{dr}^2 + 2hw_{dr}) + 2x_{mr} \dot{w}_{dr} \dot{\theta}_1 + \dot{w}_{dr}^2\} dx_{mr}
\end{aligned} \tag{3.30}$$

Assuming small deformation and rotation, $\sin \theta \approx \theta$ and $\cos \theta \approx 1$ and dropping higher order terms (≥ 3), equation 3.30 becomes:

$$\begin{aligned}
T_{mr} = & \frac{1}{2}m_{dr} \{ \dot{w}_c^{*2} + 2\dot{w}_c^* (\dot{\theta}_1 L_{gr} + \dot{w}_{dr}^*) + \dot{\theta}_1^2 (h^2 + L_{gr}^2) + 2L_{gr} \dot{w}_{dr}^* \dot{\theta}_1 + \dot{w}_{dr}^{*2} \} \\
& + \frac{1}{2}I_{dr} (\dot{\theta}_1 + \dot{\theta}_2)^2
\end{aligned} \tag{3.31}$$

Similarly, the KE of the left-end is given as:

$$\begin{aligned}
T_{ml} = & \frac{1}{2}m_{dl} \{ \dot{w}_c^{*2} + 2\dot{w}_c^* (-\dot{\theta}_1 L_{gl} + \dot{w}_{dl}^*) + \dot{\theta}_1^2 (h^2 + L_{gl}^2) - 2L_{gl} \dot{w}_{dl}^* \dot{\theta}_1 + \dot{w}_{dl}^{*2} \} \\
& + \frac{1}{2}I_{dl} (\dot{\theta}_1 + \dot{\theta}_3)^2
\end{aligned} \tag{3.32}$$

The KE of the cable on the right-side is given as:

$$\begin{aligned}
T_{mmr} = & \frac{1}{2}m_{mr}(\dot{w}_c^{*2} + (\dot{\theta}_1 h)^2) + \frac{1}{2}(\rho A)_{mr} \int_0^{L_{gr}} \{2\dot{w}_c^* \dot{w}_{dr} + 2x_{mr} \dot{\theta}_1 \dot{w}_{dr} + \dot{w}_{dr}^2\} dx \\
& + \frac{1}{2}(\rho A)_{mr} (\dot{w}_c^* \dot{\theta}_1 L_{gr}^2 + \frac{2}{3} \dot{\theta}_1^2 L_{gr}^3)
\end{aligned} \tag{3.33}$$

Similarly, the KE of the cable on the left-side is:

$$\begin{aligned}
T_{mml} = & \frac{1}{2}m_{ml}(\dot{w}_c^{*2} + (\dot{\theta}_1 h)^2) + \frac{1}{2}(\rho A)_{ml} \int_0^{L_{gl}} \{2\dot{w}_c^* \dot{w}_{dl} - 2x_{ml} \dot{\theta}_1 \dot{w}_{dl} + \dot{w}_{dl}^2\} dx \\
& - \frac{1}{2}(\rho A)_{ml} (\dot{w}_c^* \dot{\theta}_1 L_{gl}^2 + \frac{2}{3} \dot{\theta}_1^2 L_{gl}^3)
\end{aligned} \tag{3.34}$$

The total KE is then obtained as:

$$\begin{aligned}
T &= T_c + T_{mr} + T_{ml} + T_{mmr} + T_{mml} \\
T &= \frac{(\rho A)_c}{2} \int_0^{L_c} \dot{w}_c \cdot \dot{w}_c dx + \frac{1}{2} m_{dr} \{ \dot{w}_c^{*2} + 2\dot{w}_c^* (\dot{\theta}_1 L_{gr} + \dot{w}_{dr}^*) + \dot{\theta}_1^2 (h^2 + L_{gr}^2) \\
&\quad + 2L_{gr} \dot{w}_{dr}^* \dot{\theta}_1 + \dot{w}_{dr}^{*2} \} + \frac{1}{2} I_{dr} (\dot{\theta}_1 + \dot{\theta}_2)^2 + \frac{1}{2} m_{dl} \{ \dot{w}_c^{*2} + 2\dot{w}_c^* (-\dot{\theta}_1 L_{gl} + \dot{w}_{dl}^*) \\
&\quad + \dot{\theta}_1^2 (h^2 + L_{gl}^2) - 2L_{gl} \dot{w}_{dl}^* \dot{\theta}_1 + \dot{w}_{dl}^{*2} \} + \frac{1}{2} I_{dl} (\dot{\theta}_1 + \dot{\theta}_3)^2 \\
&\quad + \frac{1}{2} m_{mr} (\dot{w}_c^{*2} + (\dot{\theta}_1 h)^2) + \frac{1}{2} (\rho A)_{mr} \int_0^{L_{gr}} \{ 2\dot{w}_c^* \dot{w}_{dr} + 2x_{mr} \dot{\theta}_1 \dot{w}_{dr} + \dot{w}_{dr}^2 \} dx \\
&\quad + \frac{1}{2} (\rho A)_{mr} (\dot{w}_c^* \dot{\theta}_1 L_{gr}^2 + \frac{2}{3} \dot{\theta}_1^2 L_{gr}^3) + \frac{1}{2} m_{ml} (\dot{w}_c^{*2} + (\dot{\theta}_1 h)^2) \\
&\quad + \frac{1}{2} (\rho A)_{ml} \int_0^{L_{gl}} \{ 2\dot{w}_c^* \dot{w}_{dl} - 2x_{ml} \dot{\theta}_1 \dot{w}_{dl} + \dot{w}_{dl}^2 \} dx - \frac{1}{2} (\rho A)_{ml} (\dot{w}_c^* \dot{\theta}_1 L_{gl}^2 + \frac{2}{3} \dot{\theta}_1^2 L_{gl}^3)
\end{aligned} \tag{3.35}$$

3.2.4 Potential Energy

The strain energy is defined as follows:

$$U = \frac{1}{2} \int_V \sigma \epsilon dV \tag{3.36}$$

where ϵ is strain, σ the stress, and dV the differential volume. The strain is given as:

$$\epsilon = \frac{du}{dx} \tag{3.37}$$

From the assumption of using Euler-Bernoulli beam ($\frac{Length}{Thickness} > 20$), the displacement in the x direction is:

$$u = -z \frac{dw}{dx} \tag{3.38}$$

where w denotes the transverse displacement and z represents the coordinate in the transverse direction. Substituting the constitutive relation

$$\sigma = E\epsilon \quad (3.39)$$

and equations 3.37-3.38 into 3.36 yields:

$$U = \frac{1}{2} \int_A \int_0^L z^2 \left(\frac{d^2 w}{dx^2} \right)^2 E dx dA \quad (3.40)$$

$$\Rightarrow U = \frac{1}{2} EI \int_0^L (w'')^2 dx \quad (3.41)$$

where $I = \int_A z^2 dA$ is the moment of inertia. The tension length of the deformed differential element of the conductor is related to the undeformed length as:

$$ds = (dx^2 + dw^2)^{1/2} = dx \left[1 + \frac{1}{2} \left(\frac{dw}{dx} \right)^2 \right]$$

where dw is the displacement along y-axis, see Figure 3.2. Hence the differential stretch in the conductor is:

$$ds - dx = \frac{1}{2} \left(\frac{dw}{dx} \right)^2 dx \quad (3.42)$$

Therefore, the work done by the tension is:

$$W = \frac{1}{2} T \int_0^L \left(\frac{dw}{dx} \right)^2 dx \quad (3.43)$$

Using equations 3.41 and 3.43, the potential energy (PE) of the conductor can be expressed as:

$$V_c = \frac{1}{2} (EI)_c \int_0^{L_c} \left(\frac{\partial^2 w_c}{\partial x^2} \right)^2 dx - \frac{1}{2} T \int_0^{L_c} \left(\frac{\partial w_c}{\partial x} \right)^2 dx \quad (3.44)$$

The PE of the right-end mass is:

$$V_{mr} = -m_{dr}g\hat{j}_o[w_c^*\hat{j}_o + h\cos\theta_1\hat{j}_o - \sin\theta_1\hat{i}_o + L_{gr}(\cos\theta_1\hat{i}_o + \sin\theta_1\hat{j}_o) + w_{dr}^*(\cos\theta_1\hat{j}_o + \sin\theta_1\hat{i}_o)] \quad (3.45)$$

where g denotes gravity ($g = 9.814 \text{ m/s}^2$). Using the assumption of small deformation where $\sin\theta_1 \approx \theta_1$ and $\cos\theta_1 \approx 1$, the PE of the right-end mass becomes:

$$V_{mr} = -m_{dr}g(w_c^* + h + L_{gr}\theta_1 + w_{dr}^*) \quad (3.46)$$

Similarly, the PE of the left-end mass is:

$$V_{ml} = -m_{dl}g(w_c^* + h - L_{gl}\theta_1 + w_{dl}^*) \quad (3.47)$$

Also, the PE of the right and left side of the messenger are expressed as:

$$V_{mmr} = \frac{1}{2}(EI)_{mr} \int_0^{L_{gr}} \frac{\partial^2 w_{mr}}{\partial x^2}^2 dx \quad (3.48)$$

$$V_{mml} = \frac{1}{2}(EI)_{ml} \int_0^{L_{gl}} \frac{\partial^2 w_{ml}}{\partial x^2}^2 dx \quad (3.49)$$

The total PE is: $V = V_c + V_{mr} + V_{ml} + V_{mmr} + V_{mml}$ and after algebraic work, it is written as:

$$V = \frac{1}{2}\left\{(EI)_c \int_0^{L_c} \frac{\partial^2 w_c}{\partial x^2}^2 dx - \frac{1}{2}T \int_0^{L_c} \frac{\partial w_c}{\partial x}^2 dx - m_{dr}g(w_c^* + h + L_{gr}\theta_1 + w_{dr}^*) - m_{dl}g(w_c^* + h - L_{gl}\theta_1 + w_{dl}^*) + \frac{1}{2}(EI)_{mr} \int_0^{L_{gr}} \frac{\partial^2 w_{mr}}{\partial x^2}^2 dx + \frac{1}{2}(EI)_{ml} \int_0^{L_{gl}} \frac{\partial^2 w_{ml}}{\partial x^2}^2 dx\right\} \quad (3.50)$$

where EI_c the flexural rigidity of the conductor. EI_{mr} , EI_{ml} , m_{dr} , and m_{dl} , are

the flexural rigidity and the mass of the counterweight on the right and left, respectively. L_{gr} and L_{gl} are the length of the messenger on the right-side and the left-side, respectively.

3.3 Finite Element Modeling

This section consists of two subsections. The first subsection deals with the finite element modeling of the conductor without a damper and the second includes the damper.

The field variable is interpolated along the span of the structure using cubic Lagrange interpolation shape functions [30]. These cubic shape functions, ϕ , are also known as Hermite shape functions and are defined as:

$$\begin{aligned} \phi_1 &= 1 - 3\frac{\xi^2}{L^2} + 2\frac{\xi^3}{L^3} & \phi_2 &= \xi - 2\frac{\xi^2}{L} + \frac{\xi^3}{L^2} \\ \phi_3 &= 3\frac{\xi^2}{L^2} - 2\frac{\xi^3}{L^3} & \phi_4 &= -\frac{\xi^2}{L} + \frac{\xi^3}{L^2} \end{aligned} \quad (3.51)$$

3.3.1 Finite Element Modeling of the Conductor Without Damper

The representation of the finite element model of the conductor without damper is depicted in Figure 3.5. The element consists of two nodes and each node consists of two degrees of freedom to match with the hermit shape functions described previously.

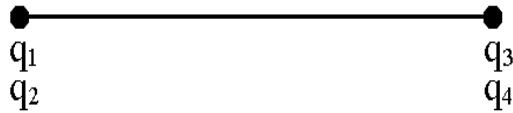


Figure 3.5: Schematic of finite element of the conductor without damper.

The equation of motion of a conductor without a damper was derived in section

3.1 and it is reproduced here as:

$$EI \frac{\partial^4 w}{\partial x^4} - T \frac{\partial^2 w}{\partial x^2} + m \frac{\partial^2 w}{\partial t^2} = 0 \quad (3.52)$$

Using Galerkin method with W_i denoting the weight factor leads to:

$$\int_0^L \left(EI \frac{\partial^4 w}{\partial x^4} - T \frac{\partial^2 w}{\partial x^2} + m \frac{\partial^2 w}{\partial t^2} \right) W_i dx = 0 \quad (3.53)$$

Discretization of the beam into a number of finite elements and integrating equation 3.53 by parts gives:

$$\int_0^L EI \frac{\partial^4 w}{\partial x^4} W_i dx - \int_0^L T \frac{\partial^2 w}{\partial x^2} W_i dx + \int_0^L m \frac{\partial^2 w}{\partial t^2} W_i dx = 0 \quad (3.54)$$

Integrating the first term of equation 3.54 twice gives:

$$\int_0^L EI \frac{\partial^4 w}{\partial x^4} W_i dx = [W_i V - W_i' M]_0^L + \int_0^L EI \frac{\partial^2 w}{\partial x^2} \cdot \frac{\partial^2 W_i}{\partial x^2} dx \quad (3.55)$$

where V and M are the shear and the bending moment, respectively and they are given as follows:

$$V = -EI \frac{\partial^3 w}{\partial x^3} \quad \text{and} \quad M = EI \frac{\partial^2 w}{\partial x^2}$$

Integrating the second term of equation 3.54 once yields:

$$\int_0^L T \frac{\partial^2 w}{\partial x^2} W_i dx = \left[T W_i \frac{\partial w}{\partial x} \right]_0^L - \int_0^L W_i' T \frac{\partial w}{\partial x} dx \quad (3.56)$$

Substitute equations (3.55) and (3.56) into equation (3.54) yields:

$$[V W_i - M W_i']_0^L + \int_0^L EI \frac{\partial^2 w}{\partial x^2} \cdot \frac{\partial^2 W_i}{\partial x^2} - \left[T W_i \frac{\partial w}{\partial x} \right]_0^L + T \int_0^L \frac{\partial w}{\partial x} \cdot \frac{\partial W_i}{\partial x} dx + \int_0^L m \frac{\partial^2 w}{\partial t^2} W_i dx = 0 \quad (3.57)$$

W_i can be written as:

$$W_i = \frac{\partial \tilde{w}}{\partial q_i} \quad \text{where} \quad \tilde{w} = [\phi] \{q\} \quad \text{as well} \quad \tilde{w}_{xx} = [\phi]_{xx} \{q\} \quad \text{and} \quad \ddot{\tilde{w}} = [\phi] \{\ddot{q}\}$$

where

$$\phi = \begin{bmatrix} \phi_1 & \phi_2 & \phi_3 & \phi_4 \end{bmatrix},$$

$$q = \begin{Bmatrix} q_1 \\ q_2 \\ q_3 \\ q_4 \end{Bmatrix},$$

q and \ddot{q} represent the nodal displacement and acceleration, respectively.

Note that

$$W_i = \phi_j$$

Applying boundary conditions:

$$\begin{aligned} \text{For } x = 0; \quad W_i(0) &= 0 \\ x = L; \quad W_i(L) &= 0 \end{aligned}$$

Since there is no deflection at both ends:

$$[VW_i - MW_i]_0^L = 0 \quad \text{and} \quad \left[TW_i \frac{\partial w}{\partial x} \right]_0^L = 0$$

Hence equation 3.57 gives:

$$\int_0^L \left([\phi]_{xx}^T EI [\phi]_{xx} \right) dx \{q\} + \int_0^L \left([\phi]_x^T T [\phi]_x \right) dx \{q\} + \int_0^L \left([\phi]^T m [\phi] \right) dx \{\ddot{q}\} = 0 \quad (3.58)$$

Equation 3.58 can be written as:

$$[M] \{\ddot{q}\} + ([K_B] + [K_T]) \{q\} = 0 \quad (3.59)$$

where the mass matrix, M is expressed as:

$$[M] = \int_0^L \left([\phi]^T m [\phi] \right) dx$$

The above equation yields:

$$[M] = \frac{\rho AL}{420} \begin{bmatrix} 156 & 22L & 54 & -13L \\ 22L & 4L^2 & 13L & -3L^2 \\ 54 & 13L & 156 & -22L \\ -13L & -3L^2 & -22L & 4L^2 \end{bmatrix} \quad (3.60)$$

The stiffness matrix due to bending, K_B is :

$$[K_B] = \int_0^L \left([\phi]_{xx}^T EI [\phi]_{xx} \right) dx$$

The above equation yields:

$$[K_B] = \frac{EI}{L^3} \begin{bmatrix} 12 & 6L & -12L & 6L \\ 6L & 4L^2 & -6L & 2L^2 \\ -12L & -6L & 12 & -6L \\ 6L & 2L^2 & -6L & 4L^2 \end{bmatrix} \quad (3.61)$$

Also, the stiffness matrix due to tension, K_T can be written as follows:

$$[K_T] = \int_0^L \left([\phi]_x^T T [\phi]_x \right) dx$$

The above equation becomes:

$$[K_T] = \frac{T}{5} \begin{bmatrix} \frac{6}{L} & 0.5 & -\frac{6}{L} & 0.5 \\ 0.5 & 0.667L & -0.5 & -\frac{L}{15} \\ -\frac{6}{L} & -0.5 & \frac{6}{L} & -0.5 \\ 0.5 & -\frac{L}{15} & -0.5 & 0.667L \end{bmatrix} \quad (3.62)$$

3.3.2 Finite Element Modeling of the Conductor With the Damper

In this section, the kinetic and potential energies derived in section 3.2 are used in conjunction with the Hamilton's principle to derive the stiffness and mass matrices of the element of the conductor with a damper. The finite element of the conductor with the damper is delineated in Figure 3.6. This element consists of five nodes, two for the conductor and three for the messenger. Initially, the messenger consisted of four nodes, two each on the left-side and right-side. However, a node on both sides coincide at the point of contact of the messenger with the clamp. Hence, these two nodes were merged, resulting in three nodes for the messenger. Overall, the size of the element matrices of the conductor with a damper resulted in a 10x10 matrix since each node consists of two degrees of freedom.

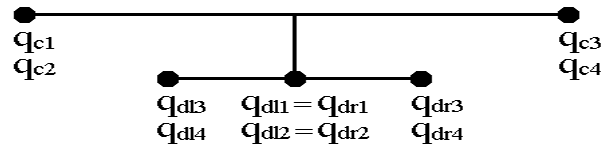


Figure 3.6: Schematic of finite element of the conductor with damper.

The displacement of the conductor, the right-side damper, and the left-side damper

are written as follows:

$$\begin{aligned}
w_c &= \phi_c^T q_c \\
w_{dr} &= \phi_{dr}^T q_{dr} \\
w_{dl} &= \phi_{dl}^T q_{dl}
\end{aligned} \tag{3.63}$$

where the ϕ s represent the elemental mode shape vectors and the q s represent the elemental displacement vectors. The subscripts c , dr , and dl denote the conductor, the damper on the right, and the damper on the left, respectively. Note that the superscript T denotes matrix transpose.

The slopes are defined as

$$\begin{aligned}
\theta_1 &= \frac{\partial w_c^*}{\partial x} = \phi_c^{*T'} q_c \\
\theta_2 &= \frac{\partial w_{dr}^*}{\partial x} = \phi_{dr}^{*T'} q_{dr} \\
\theta_3 &= \frac{\partial w_{dl}^*}{\partial x} = \phi_{dl}^{*T'} q_{dl}
\end{aligned} \tag{3.64}$$

where ϕ_c^* represents the elemental mode shapes vector at $x = L_d$, ϕ_{dr}^* and ϕ_{dl}^* represents the elemental mode shapes vectors at $x_r = L_{gr}$ and $x_l = L_{gl}$, respectively.

Substituting equation 3.63 and 3.64 into the kinetic energy equation 3.35, yields:

$$\begin{aligned}
T = & \frac{(\rho A)_c}{2} \int_0^{L_c} (\dot{q}_c^T \phi_c \phi_c^T \dot{q}_c) dx + \frac{1}{2} m_{dr} \{ \dot{q}_c^T \phi_c^* \phi_c^{*T} \dot{q}_c + 2 \dot{q}_c^T \phi_c^* (\dot{q}_c^T \phi_c^{*T} L_{gr} \\
& + \dot{q}_{dr}^T \phi_{dr}^*) + (\dot{q}_c^T \phi_c^{*'} \phi_c^{*T} \dot{q}_c) (h^2 + L_{gr}^2) + 2 L_{gr} \dot{q}_{dr}^T \phi_{dr}^* \phi_c^{*T} \dot{q}_c + \dot{q}_{dr}^T \phi_{dr}^* \phi_{dr}^{*T} \dot{q}_{dr} \} \\
& + \frac{1}{2} I_{dr} ((\dot{q}_c^T \phi_c^{*'} \phi_c^{*T} \dot{q}_c) + (\dot{q}_{dr}^T \phi_{dr}^{*'} \phi_{dr}^{*T} \dot{q}_{dr}) + 2 \dot{q}_c^T \phi_c^{*'} \phi_{dr}^{*T} \dot{q}_{dr}) \\
& + \frac{1}{2} m_{dl} \{ \dot{q}_c^T \phi_c^* \phi_c^{*T} \dot{q}_c + 2 \dot{q}_c^T \phi_c^* (-\dot{q}_c^T \phi_c^{*'} L_{gl} + \dot{q}_{dl}^T \phi_{dl}^*) \\
& + (\dot{q}_c^T \phi_c^{*'} \phi_c^{*T} \dot{q}_c) (h^2 + L_{gl}^2) - 2 L_{gl} \dot{q}_{dl}^T \phi_{dl}^* \phi_c^{*T} \dot{q}_c + \dot{q}_{dl}^T \phi_{dl}^* \phi_{dl}^{*T} \dot{q}_{dl} \} \\
& + \frac{1}{2} I_{dl} ((\dot{q}_c^T \phi_c^{*'} \phi_c^{*T} \dot{q}_c) + (\dot{q}_{dl}^T \phi_{dl}^{*'} \phi_{dl}^{*T} \dot{q}_{dl}) + 2 \dot{q}_c^T \phi_c^{*'} \phi_{dl}^{*T} \dot{q}_{dl}) \\
& + \frac{1}{2} m_{mr} ((\dot{q}_c^T \phi_c^* \phi_c^{*T} \dot{q}_c) + (\dot{q}_c^T \phi_c^{*'} \phi_c^{*T} \dot{q}_c) h^2) \tag{3.65} \\
& + \frac{1}{2} (\rho A)_{mr} \int_0^{L_{gr}} \{ 2 \dot{q}_c^T \phi_c^* \phi_{dr}^T \dot{q}_{dr} + 2 x_{mr} \dot{q}_c^T \phi_c^{*'} \phi_{dr}^T \dot{q}_{dr} \\
& + \dot{q}_{dr}^T \phi_{dr} \phi_{dr}^T \dot{q}_{dr} \} dx + \frac{1}{2} (\rho A)_{mr} (\dot{q}_c^T \phi_c^* \phi_c^{*'} \dot{q}_c L_{gr}^2 + \frac{2}{3} \dot{q}_c^T \phi_c^{*'} \phi_c^{*T} \dot{q}_c L_{gr}^3) \\
& + \frac{1}{2} m_{ml} ((\dot{q}_c^T \phi_c^* \phi_c^{*T} \dot{q}_c) + (\dot{q}_c^T \phi_c^{*'} \phi_c^{*T} \dot{q}_c) h^2) \\
& + \frac{1}{2} (\rho A)_{ml} \int_0^{L_{gl}} \{ 2 \dot{q}_c^T \phi_c^* \phi_{dl}^T \dot{q}_{dl} - 2 x_{ml} \dot{q}_c^T \phi_c^{*'} \phi_{dl}^T \dot{q}_{dl} + \dot{q}_{dl}^T \phi_{dl} \phi_{dl}^T \dot{q}_{dl} \} dx \\
& - \frac{1}{2} (\rho A)_{ml} (\dot{q}_c^T \phi_c^* \phi_c^{*'} \dot{q}_c L_{gl}^2 + \frac{2}{3} \dot{q}_c^T \phi_c^{*'} \phi_c^{*T} \dot{q}_c L_{gl}^3)
\end{aligned}$$

Now, substituting equations 3.63 and 3.64 into the potential energy equation 3.50, yields:

$$\begin{aligned}
V = & \frac{1}{2}EI \int_0^{L_c} (q_c^T \phi_c'' \phi_c''^T q_c) dx - \frac{1}{2}T \int_0^{L_c} (q_c^T \phi_c' \phi_c'^T q_c) dx - m_{dr}g(q_c^T \phi_c^* + h \\
& + L_{gr}q_c^T \phi_c^* + q_{dr}^T \phi_{dr}^*) - m_{dl}g(q_c^T \phi_c^* + h - L_{gl}q_c^T \phi_c^* + q_{dl}^T \phi_{dl}^*) \quad (3.66) \\
& + \frac{1}{2}(EI)_{mr} \int_0^{L_{gr}} (q_{dr}^T \phi_{dr}'' \phi_{dr}''^T q_{dr}) dx + \frac{1}{2}(EI)_{ml} \int_0^{L_{gl}} (q_{dl}^T \phi_{dl}'' \phi_{dl}''^T q_{dl}) dx
\end{aligned}$$

Hamilton's principle is used to derive the equation of motion:

$$\int_{t_1}^{t_2} (\delta T - \delta V + \delta W_{nc}) dt = 0$$

where δT is the variational of the kinetic energy, δV the variational of the potential energy, and δW_{nc} is the virtual work of the applied forces. And the variational of the position vector is: $\delta \mathbf{r}_i = \mathbf{0}, i = 1, 2, \dots, \phi : T = t_1 + t_2$

Taking the variation of the kinetic energy:

$$\begin{aligned}
\delta T = & (\rho A)_c \int_0^{L_c} (\delta \dot{q}_c^T \phi_c \phi_c^T \dot{q}_c) dx + \frac{1}{2} m_{dr} \{ 2\delta \dot{q}_c^T \phi_c^* \phi_c^{*T} \dot{q}_c + 2\delta \dot{q}_c^T \phi_c^* \phi_c^{*T} \dot{q}_c L_{gr} \\
& + 2\delta \dot{q}_c^T \phi_c^* \phi_c^{*T} \dot{q}_c L_{gr} + 2\delta \dot{q}_c^T \phi_c^* \phi_{dr}^{*T} \dot{q}_{dr} + 2\delta \dot{q}_{dr}^T \phi_{dr}^* \phi_c^{*T} \dot{q}_c + 2(\delta \dot{q}_c^T \phi_c^* \phi_c^{*T} \dot{q}_c)(h^2 + L_{gr}^2) \\
& + 2L_{gr} \delta \dot{q}_{dr}^T \phi_{dr}^* \phi_c^{*T} \dot{q}_c + 2L_{gr} \delta \dot{q}_c^T \phi_c^* \phi_{dr}^{*T} \dot{q}_{dr} + 2\delta \dot{q}_{dr}^T \phi_{dr}^* \phi_{dr}^{*T} \dot{q}_{dr} \} \\
& + I_{dr} ((\delta \dot{q}_c^T \phi_c^* \phi_c^{*T} \dot{q}_c) + (\delta \dot{q}_{dr}^T \phi_{dr}^* \phi_{dr}^{*T} \dot{q}_{dr}) + \delta \dot{q}_c^T \phi_c^* \phi_{dr}^{*T} \dot{q}_{dr} + \delta \dot{q}_{dr}^T \phi_{dr}^* \phi_c^{*T} \dot{q}_c) \\
& + \frac{1}{2} m_{dl} \{ 2\delta \dot{q}_c^T \phi_c^* \phi_c^{*T} \dot{q}_c - 2\delta \dot{q}_c^T \phi_c^* \phi_c^{*T} \dot{q}_c L_{gl} - 2\delta \dot{q}_c^T \phi_c^* \phi_c^{*T} \dot{q}_c L_{gl} + 2\delta \dot{q}_c^T \phi_c^* \phi_{dl}^{*T} \dot{q}_{dl} \\
& + 2\delta \dot{q}_{dl}^T \phi_{dl}^* \phi_c^{*T} \dot{q}_c + 2(\delta \dot{q}_c^T \phi_c^* \phi_c^{*T} \dot{q}_c)(h^2 + L_{gl}^2) - 2L_{gl} \delta \dot{q}_{dl}^T \phi_{dl}^* \phi_c^{*T} \dot{q}_c \\
& - 2L_{gl} \delta \dot{q}_c^T \phi_c^* \phi_{dl}^{*T} \dot{q}_{dl} + 2\delta \dot{q}_{dl}^T \phi_{dl}^* \phi_{dl}^{*T} \dot{q}_{dl} \} + I_{dl} ((\delta \dot{q}_c^T \phi_c^* \phi_c^{*T} \dot{q}_c) + (\delta \dot{q}_{dl}^T \phi_{dl}^* \phi_{dl}^{*T} \dot{q}_{dl}) \\
& + \delta \dot{q}_c^T \phi_c^* \phi_{dl}^{*T} \dot{q}_{dl} + \delta \dot{q}_{dl}^T \phi_{dl}^* \phi_c^{*T} \dot{q}_c) + m_{mr} ((\delta \dot{q}_c^T \phi_c^* \phi_c^{*T} \dot{q}_c) \tag{3.67} \\
& + (\delta \dot{q}_c^T \phi_c^* \phi_c^{*T} \dot{q}_c) h^2) + \frac{1}{2} (\rho A)_{mr} \int_0^{L_{gr}} \{ 2(\delta \dot{q}_c^T \phi_c^* \phi_{dr}^{*T} \dot{q}_{dr} + \delta \dot{q}_{dr}^T \phi_{dr}^* \phi_c^{*T} \dot{q}_c) \\
& + 2x_{mr} (\delta \dot{q}_c^T \phi_c^* \phi_{dr}^{*T} \dot{q}_{dr} + \delta \dot{q}_{dr}^T \phi_{dr}^* \phi_c^{*T} \dot{q}_c) + 2\delta \dot{q}_{dr}^T \phi_{dr}^* \phi_{dr}^{*T} \dot{q}_{dr} \} dx \\
& + \frac{1}{2} (\rho A)_{mr} ((\delta \dot{q}_c^T \phi_c^* \phi_c^{*T} \dot{q}_c + \delta \dot{q}_c^T \phi_c^* \phi_c^{*T} \dot{q}_c) L_{gr}^2 + \frac{4}{3} \delta \dot{q}_c^T \phi_c^* \phi_c^{*T} \dot{q}_c L_{gr}^3) \\
& + m_{ml} ((\delta \dot{q}_c^T \phi_c^* \phi_c^{*T} \dot{q}_c) + (\delta \dot{q}_c^T \phi_c^* \phi_c^{*T} \dot{q}_c) h^2) + \frac{1}{2} (\rho A)_{ml} \int_0^{L_{gl}} \{ 2(\delta \dot{q}_c^T \phi_c^* \phi_{dl}^{*T} \dot{q}_{dl} \\
& + \delta \dot{q}_{dl}^T \phi_{dl}^* \phi_c^{*T} \dot{q}_c) - 2x_{ml} (\delta \dot{q}_c^T \phi_c^* \phi_{dl}^{*T} \dot{q}_{dl} + \delta \dot{q}_{dl}^T \phi_{dl}^* \phi_c^{*T} \dot{q}_c) + 2\delta \dot{q}_{dl}^T \phi_{dl}^* \phi_{dl}^{*T} \dot{q}_{dl} \} dx \\
& - \frac{1}{2} (\rho A)_{ml} ((\delta \dot{q}_c^T \phi_c^* \phi_c^{*T} \dot{q}_c + \delta \dot{q}_c^T \phi_c^* \phi_c^{*T} \dot{q}_c) L_{gl}^2 + \frac{4}{3} \delta \dot{q}_c^T \phi_c^* \phi_c^{*T} \dot{q}_c L_{gl}^3)
\end{aligned}$$

The variation in the potential energy is:

$$\begin{aligned}
\delta V = & \delta q_c^T (EI \int_0^{L_c} \phi_c'' \phi_c''^T q_c dx - T \int_0^{L_c} \phi_c' \phi_c'^T q_c dx) - \delta q_c^T g [m_{dr}(\phi_c^* + L_{gr} \phi_c^*) \\
& - m_{dl}(\phi_c^* - L_{gl} \phi_c^*)] - \delta q_{dr}^T m_{dr} g \phi_{dr}^* - \delta q_{dl}^T m_{dl} g \phi_{dl}^* \\
& + \delta q_{dr}^T ((EI)_{mr} \int_0^{L_{gr}} \phi_{dr}'' \phi_{dr}''^T q_{dr}) dx + \delta q_{dl}^T ((EI)_{ml} \int_0^{L_{gl}} \phi_{dl}'' \phi_{dl}''^T q_{dl}) dx
\end{aligned} \tag{3.68}$$

The variation of W_g , δW_g is defined as:

$$\delta W_g = -\delta q_c^T g [m_{dr}(\phi_c^* + L_{gr} \phi_c^*) - m_{dl}(\phi_c^* - L_{gl} \phi_c^*)] - \delta q_{dr}^T m_{dr} g \phi_{dr}^* - \delta q_{dl}^T m_{dl} g \phi_{dl}^* \tag{3.69}$$

Note that δW_g is the work due to gravity. Hence, the variation of the potential energy becomes:

$$\begin{aligned}
\delta V = & \delta q_c^T (EI \int_0^{L_c} \phi_c'' \phi_c''^T q_c dx - T \int_0^{L_c} \phi_c' \phi_c'^T q_c dx) + \delta q_{dr}^T ((EI)_{mr} \int_0^{L_{gr}} \phi_{dr}'' \phi_{dr}''^T q_{dr}) dx \\
& + \delta q_{dl}^T ((EI)_{ml} \int_0^{L_{gl}} \phi_{dl}'' \phi_{dl}''^T q_{dl}) dx + \delta W_g
\end{aligned} \tag{3.70}$$

Observe that the potential energy and the work by the weight involve only the virtual displacement whereas, the kinetic energy involves both virtual displacement and virtual velocity. Therefore, in order to derive the equation of motion, the virtual velocity must be transformed to virtual displacement through integration by parts of the kinetic energy.

Recall integration by parts: $\int u dv = uv| - \int v du$. Whereupon, in this case, the uv term equals zero because of the auxiliary condition that states t_1 and t_2 are known.

To this end, carrying out the integration by parts of the variation of the kinetic energy and rearranging and factorizing by δq_c , δq_{dr} , and δq_{dl} , respectively, leads to

the equation below:

$$\begin{aligned}
\int_{t_1}^{t_2} \delta T dt = & - \left(\int_{t_1}^{t_2} (\delta q_c^T [\{(\rho A)_c \int_0^{L_c} \phi_c \phi_c^T dx + m_{dr} [\phi_c^* \phi_c^{*T} + L_{gr} (\phi_c^* \phi_c^{*T} \right. \\
& + \phi_c' \phi_c^{*T} + \phi_c^* \phi_c'^{*T}) (h^2 + L_{gr}^2)] + I_{dr} \phi_c' \phi_c'^{*T} + m_{dl} [\phi_c^* \phi_c^{*T} - L_{gl} (\phi_c^* \phi_c'^{*T} \\
& + \phi_c' \phi_c^{*T} + \phi_c^* \phi_c'^{*T}) (h^2 + L_{gl}^2)] + I_{dl} \phi_c' \phi_c'^{*T} + m_{mr} [\phi_c^* \phi_c^{*T} + \phi_c' \phi_c'^{*T} h^2] \\
& + \frac{1}{2} (\rho A)_{mr} [L_{gr}^2 (\phi_c^* \phi_c'^{*T} + \phi_c' \phi_c^{*T}) + \frac{2}{3} L_{gr}^3 \phi_c' \phi_c'^{*T}] + m_{ml} [\phi_c^* \phi_c^{*T} \\
& + \phi_c' \phi_c'^{*T} h^2] + \frac{1}{2} (\rho A)_{ml} [-L_{gl}^2 (\phi_c^* \phi_c'^{*T} + \phi_c' \phi_c^{*T}) + \frac{2}{3} L_{gl}^3 \phi_c' \phi_c'^{*T}] dx \} \ddot{q}_c \\
& + \{ m_{dr} (\phi_c^* \phi_{dr}^{*T} + L_{gr} \phi_c' \phi_{dr}^{*T}) + I_{dr} \phi_c' \phi_{dr}^{*T} + (\rho A)_{mr} \int_0^{L_{gr}} (\phi_c^* \phi_{dr}^T \\
& + x_{mr} \phi_c' \phi_{dr}^T) dx_{mr} \} \ddot{q}_{dr} + \{ m_{dl} (\phi_c^* \phi_{dl}^{*T} - L_{gl} \phi_c' \phi_{dl}^{*T}) + I_{dl} \phi_c' \phi_{dl}^{*T} \\
& + (\rho A)_{ml} \int_0^{L_{gl}} (\phi_c^* \phi_{dl}^T - x_{ml} \phi_c' \phi_{dl}^T) dx_{ml} \} \ddot{q}_{dl}] - \delta q_{dr}^T [\{ m_{dr} (\phi_{dr}^* \phi_c^{*T} \\
& + L_{gr} \phi_{dr}^* \phi_c'^{*T}) + I_{dr} \phi_{dr}^* \phi_c'^{*T} + (\rho A)_{mr} \int_0^{L_{gr}} (\phi_{dr} \phi_c^{*T} + x_{mr} \phi_{dr} \phi_c'^{*T}) dx_{mr} \} \ddot{q}_c \\
& + \{ m_{dr} \phi_{dr}^* \phi_{dr}^{*T} + I_{dr} \phi_{dr}^* \phi_{dr}^{*T} + (\rho A)_{mr} \int_0^{L_{gr}} \phi_{dr} \phi_{dr}^T dx_{mr} \} \ddot{q}_{dr} \\
& - \delta q_{dl}^T [\{ m_{dl} (\phi_{dl}^* \phi_c^{*T} - L_{gl} \phi_{dl}^* \phi_c'^{*T}) + I_{dl} \phi_{dl}^* \phi_c'^{*T} + (\rho A)_{ml} \int_0^{L_{gl}} (\phi_{dl} \phi_c^{*T} \\
& - x_{ml} \phi_{dl} \phi_c'^{*T}) dx_{ml} \} \ddot{q}_c + \{ m_{dl} [\phi_{dl}^* \phi_{dl}^{*T} + I_{dl} \phi_{dl}^* \phi_{dl}^{*T} \\
& + (\rho A)_{ml} \int_0^{L_{gl}} \phi_{dl} \phi_{dl}^T dx_{ml} \} \ddot{q}_{dl}] dt) \tag{3.71}
\end{aligned}$$

Hence, equation 3.71 can be written in a matrix form as follows:

$$[\delta q_c^T \delta q_{dr}^T \delta q_{dl}^T] \begin{bmatrix} M_{cc} & M_{cr} & M_{cl} \\ M_{rc} & M_{rr} & 0 \\ M_{lc} & 0 & M_{ll} \end{bmatrix} \begin{Bmatrix} \ddot{q}_c \\ \ddot{q}_{dr} \\ \ddot{q}_{dl} \end{Bmatrix} \quad (3.72)$$

where

$$\begin{aligned} M_{cc} = & (\rho A)_c \int_0^{L_c} \phi_c \phi_c^T dx + m_{dr} [\phi_c^* \phi_c^{*T} + L_{gr} (\phi_c^* \phi_c^{*T} + \phi_c' \phi_c^{*T} \\ & + \phi_c^{*'} \phi_c^{*T} (h^2 + L_{gr}^2))] + I_{dr} \phi_c^{*'} \phi_c^{*T} + m_{dl} [\phi_c^* \phi_c^{*T} - L_{gl} (\phi_c^* \phi_c^{*T} \\ & + \phi_c' \phi_c^{*T} + \phi_c^{*'} \phi_c^{*T} (h^2 + L_{gl}^2))] + I_{dl} \phi_c^{*'} \phi_c^{*T} + m_{mr} [\phi_c^* \phi_c^{*T} \\ & + \phi_c^{*'} \phi_c^{*T} h^2] + \frac{1}{2} (\rho A)_{mr} [L_{gr}^2 (\phi_c^* \phi_c^{*T} + \phi_c^{*'} \phi_c^{*T}) + \frac{2}{3} L_{gr}^3 \phi_c^{*'} \phi_c^{*T}] \\ & + m_{ml} [\phi_c^* \phi_c^{*T} + \phi_c^{*'} \phi_c^{*T} h^2] + \frac{1}{2} (\rho A)_{ml} [-L_{gl}^2 (\phi_c^* \phi_c^{*T} \phi_c^{*'} \phi_c^{*T}) \\ & + \frac{2}{3} L_{gl}^3 \phi_c^{*'} \phi_c^{*T}] dx \end{aligned}$$

$$\begin{aligned} M_{cr} = & m_{dr} (\phi_c^* \phi_{dr}^{*T} + L_{gr} \phi_c^{*'} \phi_{dr}^{*T}) + I_{dr} \phi_c^{*'} \phi_{dr}^{*T} \\ & + (\rho A)_{mr} \int_0^{L_{gr}} (\phi_c^* \phi_{dr}^T + x_{mr} \phi_c^{*'} \phi_{dr}^T) dx_{mr} \end{aligned}$$

$$\begin{aligned} M_{rc} = & m_{dr} (\phi_{dr}^* \phi_c^{*T} + L_{gr} \phi_{dr}^* \phi_c^{*T}) + I_{dr} \phi_{dr}^* \phi_c^{*T} \\ & + (\rho A)_{mr} \int_0^{L_{gr}} (\phi_{dr} \phi_c^{*T} + x_{mr} \phi_{dr} \phi_c^{*T}) dx_{mr} \end{aligned}$$

$$\begin{aligned}
M_{cl} &= m_{dl}(\phi_c^* \phi_{dl}^{*T} - L_{gl} \phi_c^* \phi_{dl}^{*T}) + I_{dl} \phi_c^* \phi_{dl}^{*T} \\
&\quad + (\rho A)_{ml} \int_0^{L_{gl}} (\phi_c^* \phi_{dl}^T - x_{ml} \phi_c^* \phi_{dl}^T) dx_{ml} \\
M_{lc} &= m_{dl}(\phi_{dl}^* \phi_c^{*T} - L_{gl} \phi_{dl}^* \phi_c^{*T}) + I_{dl} \phi_{dl}^* \phi_c^{*T} \\
&\quad + (\rho A)_{ml} \int_0^{L_{gl}} (\phi_{dl} \phi_c^{*T} - x_{ml} \phi_{dl} \phi_c^{*T}) dx_{ml} \\
M_{rr} &= m_{dr} \phi_{dr}^* \phi_{dr}^{*T} + I_{dr} \phi_{dr}^* \phi_{dr}^{*T} + (\rho A)_{mr} \int_0^{L_{gr}} \phi_{dr} \phi_{dr}^T dx_{mr} \\
M_{ll} &= m_{dl} \phi_{dl}^* \phi_{dl}^{*T} + I_{dl} \phi_{dl}^* \phi_{dl}^{*T} + (\rho A)_{ml} \int_0^{L_{gl}} \phi_{dl} \phi_{dl}^T dx_{ml}
\end{aligned}$$

Thus, the mass matrix M_D can be expressed as:

$$M_D = \begin{bmatrix} M_{cc} & M_{cr} & M_{cl} \\ M_{rc} & M_{rr} & 0 \\ M_{lc} & 0 & M_{ll} \end{bmatrix} \quad (3.73)$$

The stiffness matrix is obtained from subtracting equation 3.70 from equation 3.69 ($\delta V - \delta W_g$). Note that the resulting equation can be written as:

$$[\delta q_c^T \delta q_{dr}^T \delta q_{dl}^T] \begin{bmatrix} K_{cc} & 0 & 0 \\ 0 & K_{rr} & 0 \\ 0 & 0 & K_{ll} \end{bmatrix} \begin{Bmatrix} q_c \\ q_{dr} \\ q_{dl} \end{Bmatrix} \quad (3.74)$$

Hence, the stiffness matrix can be written as:

$$K_D = \begin{bmatrix} K_{cc} & 0 & 0 \\ 0 & K_{rr} & 0 \\ 0 & 0 & K_{ll} \end{bmatrix} \quad (3.75)$$

where

$$K_{cc} = \delta q_c^T \left(EI \int_0^{L_c} \phi_c'' \phi_c''^T q_c dx - T \int_0^{L_c} \phi_c' \phi_c'^T q_c dx \right)$$

$$K_{rr} = (EI)_{mr} \int_0^{L_{gr}} \phi_{dr}'' \phi_{dr}''^T q_{dr} dx$$

$$K_{ll} = (EI)_{ml} \int_0^{L_{gl}} \phi_{dl}'' \phi_{dl}''^T q_{dl} dx$$

The virtual work of the wind force is defined as:

$$\delta W_{nc} = \int_0^{L_c} F(t) \delta w_c dx \quad (3.76)$$

Discretizing equation 3.76 and taking its variation yields:

$$\delta W_{nc} = \delta q_c^T \int_0^{L_c} F(t) \phi_c dx \quad (3.77)$$

where $F(t)$ is the uniform wind force across the conductor.

Equation 3.69 can be written as:

$$[\delta q_c^T \delta q_{dr}^T \delta q_{dl}^T] \begin{bmatrix} W_{cc} \\ W_{rr} \\ W_{ll} \end{bmatrix} \quad (3.78)$$

where

$$\begin{aligned} W_{cc} &= g[m_{dr}(\phi_c^* + L_{gr}\phi_c^*) - m_{dl}(\phi_c^* - L_{gl}\phi_c^*)] \\ W_{rr} &= g m_{dr}\phi_{dr}^* \\ W_{ll} &= g m_{dl}\phi_{dl}^* \end{aligned}$$

Finally, using equation 3.72, 3.74, 3.76 and 3.78, the equation of motion is expressed as follows:

$$\begin{bmatrix} M_{cc} & M_{cr} & M_{cl} \\ M_{rc} & M_{rr} & 0 \\ M_{lc} & 0 & M_{ll} \end{bmatrix} \begin{Bmatrix} \ddot{q}_c \\ \ddot{q}_{dr} \\ \ddot{q}_{dl} \end{Bmatrix} + \begin{bmatrix} K_{cc} & 0 & 0 \\ 0 & K_{rr} & 0 \\ 0 & 0 & K_{ll} \end{bmatrix} \begin{Bmatrix} q_c \\ q_{dr} \\ q_{dl} \end{Bmatrix} = \begin{bmatrix} W_{cc} \\ W_{rr} \\ W_{ll} \end{bmatrix} + \int_0^{L_c} F(t)\phi_c dx \quad (3.79)$$

Chapter 4

Dynamic of Single Conductor Without Damper

4.1 Description of the Matlab Codes

This section describes the MATLAB codes (Appendix B.1). The overall codes consists of 5 subroutines, a main function for the free vibration, and a main function for the simulation. The subroutines and the main functions are described as follows:

1. *Matrix KM* is the subroutine where the mass and the stiffness matrices are computed. It consists of the mass and stiffness matrices of the element damper (M_D and K_D) and the mass and stiffness matrix of the element without damper (M , K).
2. *Assemble KM* this subroutine assembles the element mass and stiffness matrices. The output is a global mass and stiffness matrices and the size of these matrices depends on the number of element considered.
3. *Apply BC* is the subroutine used for applying boundary conditions.
4. *Free vibration* calls all the subroutines described above and then computes the natural frequencies.

5. *Linearize*: This subroutine is used as a state space equation to convert the second order ODE (ordinary differential equation) to the first order ODE so that the function *ode45* can be used in the subroutine *Mainsimulation*.
6. *Mainsimulation*: This subroutine determines the response of the system.

4.1.1 Modal Analysis

4.1.1.1 Description of the Conductor Characteristics

The parameters used for the purpose of the modal analysis are taken from Ref. [10] in order to allow the comparison of the obtained simulation results to the corresponding experimental results. The conductor has the following characteristics:

1. Mass per unit length, $m = 0.8127 \text{ kg/m}$.
2. Flexural rigidity $EI_{min} = 11.07 \text{ N.m}^2$.
3. Mechanical load (tension) in the cable, $T = 15860 \text{ N}$ and 10700 N .
4. Three span lengths were considered, $L = 13.385 \text{ m}$, 32.3 m , and 65.355 m .

It should be noted that the minimum flexural rigidity is used in all computations for the sake of safety since the worst case scenario of having a failure would result for EI_{min} .

4.1.1.2 Methodology and Results

With respect to the finite element results, the mass and stiffness matrices derived in chapter 3 are incorporated in the MATLAB codes. For the purpose of validating the model, the simply supported boundary condition is employed. The first five natural frequencies are tabulated in Table 4.1. The exact or theoretical natural frequencies are obtained using equation 3.14. As it can be seen, the natural frequencies found from the finite element method are identical to those established from the exact solution. The percentage of error for the 13.385 m span length is 1% and the remaining two span lengths resulted in no error.

Table 4.1: Finite element (FE) and theoretical (exact) natural frequencies.

Mode	Natural frequency (Hz)					
	L = 13.385m		L = 32.3m		L = 65.355m	
	T = 15860N		T = 10700N		T = 15860N	
	FE	Exact	FE	Exact	FE	Exact
1	5.21850	5.2185	1.7762	1.7762	1.0688	1.0688
2	10.4380	10.4376	3.5525	3.5525	2.1375	2.1375
3	15.6580	15.6579	5.3289	5.3289	3.2063	3.2063
4	20.0881	20.8801	7.1054	7.1054	4.2751	4.2751
5	26.1080	26.1046	8.8822	8.8821	5.3439	5.3439

In Ref. [10], a prototype of the overhead transmission lines testing was performed. The experimental data were obtained using five accelerometers placed along the cable at $L/2$, $3L/8$, $L/4$, $L/8$, and $L/16$ with a system excitation from an impact hammer. The first five natural frequencies of the three span lengths found experimentally are tabulated in the table below.

Table 4.2: Experimental natural frequencies.

Mode	Natural frequency (Hz)		
	L = 13.385m	L = 32.3m	L = 65.355m
	T = 15860N	T = 10700N	T = 15860N
1	5.2200	1.7760	1.1159
2	10.4603	3.5179	2.1234
3	15.6638	5.2539	3.1829
4	20.9681	7.0183	4.2509
5	26.1545	8.7359	5.3081

The comparison of the experimental and the finite element results is illustrated in Figure 4.1. From this figure, it is evident that both results are very close. The percentage error for 13.385 m, 32.3 m, and 65.335 m span lengths is found to be 1.21%, 1.3%, and 0.32%, respectively. The discrepancies in the results are due to the fact that the non-linearity effect and the conductor torsion were not accounted in the mathematical formulation.

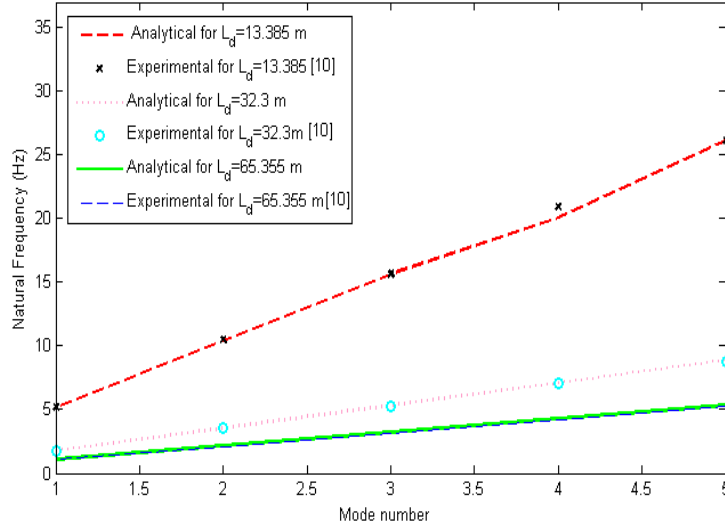


Figure 4.1: Comparison of the analytical and experimental results.

4.2 Forced Vibration Analysis

4.2.1 Conductors Selection and Transmission Lines Condition

Two common conductors used for transmission lines with very different characteristics are selected. The conductor 240/40 sq.mm ACSR (26/7) and 1840 Kcmil drake ACSR (72/7) are chosen from the EPRI handbook [1]. The first conductor would be used in both parts of the analysis since its diameter falls within the range of the Stockbridge damper requirements. The second conductor is only used in the first part to verify the dynamics of the conductor with higher flexural rigidity.

With respect to the applied force, it was indicated in chapter two that the wind force applied on the conductor can be approximated by equation 2.8 since past investigations have shown that the conductor behaves as a rigid cylinder. Hence, the force by unit span length is calculated for each conductor using this equation and taking the average value of the lift coefficient to be 0.3 and the density of air to be approximately 1.2 kg/m^3 at 20° C . Should this lift coefficient of 0.3 be used, the

maximum amplitude of vibration cannot exceed the diameter of the conductor. It is important to note that the expression of the wind force F_l is in terms of the wind speed and it is the amplitude of the sinusoidal wind force in equation 2.8.

The span length for a typical transmission line can vary from 100-1000 m, and a span length of 372 m is used in this analysis.

Conductor 240/40 sq.mm ACSR (26/7) consists of 26 strands of aluminum with a diameter of 3.439 mm/strand and 7 strands of steel with a diameter of 2.675 mm/s-trand. This conductor has the following characteristics:

1. Mass per unit length, $m = 0.987 \text{ kg/m}$.
2. Overall diameter, $D = 21.9 \text{ mm}$.
3. Rated tensile strength, $RTS = 86,400 \text{ N}$ (20% $RTS = 17280 \text{ N}$; 25% $RTS = 21600 \text{ N}$).
4. Minimum flexural rigidity, $EI_{min} = 16 \text{ Nm}^2$.
5. Maximum safe bending amplitude at 25% RTS , and 20% RTS with $Y_{bsafe} = 0.310 \text{ mm}$, and 0.3 mm , respectively.
6. Applied lift force per unit length, $F_l = 0.00378v^2 \text{ (N/m)}$ (where v is the wind speed in m/s) for $v = 7 \text{ m/s}$, $F_l = 0.18522 \text{ N/m}$.

Conductor 1840 Kcmil drake ACSR (72/7) is one of the conductors that possesses the highest flexural rigidity and mass per unit length. It consists of 72 strands of aluminum with a diameter of 4.407 mm/strand and 7 strands of steel with a diameter of 2.068 mm/strand. The remaining characteristics of this conductor are:

1. Mass per unit length, $m = 2.91 \text{ kg/m}$.
2. Overall diameter, $D = 44.069 \text{ mm}$.
3. Rated tensile strength, $RTS = 200,600 \text{ N}$ (20% $RTS = 40120 \text{ N}$; 25% $RTS = 50150 \text{ N}$).

4. Minimum flexural rigidity, $EI_{min} = 97.11 \text{ Nm}^2$.
5. Maximum safe bending amplitude at 25% *RTS*, $Y_{bsafe} = 0.170 \text{ mm}$.
6. Applied lift force per unit length, $F_l = 0.007932v^2 \text{ (N/m)}$, for $v = 7 \text{ m/s}$,
 $F_l = 0.3886 \text{ N/m}$.

4.2.2 Simulation Results

Both conductors are only excited for higher modes since the Strouhal frequencies (for a wind speed varying 1 to 7 m/s) obtained for 240/40 sq.mm ACSR and 1840 Kcmil conductors varies from 9.52 to 66.666 Hz, and 4.53 to 31.75 Hz, respectively. The first mode of the 240/40 sq.mm ACSR (26/7) that fell within the range of the Strouhal frequency is found to be the 52nd mode with a frequency of 9.46 Hz. While the first excitation mode for the second conductor is the 29th mode with a frequency of 4.609 Hz. The wind velocity responsible for the first resonant frequency is, indeed, 1 m/s for both conductors.

For the purpose of determining the wind force, the velocity of the wind is taken to be 7 m/s. The highest uniform wind pressure is the worst case scenario since this resulted in the highest displacement. Hence the applied wind pressure is fixed for both conductors and it is determined to be 0.18522 N/m and 0.3886 N/m for the 240/40 sq.mm and 1840 Kcmil conductors, respectively.

The 240/40 sq.mm is considered first. Using the 20% rated tensile strength (RTS) condition, the maximum peak-to-peak amplitude is found to be 8.498 mm, 3.626 mm, and 1.175 mm for a frequency of 9.46 Hz, 21.979 Hz, and 66.66 Hz, respectively. The 25% RTS condition is also evaluated and it is determined that the first resonant frequency results in a peak-to-peak amplitude of 7.91 mm and the last resonant frequency produces a value of 1.056 mm. Figures 4.2 and 4.3 show the normalized amplitude of vibration with respect to the diameter (Y_{max}/D). From Figure 4.2 it is apparent that the normalized displacement is less than 0.2, implying that the amplitude of vibration is less than the diameter of the conductor by almost an order of magnitude, which is in agreement with the conclusion found in the literature.

With respect to 1840 Kcmil conductor at 20% RTS, the maximum peak-to-peak displacement across the conductor is determined to be 14.43 mm and 2.01 mm for the first and last resonant frequencies, respectively. Also, the conductor displays a peak-to-peak amplitude of 4.92 mm when it is excited at a resonant frequency of 13.017 Hz. Using the 25% RTS condition, the peak-to-peak amplitude is found to be 12.68 mm, 4.411 mm, and 1.80 mm with respect to the three natural frequencies listed previously. Figure 4.3 shows that the maximum normalized amplitude of vibration is less than 0.3.

An investigation is done on the 1840 Kcmil conductor to determine how the amplitude of vibration changes with respect to the span length. Three lengths are considered 300 m, 200 m, and 100 m. The peak-to-peak amplitude of vibration, y_{max} , corresponding to these three span lengths are determined to be 11.718 mm, 8.455 mm, and 4.418 mm, respectively. It is evident from Figure 4.4 that the normalized displacement decreases with decreasing span length. This fact is intuitive and in agreement with the literature. Thus, a shorter span is less susceptible to *Aeolian Vibration* than a longer span.

Furthermore, the effect of the tension was examined on the 240/40 sq.mm conductor. This is done by inspecting the amplitude of vibration at the midpoint for 10%, 20%, and 35% RTS while keeping the span length of the conductor and the forcing frequency fixed. The 10% RTS condition results in the highest amplitude of vibration and this value is less than one-half of the diameter of the conductor.

As shown in Figures 4.5 and 4.6, the maximum amplitude of vibration increases with decreasing tension for both high and low forcing frequencies. This is not surprising since the stiffness of the cable increases with increasing tension.

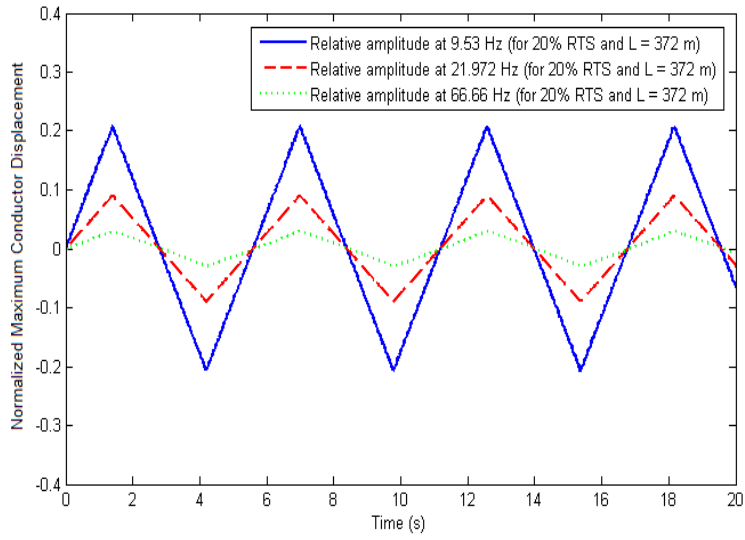


Figure 4.2: Effect of the frequency on the vibration amplitude of 240/40 sq.mm conductor (20% RTS).

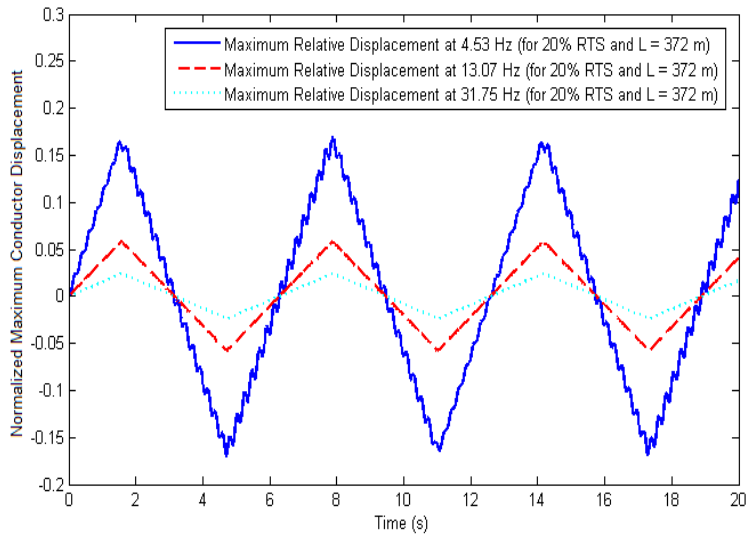


Figure 4.3: Effect of the frequency on the vibration amplitude of the 1840 kcmil conductor (20% RTS).

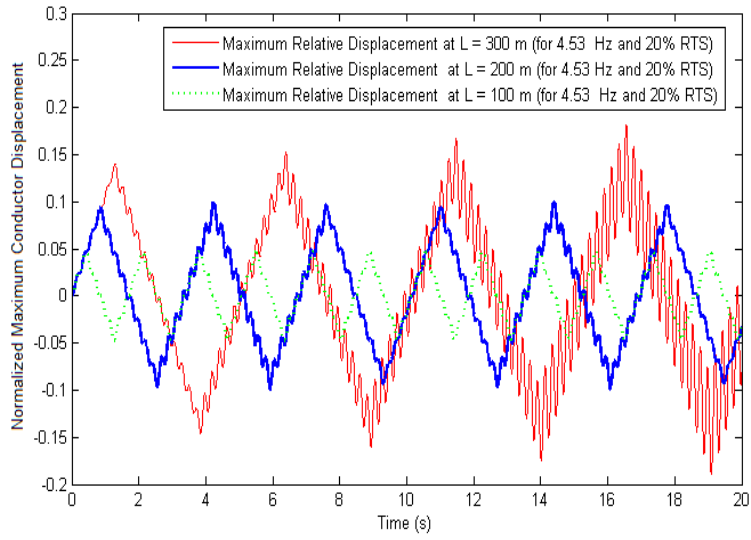


Figure 4.4: Normalized maximum displacement response of the 1840 Kcmil conductor for different span lengths.

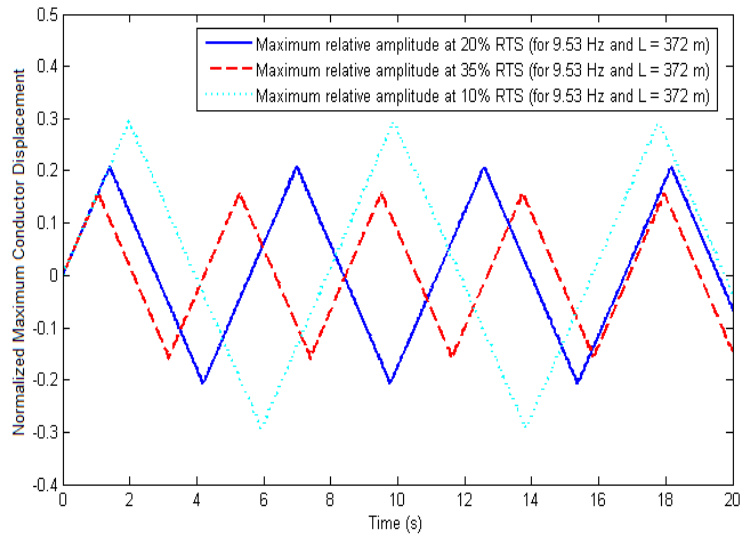


Figure 4.5: Effect of the tension on the vibration amplitude at low forcing frequency.

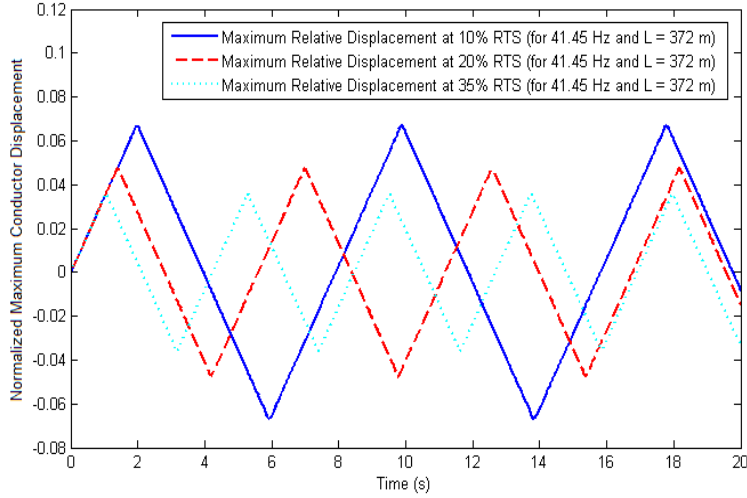


Figure 4.6: Effect of tension on the amplitude of vibration at higher forcing frequency.

4.2.3 Bending Amplitude

Recall that the bending stress is proportional to the bending amplitude. Hence in order to predict whether the conductor is safe, it suffices to determine the conductor bending amplitude and compare it to the specified limit. This bending amplitude is usually measured at a distance of 89 mm from the suspension clamp and it is given as $Y_b = Y_{max} \sin(0.089n\pi/L)$ [21] where n is the mode number and L is the span (L/n is the loop length).

For the 240/40 sq.mm conductor, the bending amplitude is determined to be 0.319 mm for 20% RTS. Note that this value corresponds approximately to the 52nd mode (9.46 Hz) which resulted in the highest maximum amplitude. The bending amplitude of the 1840 kcmil conductor is found to be 0.496 mm corresponding to the 29th mode for 25% RTS. The safe bending amplitudes are given as $Y_{bsafe} = 0.316$ mm at 20% RTS for 240/40 sq.mm conductor, and $Y_{bsafe} = 0.17$ mm at 25% RTS for 1840 Kcmil conductor. Comparing the calculated bending amplitudes to the safe bending amplitude, it is concluded that neither conductor is safe when dampers are not attached. Overall, the bending stress (bending amplitude) would exceed the endurance limit (safe bending) resulting in fatigue damage.

Chapter 5

Numerical Analysis of a Single Conductor Plus Dampers

5.1 Free Vibration Analysis

This section examines the validation of the mathematical model by comparing the natural frequencies obtained from MATLAB to those obtained using the commercial finite element analysis software, ANSYS.

5.1.1 Validation of the Model

A free vibration analysis is performed in ANSYS to validate the finite element model of the conductor with a damper. For the purpose of validating the model, the same parameters for the conductor used in section 4.1.1 are employed both in MATLAB and ANSYS. The damper has the following characteristics: $EI = 3.19 \text{ N/m}^2$; $m_{dr} = 4 \text{ kg}$ and $m_{dl} = 2.75 \text{ kg}$ (mass of damper on right and left) ; $\rho A_{dr} = \rho A_{dl} = 0.2 \text{ kg/m}$ (messenger mass per unit length on right and left); $L_{dr} = L_{dl} = 0.2 \text{ m}$; $h = 0.05 \text{ m}$ (height of clamp). The damper was placed at distance of 4.1 m from the left end of the conductor.

5.1.1.1 Simulation in ANSYS

Both the conductor and the messenger are modeled using *BEAM3* element, which is a two dimensional elastic beam element. The two counterweights at the ends are modeled as *mass21* elements, which is a two dimensional mass with rotational inertia. The clamp is modeled as *BEAM3*, but it is assumed that its mass per unit length is negligible compared to that of the conductor and the messenger. The span length is 13.375 m and the damper is placed at a distance of 4.1 m from the first node. The tension is considered to be zero so that the effect of the damper properties on the natural frequency can be isolated. Fixed boundary conditions are applied at the first and last finite element nodes of the conductor span by restricting the displacements along the x and y axis and the rotation about the z axis .

The first three modes are shown in Figures 5.1 to 5.3, the 10 th and 15 th mode are illustrated in Figure 5.5 and 5.6, and the 5 th mode with a closer look at the damper motion is delineated in Figure 5.4. The remaining modes of interest are shown in Appendix A. Unlike in chapter 4, it is evident from the figures below that the existence of symmetry has been disturbed by the presence of the damper in the system. This implies that the maximum amplitude does not occur at mid-span with respect to the first mode; also the displacement of the mid-span is not zero for the second mode. Furthermore, Figure 5.2 indicates that the antinode on the right of the vibration node is greater than the one on the left.

It is observed that the damper response starts occurring in the 5 th mode as illustrated in Figure 5.4. Taking the results of Figures 5.5 and 5.6 into consideration, it is evident that the damper dissipates all the energy of the conductor on the left and right side of the damper, respectively. Hence, it can be concluded that the 5 th and the 10 th mode of the system are, indeed, two of the resonant frequencies of the damper.

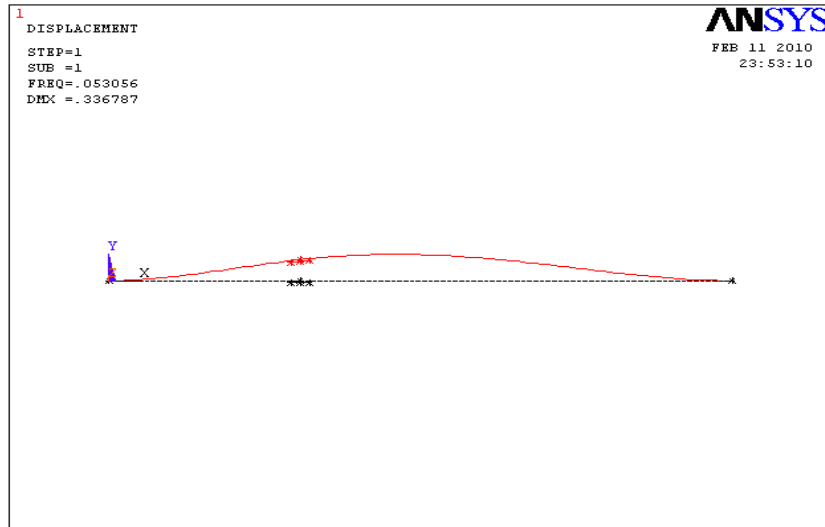


Figure 5.1: First mode of vibration of the conductor plus a damper.

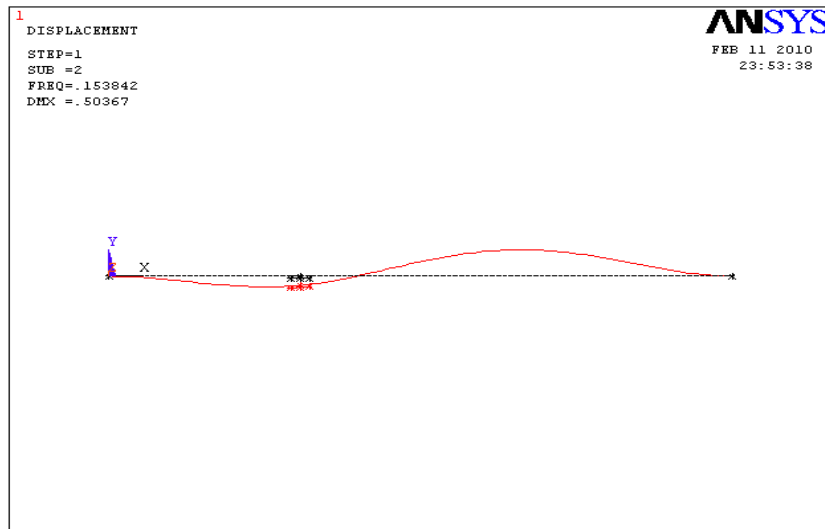


Figure 5.2: Second mode of vibration of the conductor plus a damper.

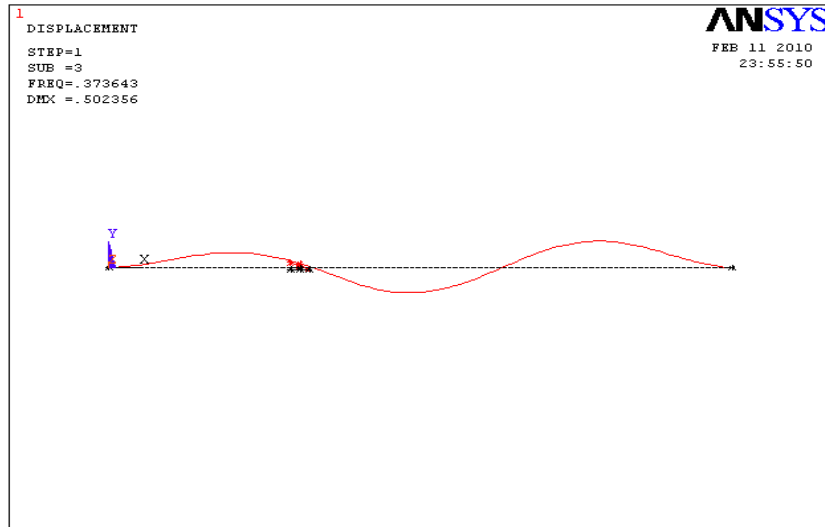


Figure 5.3: Third mode of vibration of the conductor plus a damper.

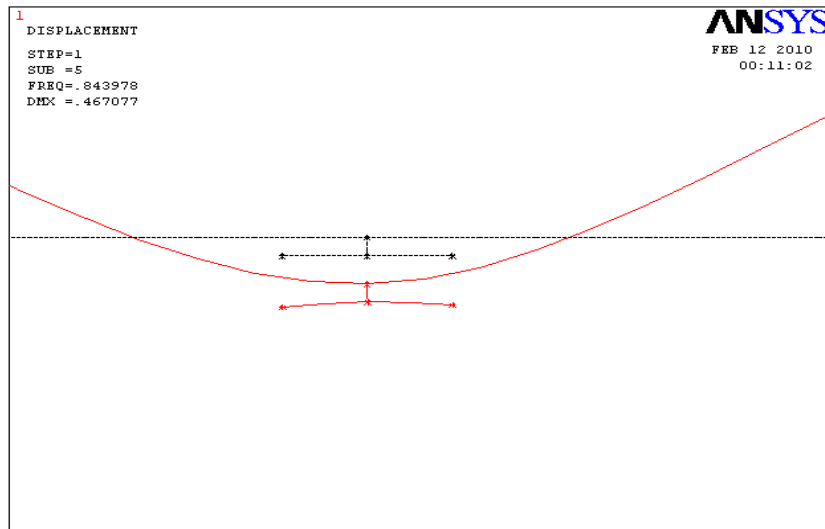


Figure 5.4: Fifth mode with a closer look at the damper.

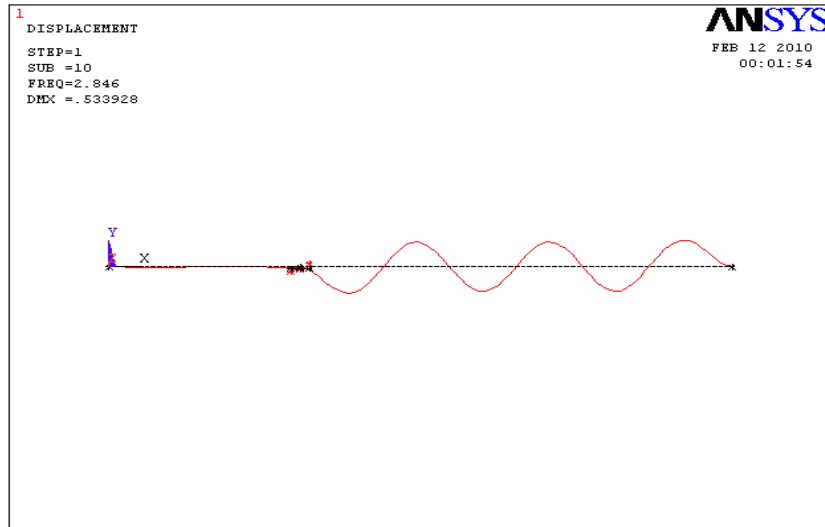


Figure 5.5: Tenth mode of vibration of the conductor plus a damper.

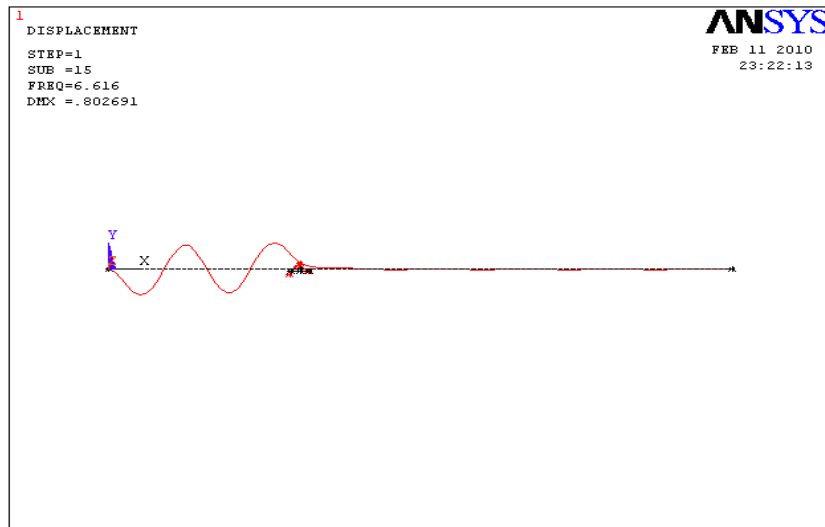


Figure 5.6: Fifteenth mode of vibration of the conductor plus a damper.

5.1.1.2 Numerical Analysis in MATLAB

The same procedure described in subsection 4.1.1 is performed in this section except that a damper is attached to the conductor. Table 5.1 compares the natural frequencies of the same conductor used in Ref. [10] with and without a damper. The addition of the damper in the span decreases the natural frequencies of the system. This is not surprising as it is known that natural frequency is inversely proportional to the mass.

Table 5.1: Comparison of MATLAB natural frequencies of the conductor with and without damper for $L = 13.375$ m and $T = 0$ N.

Mode	Natural frequency (Hz)	
	Without damper	With damper
1	0.07335	0.0531
2	0.202	0.1501
3	0.397	0.365
4	0.657	0.629
5	0.984	0.845
6	1.381	1.247
10	3.98	2.84

Table 5.2 shows the results of the first six natural frequencies and the 10th natural frequency obtained through both simulation methods. The first 20 natural frequencies versus the mode numbers of both MATLAB and ANSYS are plotted in Figure 5.7. It is apparent from this figure that the results are very similar. The average percentage error is found to be 1.02%. The discrepancy associated with the results is due in part to the assumption that the clamp has negligible mass and stiffness. Both mass and stiffness are taken into consideration in ANSYS finite element analysis. However, since the length of the clamp is very small (0.05 m) compared to the length of the messenger (0.35 m) and to the conductor (13.375 m), the error is insignificant.

Table 5.2: Comparison of ANSYS and MATLAB natural frequencies of the conductor with damper for $L = 13.375$ m and $T = 0$ N.

Mode	Natural frequency (Hz)	
	ANSYS	MATLAB
1	0.0531	0.0531
2	0.153	0.1501
3	0.373	0.365
4	0.621	0.629
5	0.845	0.845
6	1.247	1.247
10	2.84	2.84

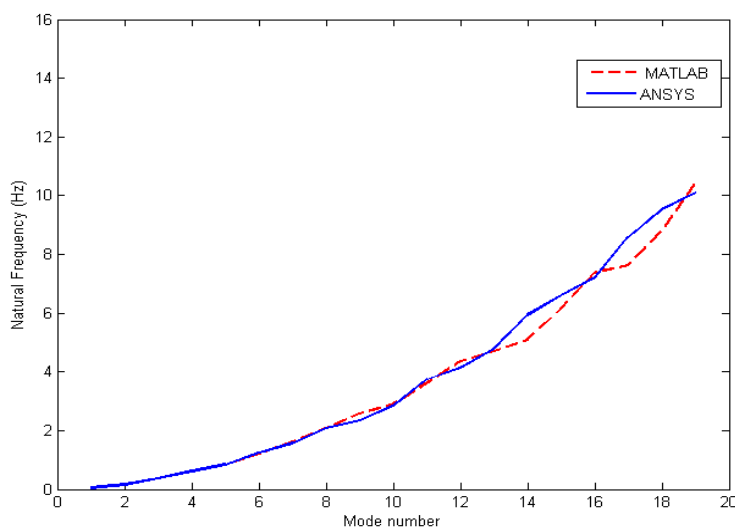


Figure 5.7: ANSYS and MATLAB natural frequencies comparison.

5.1.2 Effect of the Mass and the Location of the Damper on the Natural Frequency

The conductor 240/40 sq.mm from section 4.2.1 is employed hereafter. The characteristics of the damper are as follows [31]:

1. The minimum flexural rigidity $EI_{min} = 3.19$ N/m²
2. Messenger mass per unit length, $m = 0.498$ kg

3. Length of the messenger on one side $l = 0.15 - 0.2 \text{ m}$
4. Mass of the counterweight, m_{dr} or m_{dl} varies from 0.856 to 4 kg
5. Counterweight mass moment of inertia, I_{dr} or I_{dl} varies from 0.001814 to 0.00741 kgm^2

The natural frequencies are determined for four different cases as illustrated in Figure 5.8. It is plausible that the natural frequencies are not considerably affected when one damper is attached to the conductor because the tension is very large compared to the damper parameters. However, when two dampers are attached, the natural frequencies above 50 Hz tend to diminish considerably.

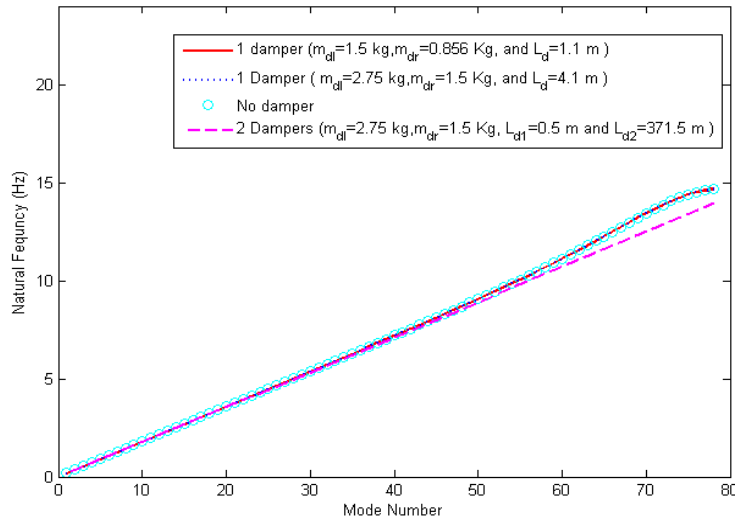


Figure 5.8: Effect of damper properties on the natural frequencies.

5.2 Force Vibration Analysis

The force vibration analysis is presented in two subsections. The first subsection deals with the response of the conductor with one damper attached and the second deals with the conductor response when two dampers are positioned on the conductor.

5.2.1 Response of the Conductor With One Damper

As mentioned above, the 240/40 sq.mm was selected for the purpose of the numerical analysis, so the applied wind force is the same as that calculated in section 4.2.1 ($F_l = 0.18522$ N/m). In the first part of this subsection, the effect of the damper mass on the response is established. The second part deals with the impact of the vibration frequency on the response. Finally, the effect of the damper location is examined in the last section.

It is important to note that the figures in this section also show the peak-to-peak displacement normalized with respect to the diameter, Y . The normalized peak-to-peak amplitudes at the finite element nodes of interest are describes as:

1. Y_2 denotes the normalized peak-to-peak amplitude evaluated at the second finite element node.
2. Y_f represents the normalized peak-to-peak amplitude evaluated at the penultimate finite element node.
3. Y_{max} is the finite element node corresponding to the maximum normalized vibration amplitude along the conductor.
4. Y_{mid} corresponds to the normalized peak-to-peak amplitude at the mid-span.
5. Y_d is the normalized peak-to-peak amplitude of the damper clamp.
6. Y_{dr} denotes the normalized peak-to-peak amplitude of the right side counterweight.
7. Y_{dl} is the normalized peak-to-peak amplitude of the left side counterweight.

5.2.1.1 Effect of the Damper Mass

In this section, the damper is positioned at a distance $L_d = 1.1$ m. The response along the conductor was determined by varying the mass of the damper from 0.856 to 4 kg.

The peak-to-peak amplitude at various points along the conductor versus the total damper mass is shown in Figure 5.9. This figure shows that the conductor maximum vibration amplitude slightly increases as the damper mass becomes larger, but the mid-span displacement amplitude, Y_{mid} , is almost constant. Further, Y_2 increases linearly with the damper mass, whereas Y_f decreases.

Figure 5.10 shows that the peak-to-peak vibration amplitude of both counterweights also increases with increasing damper mass and the damper with the lowest mass results in the largest peak-to-peak amplitude.

The peak-to-peak response along the conductor is illustrated in Figure 5.11. This figure shows that the amplitude of vibration peaks to a maximum at a point on the conductor and then decreases. Note that this point is the finite element node associated with the resonant mode. Furthermore, when the two counterweight masses are balanced, the amplitude of vibration is larger. This implies that a symmetric damper dissipates less energy than an asymmetric damper.

Most importantly, Figure 5.11 shows that having the larger mass to either face the tower or the mid-span can slightly influence the vibration amplitude. The magnitude of the maximum displacement slightly increases when the larger counterweight is placed on the right side facing the mid-span. Thus, it is preferable to face the larger counterweight to the tower albeit doing so does not significantly reduce the maximum vibration amplitude.

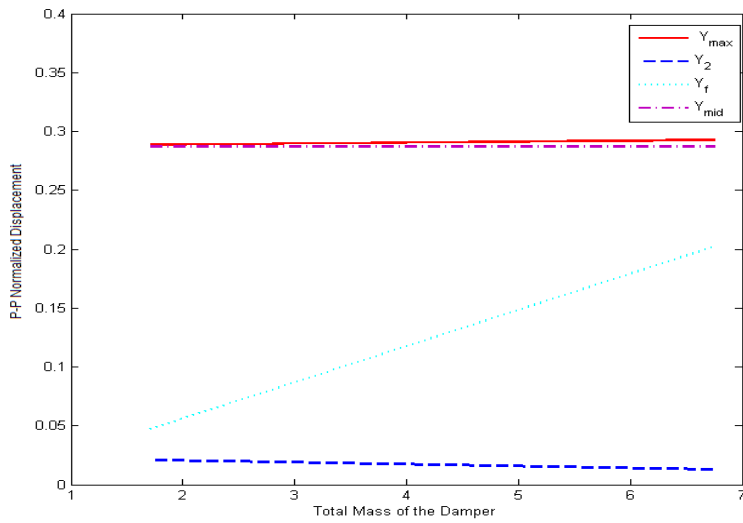


Figure 5.9: Effect of the total mass on the conductor response for $f = 9.53\text{Hz}$ and $L_d = 1.1\text{ m}$.

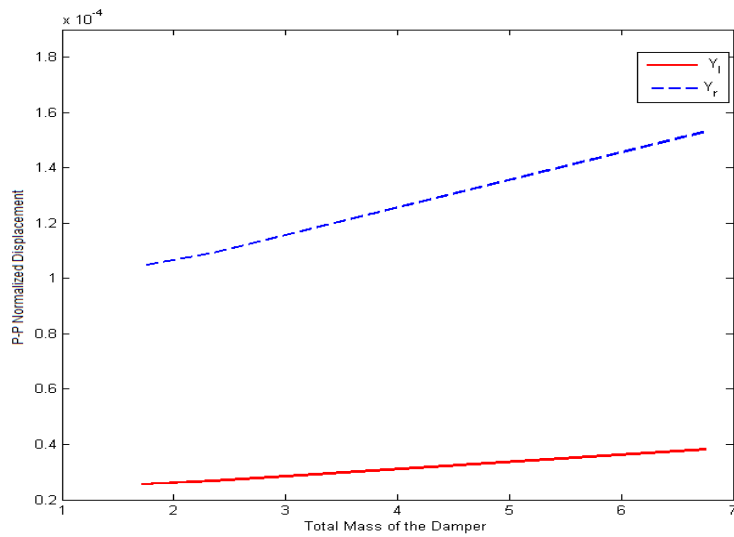


Figure 5.10: Effect of the total damper mass on the damper response for $f = 9.53\text{ Hz}$ and $L_d = 1.1\text{ m}$.

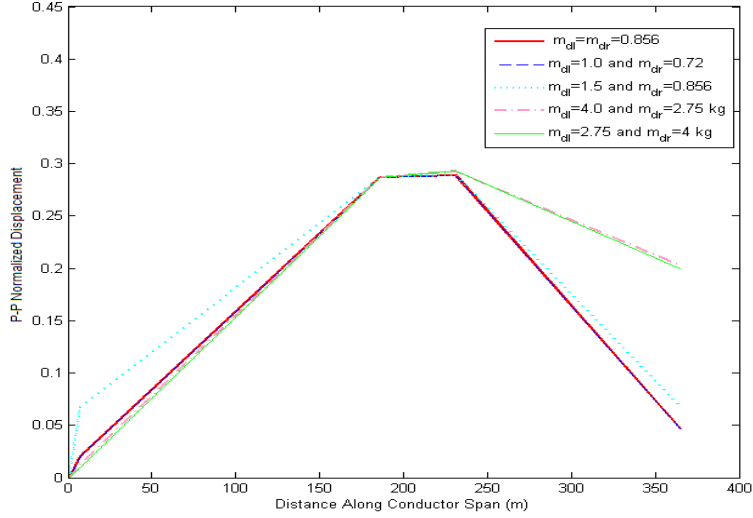


Figure 5.11: Normalized peak-to-peak displacement, as function of distance x_c along the conductor, for $f = 9.53$ Hz and $L_d = 1.1$ m.

5.2.1.2 Effect of the Forcing Frequency on the Response

This section describes the effect of the vibration frequency on the conductor response when a damper is attached at $L_d = 0.898$ and 5 m. The mass of the damper on the right and left side are taken to be 0.856 and 1.5 kg, respectively. The remaining properties are the same as those in section 5.1.2.

Figures 5.12 and 5.14 show that the amplitudes of vibration, Y_{max} and Y_{mid} , decrease with increasing vibration frequency. On the other hand, the displacement amplitudes, Y_2 and Y_f , can increase, decrease, or remain constant as the vibration frequency is increased.

The amplitude of vibration of the damper is shown in Figures 5.13 and 5.15 for $L_d = 0.898$ and 5 m, respectively. The plots in these figures display the same trends. The damper vibration amplitude increases with the forcing frequency. This can be explained by noting that Stockbridge dampers dissipate the most energy at higher vibration frequencies. Overall, it can be concluded that vibration amplitude throughout the conductor span length decreases as the excitation frequency increases.

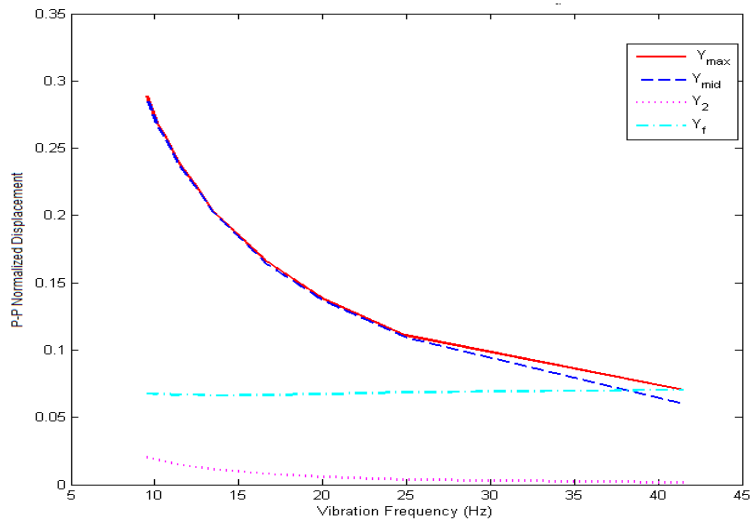


Figure 5.12: Conductor peak-to-peak displacement, as function vibration frequency for $L_d = 0.898$ m.

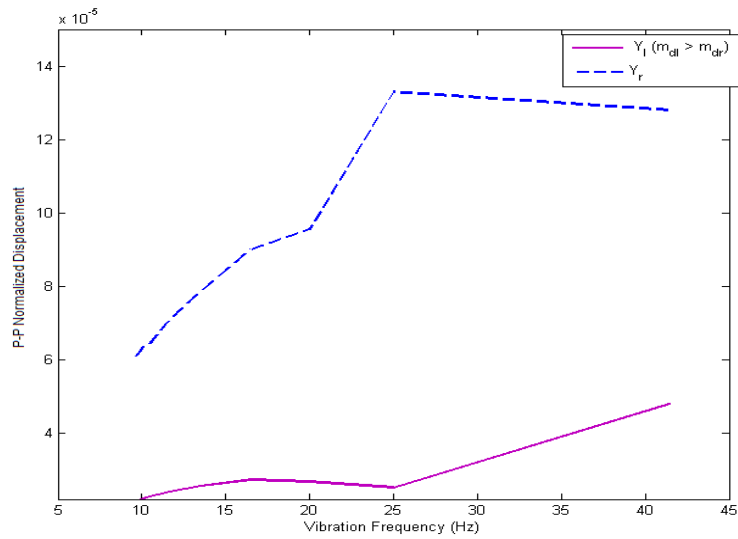


Figure 5.13: Damper peak-to-peak displacement, as function of vibration frequency for $L_d = 0.898$ m.

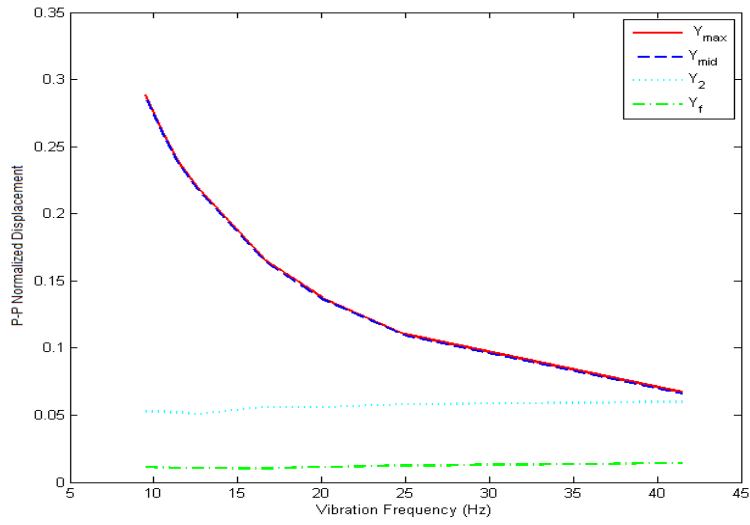


Figure 5.14: Conductor peak-to-peak displacement, as function of vibration frequency for $L_d = 5$ m.

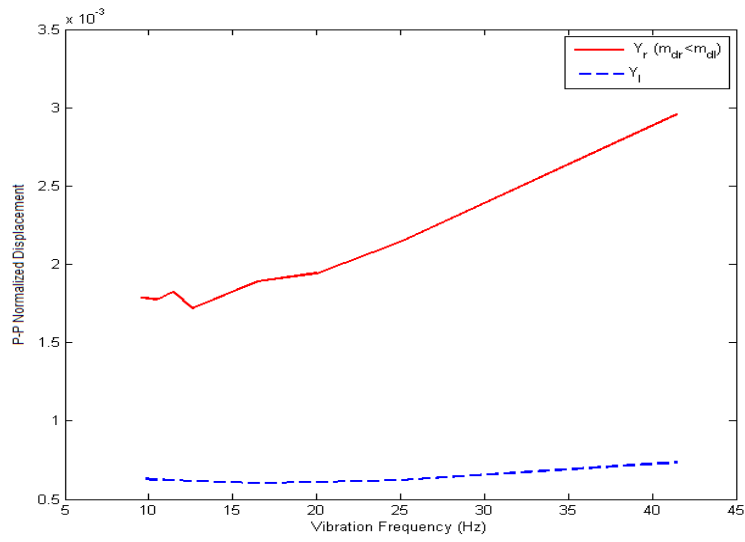


Figure 5.15: Damper counterweights peak-to-peak displacement, as function of vibration frequency $L_d = 5$ m.

5.2.1.3 Effect of the Damper Location on the Response

The vibration response is determined for various damper locations L_d for three fixed frequencies $f = 9.53, 14.0,$ and 41.45 Hz. The same damper properties from the previous section are used in this case.

For a constant forcing frequency, $f = 9.53$ Hz, the results in Figure 5.16 indicates that Y_{max} is minimum as the location of the damper L_d is increased from 0.1 to 7 m, but it increases as L_d is greater than 7 m. The maximum normalized amplitude at the mid-span Y_{mid} is also a minimum as the damper is moved from 0.1 to 7 m and increases monotonically when L_d is greater than 7 m.

Furthermore, Figure 5.16 shows that the maximum normalized displacement of the second node and the penultimate node on the conductor are approximately the same for $L_d = 5$ to 7 m. Note that this range is within the range corresponding to the minimum Y_{max} value. When the conductor is excited at 9.53 Hz, it is evident that positioning the damper between 5 to 7 m reduces the maximum amplitude of vibration and stabilize the vibration along the conductor. It is important to note that this damper location range corresponds to 70 to 95% of the loop length with respect to the 9.53 Hz forcing frequency.

Figure 5.17 shows that the maximum normalized displacement value is reduced for a constant vibration frequency of 14.0 Hz compared to Figure 5.16. However, the optimum damper location range is within the optimum range in Figure 5.16, $L_d = 2.5$ to 6.6 m. Figure 5.17 also shows that the mid-span amplitude remains relatively constant compared to the maximum amplitude. It was also apparent that the normalized displacements Y_2 and Y_f , approaches the same value for $L_d = 6.6$ m as illustrated in Figure 5.18. The optimum range corresponds to 51 to 133% of the loop length associated with this forcing frequency.

For a constant forcing frequency of 41.45 Hz, Figure 5.19 shows a considerable drop in the normalized maximum displacement of the conductor. This figure also shows that the range of the optimum damper location corresponding to $f = 41.45$ Hz is within the optimum range determined in Figure 5.16 ($L_d = 2.1$ to 4.2 m). This range corresponds to 125 to 264% of the loop length associated with 41.45 Hz. With

respect to the mid-span amplitude and the amplitude near the ends, the observations from Figure 5.16 are in agreement with those from Figures 5.17, 5.18, 5.19, and 5.20.

In Figures 5.21, 5.22, and 5.23, the normalized displacement of both counterweights for the three aforementioned forcing frequencies are illustrated. The results indicate that the normalized amplitude of both counterweights is maximal in the vicinity of the optimum damper location range. This is intuitive as it is evident that the dissipation energy of the damper increases with the displacement of the damper. Hence, this confirms that the efficiency of the damper is considerably dependent on the damper location.

It should be noted that when the damper was positioned beyond 7 m, Y_{max} started increasing monotonically as illustrated in Figures 5.16, 5.17, and 5.19. This is because the damper is approaching the vibration node of the loop length ($L_{52} = 7.15$ m) corresponding to the dominant mode ($f = 9.53$ Hz); its efficiency diminishes and the maximum amplitude increases. Irrefutably, the optimum location of the damper varies with the forcing frequency. However, each vibration frequency considered in this section shows that the vibration amplitude reduces considerably when the damper is located within $L_d = 2.5$ to 4.2 m.

To further improve our understanding of the effect of the damper location on the conductor motion, Figure 5.24 and Figure 5.25 depict the conductor and damper counterweight displacement, respectively, when the location of the damper is varied over the whole span length. Based on these plots, it is concluded that a damper is only efficient when it is located in the immediate vicinity of the span ends closer to the tower.

The largest peak-to-peak vibration amplitude corresponding to the range $L_d = 2.5$ to 4.2 m is $y_{max} = 6.338$ mm. Hence, the corresponding bending amplitude is approximately $y_b = 0.248$ mm. Note that this bending amplitude is less than the safe bending amplitude $y_{safe} = 0.332$ mm. Therefore, the conductor would be certainly safer from fatigue damage by locating the damper within $L_d = 2.5$ to 4.2m.

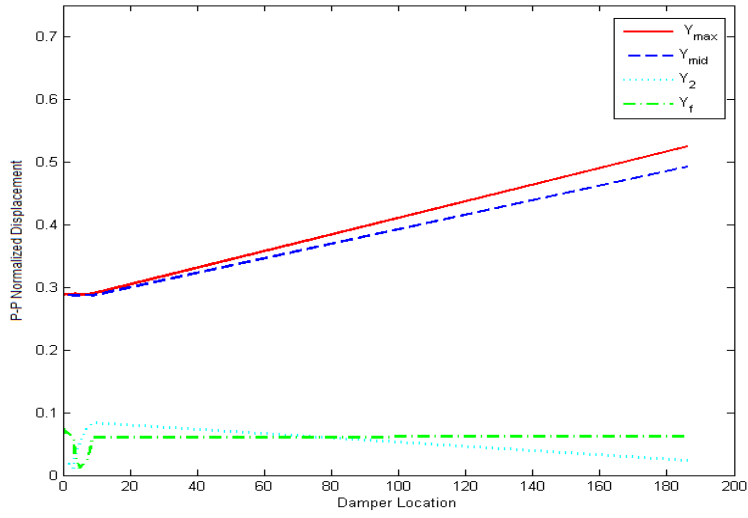


Figure 5.16: Conductor peak-to-peak displacement as function of the damper location for $f = 9.53$ Hz.

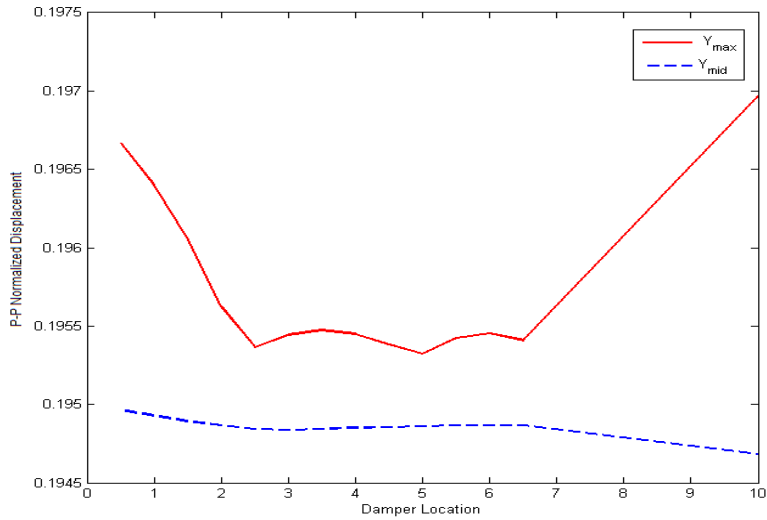


Figure 5.17: Conductor peak-to-peak displacement as function of the damper location for $f = 14.0$ Hz.

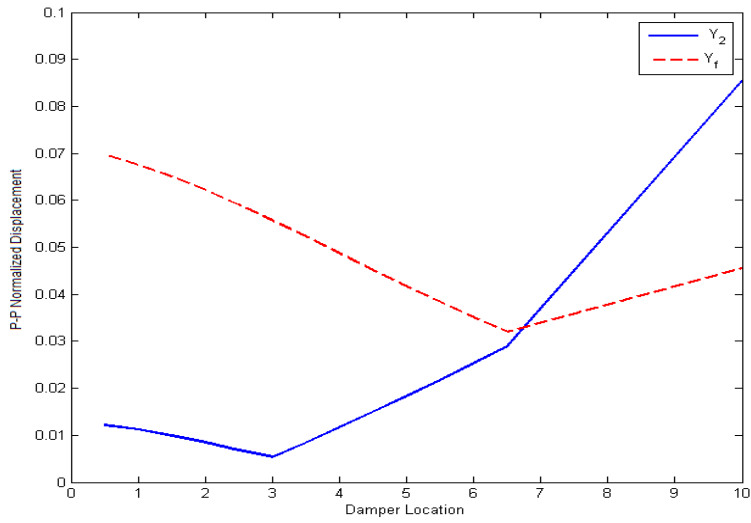


Figure 5.18: Conductor peak-to-peak displacement near span ends as function of the damper location, for $f = 14.0$ Hz.

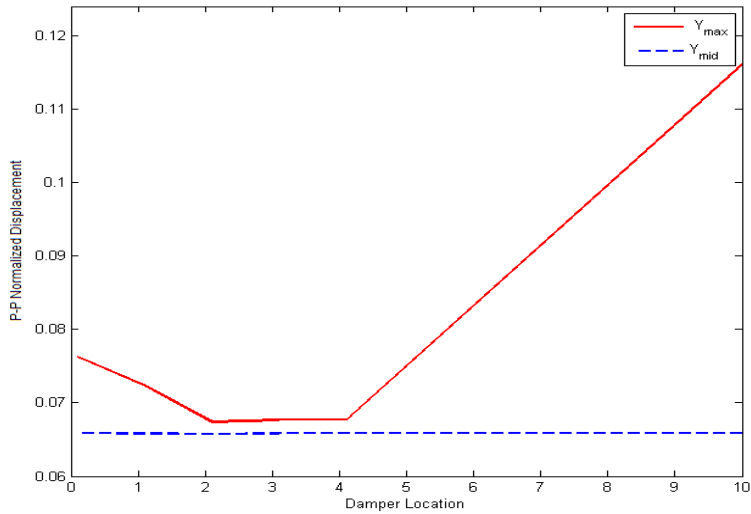


Figure 5.19: Conductor peak-to-peak displacement as function of the damper location for $f = 41.45$ Hz.

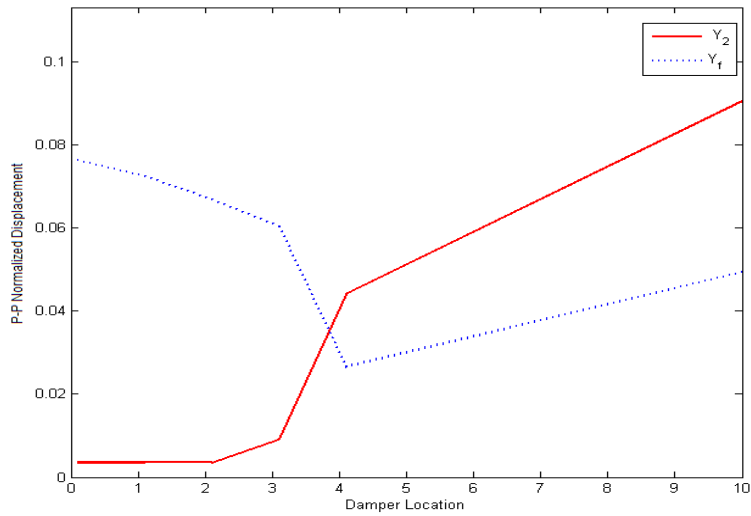


Figure 5.20: Conductor peak-to-peak displacement near span ends as function of the damper location for $f = 41.45$ Hz.

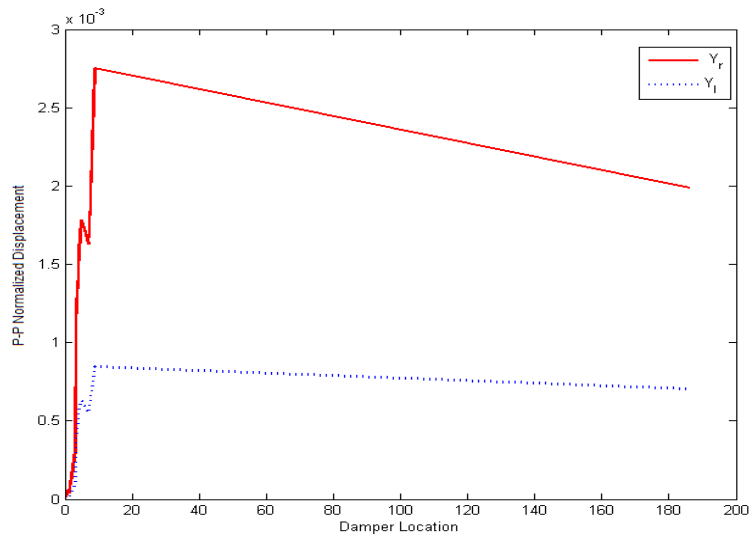


Figure 5.21: Damper peak-to-peak displacement as function of the damper location for $f = 9.53$ Hz.

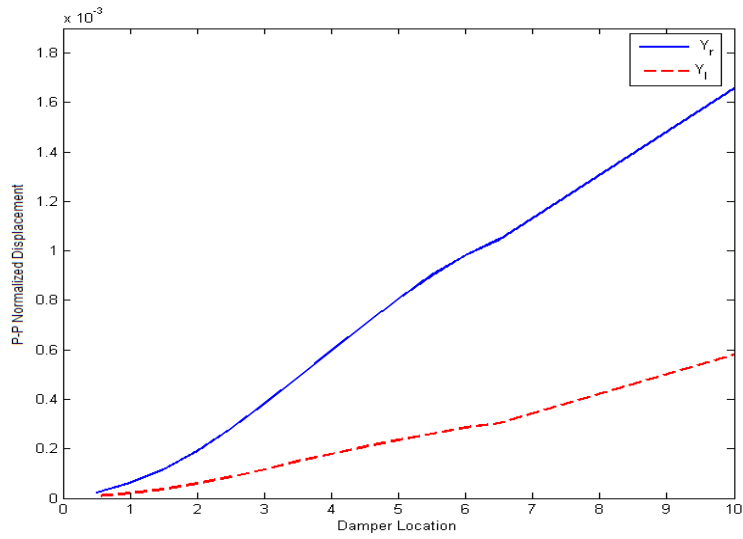


Figure 5.22: Damper peak-to-peak displacement as function of the damper location for $f = 14.0$ Hz.

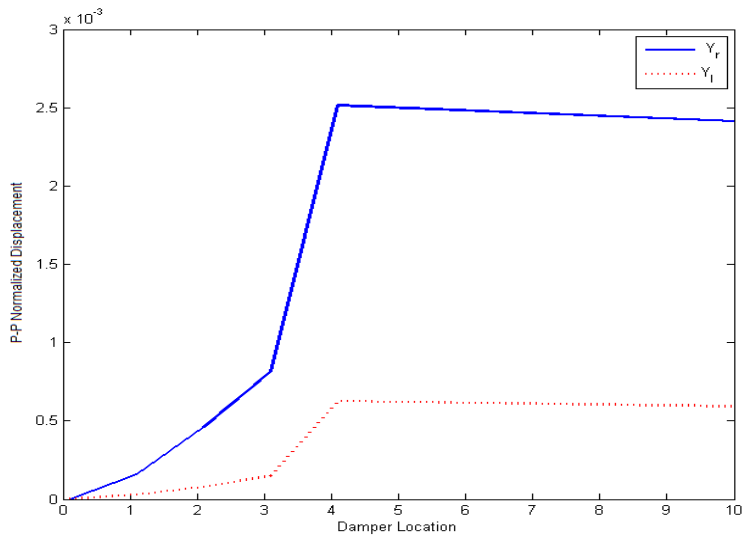


Figure 5.23: Damper peak-to-peak displacement as function of the damper location for $f = 41.45$ Hz.

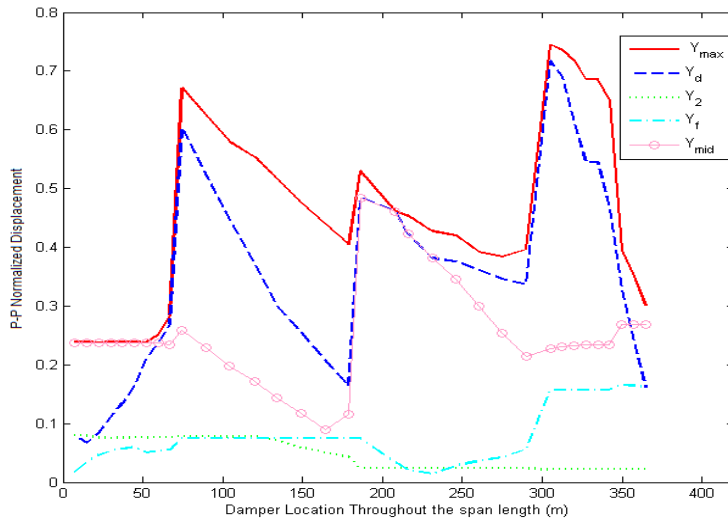


Figure 5.24: Conductor peak-to-peak displacement vs. damper location throughout the span length, for $f = 10.10$ Hz.

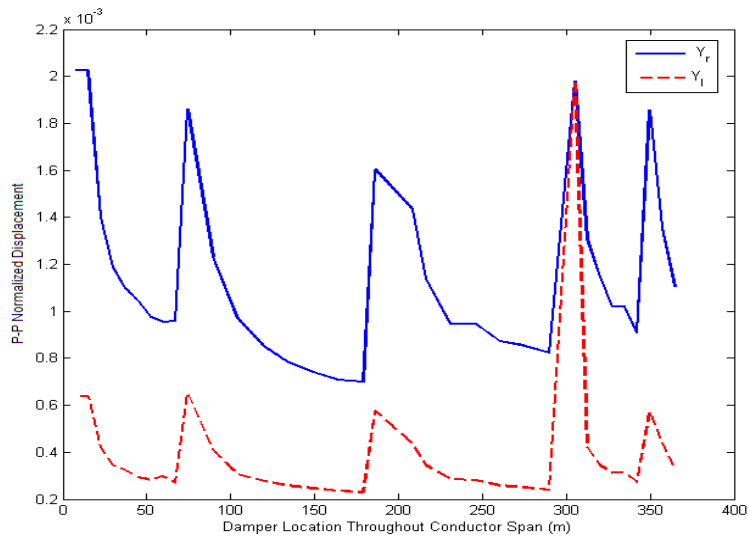


Figure 5.25: Damper peak-to-peak displacement vs. damper location throughout the span length, for $f = 10.10$ Hz.

5.3 Response of a Conductor with Two Dampers

The same damper properties from the previous section are also employed in this section. Further, the vibration frequency $f = 9.53$ Hz is selected and there is no need to examine the other two vibration frequencies employed in the previous section. Two dampers are always positioned symmetrically about the mid-span of the conductor.

As illustrated in Figure 5.26, the normalized maximum displacement on the conductor dropped significantly as a result of attaching two dampers to the conductor. It is evident that Y_{max} follows a parabolic-like variation with L_d . It decreases monotonically as the location of the damper varies from $L_d = 0$ to 2.5 m and remains relatively constant for $L_d = 2.5$ to 5.5 m. Finally, it increases as the damper is placed beyond 5.5 m.

Further, Figure 5.27 shows that the maximum displacement near both ends are minimum when the damper is approximately positioned at $L_d = 5.5$ m. Here, the damper tends to stabilize the vibration throughout the conductor.

In Figure 5.28, the normalized counterweights vibration amplitudes of both dampers are delineated. It indicates that the normalized amplitudes of the two dampers are not always the same. Instead, the vibration amplitude of either damper can be greater or less than that of the other damper, depending on the location of the dampers.

The lowest peak-to-peak conductor vibration amplitude, y_{max} , is 1.657 mm when the dampers are positioned at $L_{d1} = 2.6$ m and $L_{d2} = 369.4$ m. Whereas, the lowest y_{max} for one damper is determined to be 6.31 mm when the damper was positioned at 1.1 m. Comparing the two, it is evident that the use of two dampers, positioned at the best possible locations, would notably reduce the maximum vibration amplitude. Moreover, the conductor bending amplitude with respect to the two damper is found to be $y_b = 0.06225$ mm, which is overly less than that when only one damper is used ($y_b = 0.247$ mm). Most importantly, it is substantially less than the safe bending amplitude, $y_{safe} = 0.332$ mm. Conclusively, the conductor would be much safer from fatigue failure when two dampers, with the best conductor-damper combination, are employed.

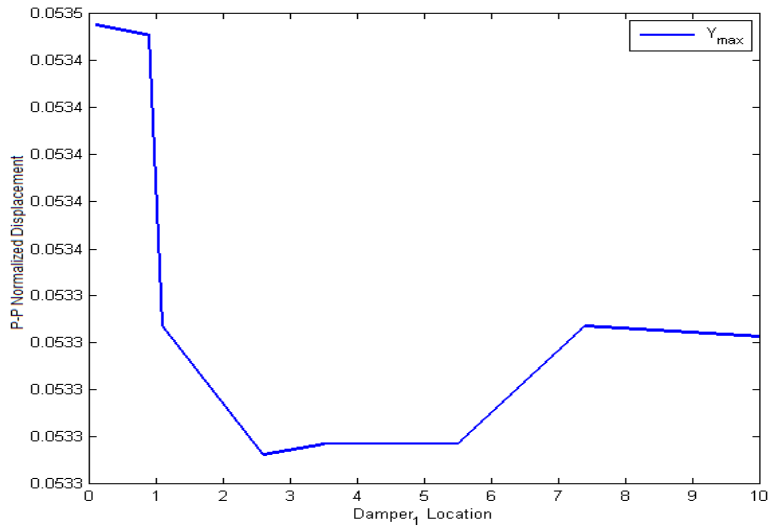


Figure 5.26: Conductor peak-to-peak displacement vs. damper location for $f = 9.53$ Hz (2 Dampers).

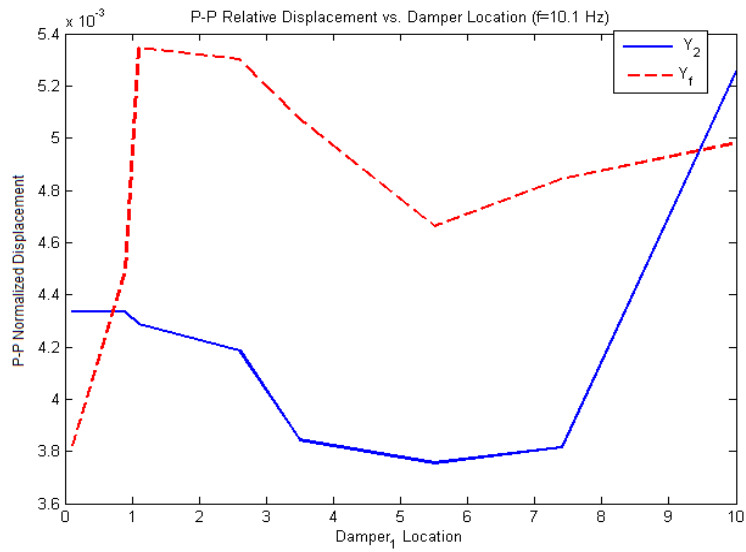


Figure 5.27: Conductor peak-to-peak displacement vs. damper location for $f = 9.53$ Hz (2 Dampers).

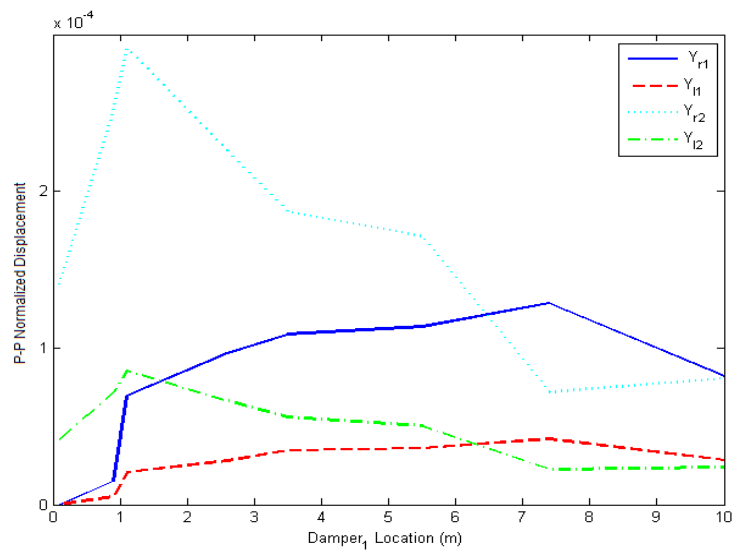


Figure 5.28: Damper peak-to-peak displacement vs. damper location for $f = 9.53$ Hz (2 Dampers).

Chapter 6

Conclusion and Recommendation

6.1 Summary

This thesis is motivated by the past failures of the transmission lines due to *Aeolian vibration*. The elimination of these failures is part of the challenges line engineers encounter in controlling *Aeolian vibration*. Currently, the best method to control wind induced vibration is to attach Stockbridge dampers to the conductor. However, the effectiveness of the damper depends on both the damping properties and its location on the conductor. As such, this thesis dealt with the *Aeolian vibration* of a single conductor with dampers, specifically, the effect of the damper location and the damping properties.

Aeolian vibration of a single conductor has been studied using the energy balance method, which states that the energy imparted by wind on the conductor is dissipated by the conductor self-damping and the damper. This method provides a good approximation of the maximum amplitude of vibration. However, it does not account for the two-way coupling between the conductor and the damper, the flexural rigidity of the conductor and damper, and the mass per unit length of the messenger. The proposed model takes these into consideration.

The mathematical model was presented in chapter 3 where the potential and kinetic energy equations of the system were derived. These equations were then discretized using the finite element method to determine the equations of motion. In

the process of the formulation the following assumptions were made:

1. The conductor behaves as an Euler-Bernoulli beam with an axial force.
2. The displacement of the conductor is very small (less than the conductor diameter).
3. The tension, flexural rigidity, and mass per unit length are constant.
4. The system is linear.
5. Torsion in the conductor is negligible.
6. The messenger is modeled as an Euler-Bernoulli beam.
7. The damper counterweights are represented as lumped masses.

These assumptions were justified in the mathematical formulation chapter. The overall formulation for the conductor with and without a damper was validated using the commercial finite element software ANSYS and the results in Ref. [10], respectively. Overall, both models were found to be valid with approximately 1% error.

Once the mathematical formulation was validated, the response of the conductor was predicted and the effect of the damper on the conductor was studied. In the first part of the numerical analysis, the natural frequencies of two conductors, 240/40 sq. mm and 1840 kcmil, without damper were examined for different span lengths and tensions. Also, the effect of the forcing frequency, tension, and span length on the conductor response were studied. The important observations are:

1. The conductor flexural rigidity and mass per unit length can significantly alter the mode shapes. The natural frequency of the conductor increases with its flexural rigidity and decreases with its mass per unit length.
2. The natural frequency increases with tension and decreases as the span length increases. Consequently, higher span lengths can be excited with very low Strouhal frequency.

3. The maximum amplitude of a conductor without damper decreases monotonically as the span length decreases. Hence, longer spans are more susceptible to vibration.
4. The conductor becomes stiffer with increasing tension; as a result, the maximum amplitude decreases. But, this does not mean the conductor is safer from fatigue damage. Note that higher tension results in lower safe bending amplitude. So, by increasing the tension, the conductor bending amplitude can be much greater than the safe bending amplitude. Consequently, the conductor would be more vulnerable to fatigue failure.
5. The maximum relative vibration amplitude of a conductor with higher flexural rigidity is less than that with a lower flexural rigidity.
6. The location of the maximum displacement varies with the excitation frequency. When the conductor is excited with the first mode, the maximum displacement occurs in the mid-span. However, with respect to the second mode of excitation, the midpoint results in a minimal displacement. Also, symmetrical displacement about the mid-span is observed for the conductor without a damper. Hence, multiple maximum amplitudes of vibration can be obtained in this case.
7. With respect to the line conditions established in chapter 5, the bending amplitude of a conductor without a damper is less than the safe bending amplitude. Thus, a conductor without a damper would not be safer from fatigue failure.

The second part of the simulation dealt with the response of the combination of the conductor with dampers. The effect of the damper mass, the forcing frequency, and the location of the damper were examined. The following observations were made:

1. Attaching a damper to the conductor, reduces the natural frequency. This reduction is insignificant when only one damper is used. However, the addition of another damper, considerably diminishes the higher natural frequencies.

2. Facing the larger counterweight mass toward the suspension clamp and the smaller mass toward the mid-span slightly reduces the amplitude of vibration.
3. A damper with two unbalanced counterweight masses resulted in smaller vibration amplitude. This is in agreement with the observation in the literature that asymmetric dampers are more efficient than the symmetric dampers.
4. The maximum vibration displacement of a conductor with dampers decreases with increasing vibration frequency. Whereas, the amplitude of the damper increases as the system is excited with higher frequency. Irrefutably, the damper is most efficient at higher vibration frequencies.
5. The presence of a damper does not necessarily reduce the vibration amplitude. When a damper is placed at a vibration node, it would be ineffective. As the damper is moved away from the vibration node, its efficiency increases.
6. The optimum damper positioning depends on the forcing frequency. This range tends to increase or decrease with increasing forcing frequency.
7. For lower vibration frequencies, the optimum range is approximately 70 to 95% of the loop length corresponding to the subject forcing frequency. Higher vibration frequencies can pertain to a percentage of loop length much higher than 100%. The vibration amplitude of the conductor notably reduces whereas the amplitude of the damper increases as the system is excited with higher frequency. Irrefutably, the damper is most efficient at higher vibration frequencies.
8. The maximum vibration amplitude of the conductor reduces as the damper is positioned within the optimum range, whereas the displacement of the damper increases. Hence, dampers are also very efficient within their optimum location range.
9. Attaching two dampers within their optimum damper location range reduces the amplitude of vibration by approximately ten times.

The presence of a damper on the conductor can be advantageous or disadvantageous. When the combination of the mass and the location of the damper are astutely chosen, the vibration amplitude would significantly reduce and the conductor vibration would stabilize. This would reduce the chance of the conductor from fatigue failure since the conductor bending amplitude would be much lower than the safe bending amplitude. On the other hand, when the location of the damper or the properties of the damper are not carefully chosen, the conductor may be more susceptible to fatigue failure.

6.1.1 Conclusion

The following conclusions are inferred:

- It is important to include the flexural rigidity of the conductor, as well as the mass and flexural rigidity of the damper in the mathematical formulation. Note that these properties can significantly affect the maximum amplitude of vibration.
- The mass of the counterweight should be carefully determined so that the damper is capable of dissipating the most energy imparted by the wind to the conductor.
- Placing two dampers symmetrically at each end is better than attaching only one damper.
- Always face the counterweight with the larger mass toward the insulator clamp and the lower counterweight mass toward the mid-span.
- With respect to the optimum location of the damper, the rule of thumb mentioned from the literature review should not be used as it is not effective because it only pertains to a specific frequency. Instead, all the dominant vibration frequencies should be considered in order to examine the optimum location range.
- The best optimum range to be predicted should correspond to the dominant frequency that resulted in the highest vibration amplitude.

6.2 Proposed Future Work

Further research in the subject topic could be listed as follows:

- Investigate the mechanical behaviour of the messenger.
- Conduct an experiment to validate the model of a single conductor with a damper.
- Examine the variation of the flexural rigidity and the tension for longer span length.
- Extend the developed model by including the non-linear terms, conductor self-damping, and torsion.
- Examine the coupling between the insulator and the conductor.
- Develop a Finite Element model for bundle conductor by modeling the conductor and the spacer dampers as one system.

Appendix A

Appendix

A.1 ANSYS Vibration Modes

As discussed in section 5.1.1.1, the remaining vibration modes of interest of the single conductor with a Stockbridge damper are shown in the figures below:

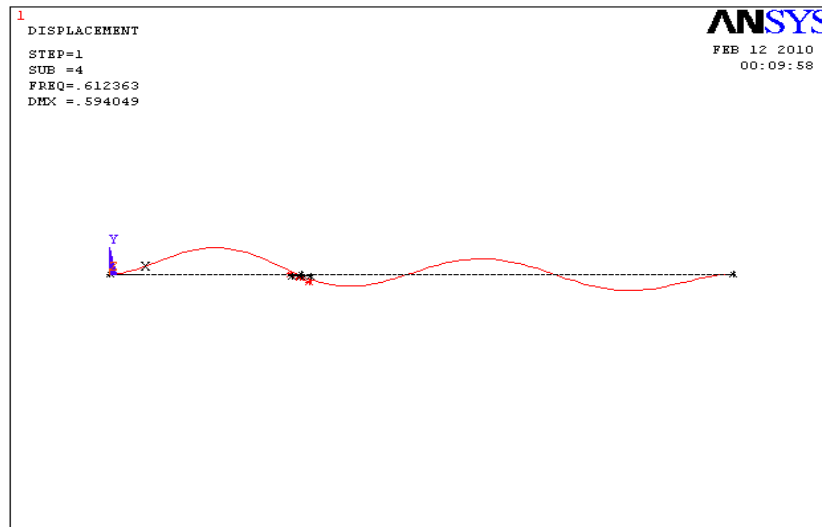


Figure A.1: Fourth mode of vibration of the conductor plus a damper.

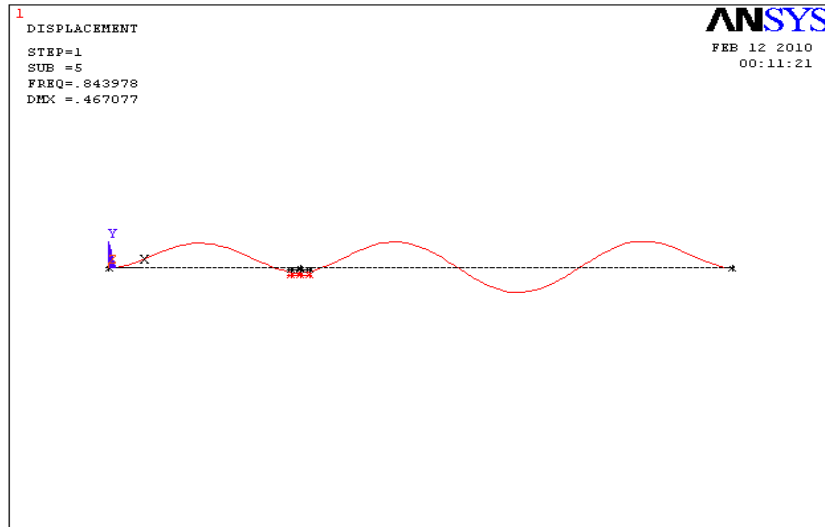


Figure A.2: Fifth mode of vibration of the conductor plus a damper.

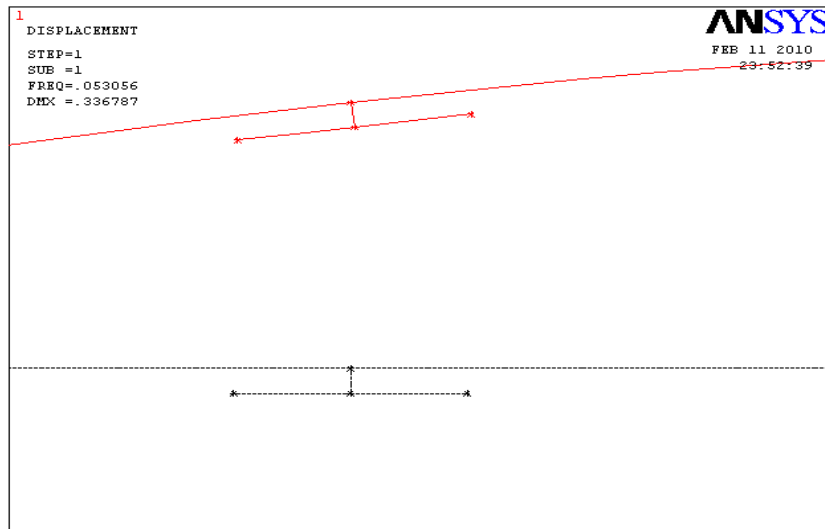


Figure A.3: First mode of vibration with a closer look at the damper.

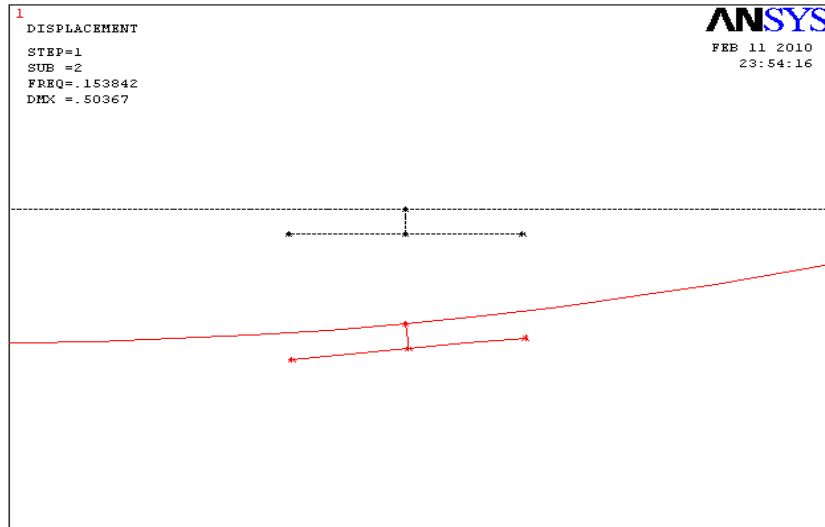


Figure A.4: Second mode of vibration with a closer look at the damper.

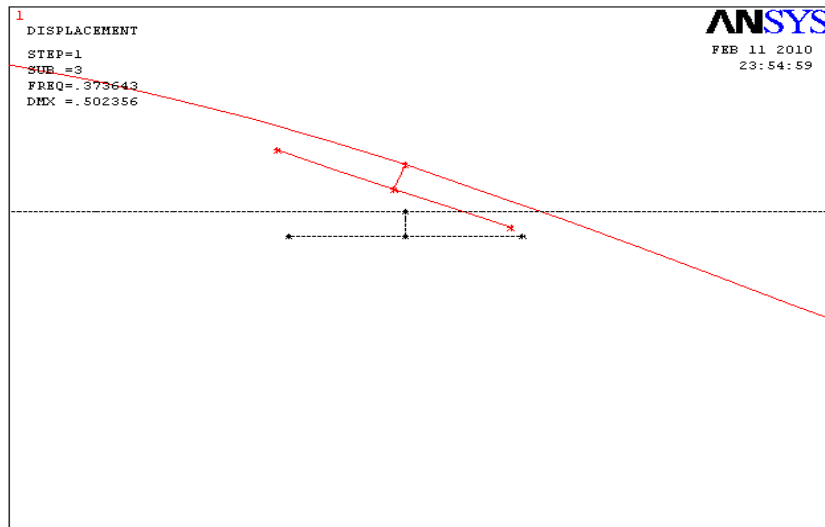


Figure A.5: Third mode of vibration with a closer look at the damper.

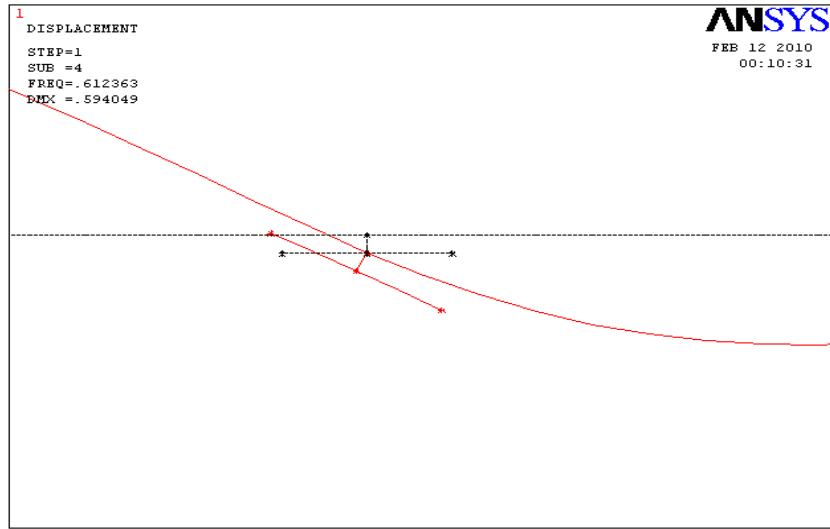


Figure A.6: Fourth mode of vibration with a closer look at the damper.

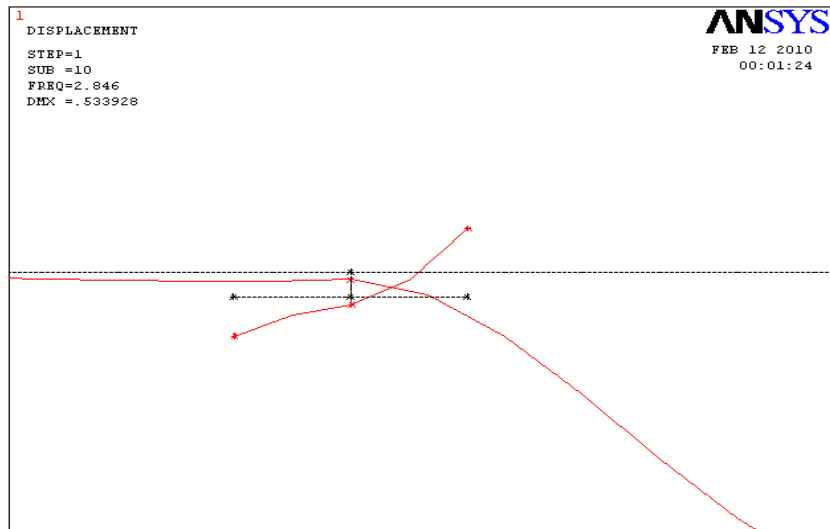


Figure A.7: Tenth mode of vibration with a closer look at the damper.

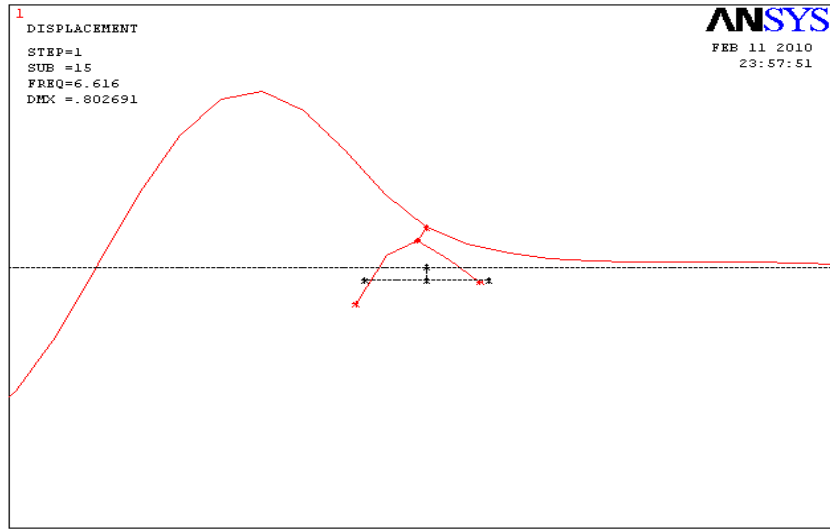


Figure A.8: Fifteenth mode of vibration with a closer look at the damper.

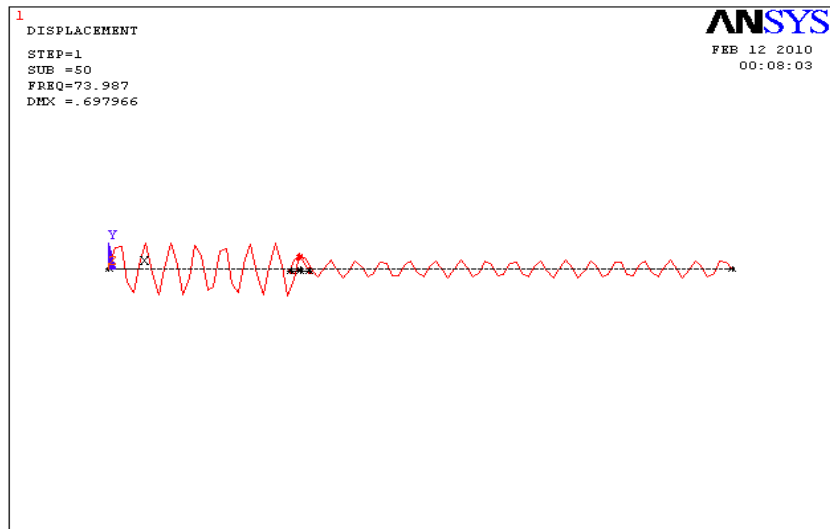


Figure A.9: Fifth mode of vibration of the conductor plus a damper.

Appendix B

Appendix

B.1 MATLAB Codes

The following MATLAB codes were used to determine the natural frequencies and the response of a single conductor with a Stockbridge damper under Aeolian vibration.

```
1  %-----
2  % Input
3  %-----
4  g=0;% Gravity
5  D=0.0219; % conductor diameter in meters
6
7  P=0.18522; %wind Force for v=7m/s in N/m
8
9  EIc=16; %fluxural rigidity of the conductor in N/m^2;
10 rhoAc=.987; % kg/m; %mass per unit length of the conductor;
11 Lc=372; %span: Total length of the conductor
12
13 T=17280;% tension
14
15 edofc=4; % dof of an element of the conductor
16 edofd=10; % dof of an element of the damper
17 nel=50; % nber of element of the conductor
18 dofnc=2; % dof per none (can use it for both messenger & conductor
19 % because the same element was used)
20 neld1=1; % number of element for damper1
21 neld1=neld1;
22 neldr=neld1;
23 neld2=neld1; % number of element for damper2
24
25
26 nnodesysd=2*neld1+1; % nber of nodes in the messenger
27 nnodesys=(nel+1+2*(2*neld1+1));%number of node in the global
28 %system since neld1=neld2
```

```

29 gdof=dofn*nnodesys; %total dof of the whole syst %
30           % (i.e conductor and damper combined)
31 gdofd=dofn*nnodesysd; %Total dof of the messenger only
32 dofsystc=2*(nel+1); % global dof of the conductor only
33
34
35 msys=zeros (gdof);
36 ksys=zeros (gdof);
37 fsys= zeros (gdof,1);
38 fgsys=zeros (gdof,1);
39
40
41 rhoAr=0.498; %mass per unit length of the messenger on the right
42 rhoAl=rhoAr; %mass per unit length of the messenger on the left
43 h=0.05;      %Height of the damper
44
45 lc=Lc/nel; %length of each element
46 Lr=0.15;   %0.15,0.15,0.15 length of the messenger from the bottom
47           %of clamp to the weight on the right
48 Ll=0.2;%0.2,0.15,0.175,. %length of the messenger from
49           %the bottom of clamp to the weight on the left
50
51 lr=Lr/neldr; % element length of the messenger on
52           % the right and it's only valid when neld1 is even
53 ll=Ll/neldl; % similarly on te left
54
55 Ir=0.001814;% Inertia of the right-side damper in Nm^2
56 Il=0.00741;% Inertia of the left-side damper in Nm^2
57 EI1=3.19; %fluxural rigidity of the messenger in the left
58 EIr=EI1;%fluxural rigidity of the messenger in the right
59
60 mdr=0.856;%mass of the damper on the right in Kg
61 mdl=1.5;% mass of the damper on the left
62 mmr=rhoAr*Lr; % mass of the messenger on the left
63 mml=rhoAl*Ll; %massof the messenger on the right
64
65 bcdof=zeros (8,1);
66 bcdof(1)=1; % applying bc at node1 ( i,e wcl=0)
67 bcdof(2)=2;
68 bcdof(4)=2*(nel+1);
69 bcdof(3)=2*nel+1;%applying bc at the last node of the
70           %conductor(i,e wcn=0)
71 bcdof(5)=2*(nel+1)+2*neldl+1; % applying bc at the node of the
72           %damper which is clamped ( i,e wd=0)
73 bcdof(6)=2*(nel+neldl+2);% i.e (wd'=0)
74 bcdof(7)=gdof-2;% boundary condition on the rotation of mid node
75           % of damper2
76 bcdof(8)=gdof-3;%boundary condition on the displacement
77           %of mid node of damper2
78
79 Ld1=10;% 5.5,10,10;15;
80 Ld2=360;%366.5, 366.5,360; 366% damper location
81
82 %-----
83 % This function determine the location of the damper in the element
84 function ld2=findld2(Ld2,lc,nel)

```

```

85
86 for n=1:nel
87
88     if (Ld2/lc>n && Ld2/lc<=(n+1)) %get element matrice with
89         %damper
90
91         ld2=Ld2-n*lc; %ld is the location of damper in element
92
93     end
94 end
95
96 %-----
97
98 %Find location of the damper1 and damper2 in the element
99
100 if (Ld1/lc<1)
101     ld1=Ld1;
102 elseif (Ld2/lc>1)
103     ld2=findld2(Ld2,lc,nel);%Call the subroutine findld2 to
104         %determine the location
105         %of the damper in the element
106 end
107
108 %-----
109 % Matrix KM is the subroutine that ccomputes the mass and stiffness
110 % matrices
111
112 function [K,M,Kd,Md1,Md2 F,Fg1 Fg2]=matrixKM(Ir,Il,h,rhoAr,rhoAl,...
113     lc,ld1,ld2,lr,ll,EIc,T,rhoAc,EIl,EIr,mdr,mdl,mmr,mml,P,g)
114
115 %Note that the subcrip 1 and 2 denote the damper on the left and
116 %right of the mid-span.
117 syms xc xr xl
118 % shapes function defined from 0 to 1 ( Cubic polynomial)
119
120 Nc=[1-3*(xc/lc)^2+2*(xc/lc)^3;xc-2*lc*(xc/lc)^2+lc*(xc/lc)^3;...
121     3*(xc/lc)^2-2*(xc/lc)^3;-lc*(xc/lc)^2+lc*(xc/lc)^3];
122 Nr=[1-3*(xr/lr)^2+2*(xr/lr)^3;xr-2*lr*(xr/lr)^2+lr*(xr/lr)^3;
123     3*(xr/lr)^2-2*(xr/lr)^3;-lr*(xr/lr)^2+lr*(xr/lr)^3];
124 Nl=[3*(xl/ll)^2-2*(xl/ll)^3;-11*(xl/ll)^2+11*(xl/ll)^3;...
125     1-3*(xl/ll)^2+2*(xl/ll)^3;xl-2*ll*(xl/ll)^2+11*(xl/ll)^3];
126
127 % First derivation of the shapes function
128 d1Nc=diff(Nc,xc);
129 d1Nr=diff(Nr,xr);
130 d1Nl=diff(Nl,xl);
131
132 % Second derivation of the shapes function
133 d2Nc=diff(d1Nc,xc);
134 d2Nr=diff(d1Nr,xr);
135 d2Nl=diff(d1Nl,xl);
136
137 % Shape function evaluated at damper mass
138
139 Nri=subs(Nr,xr,lr); % Right-side damper mass
140 d1Nri=subs(d1Nr,xr,lr);

```

```

141 Nli=subs(Nl,xl,ll);%Left-side damper mass
142 d1Nli=subs(d1Nl,xl,ll);
143
144 % M is the Mass matrice of the conductor w/o damper
145
146 Mc= rhoAc*int (Nc*transpose (Nc),xc,0,lc);
147 M=Mc;
148
149 % Mass matrice of the conductor with damper
150
151 Nci1=subs (Nc,xc,ld1);
152 Nci2=subs (Nc,xc,ld2);
153 d1Nci1=subs (d1Nc,xc,ld1);
154 d1Nci2=subs (d1Nc,xc,ld2);
155
156 % Mass matrice (top left 4x4) of the conductor element with damper
157 % Damper1
158 Mcc1=Mc+mdr*(Nci1*transpose (Nci1)+lr*(Nci1*transpose (d1Nci1) ...
159 +d1Nci1*transpose (Nci1))+d1Nci1*transpose (d1Nci1)*(h^2+lr^2))...
160 +Ir*d1Nci1*transpose (d1Nci1)+mdl*(Nci1*transpose (Nci1) ...
161 -ll*(Nci1*transpose (d1Nci1)+d1Nci1*transpose (Nci1))...
162 +d1Nci1*transpose (d1Nci1)*(h^2+ll^2))+Il*d1Nci1*transpose (d1Nci1) ...
163 +mmr*(Nci1*transpose (Nci1)+d1Nci1*transpose (d1Nci1)*h^2) ...
164 +1/2*rhoAr*(lr^2*(Nci1*transpose (d1Nci1)+d1Nci1*transpose (Nci1))...
165 +2/3*lr^3*d1Nci1*transpose (d1Nci1))+mml*(Nci1*transpose (Nci1) ...
166 +d1Nci1*transpose (d1Nci1)*h^2)+1/2*rhoAl*(-ll^2*(Nci1...
167 *transpose (d1Nci1)+d1Nci1*transpose (Nci1))+2/3*ll^3*d1Nci1...
168 *transpose (d1Nci1));
169 %Damper2
170 Mcc2=Mc+mdr*(Nci2*transpose (Nci2)+lr*(Nci2*transpose (d1Nci2) ...
171 +d1Nci2*transpose (Nci2))+d1Nci2*transpose (d1Nci2)*(h^2+lr^2))...
172 +Ir*d1Nci2*transpose (d1Nci2)+mdl*(Nci2*transpose (Nci2) ...
173 -ll*(Nci2*transpose (d1Nci2)+d1Nci2*transpose (Nci2))...
174 +d1Nci2*transpose (d1Nci2)*(h^2+ll^2))+Il*d1Nci2*transpose (d1Nci2) ...
175 +mmr*(Nci2*transpose (Nci2)+d1Nci2*transpose (d1Nci2)*h^2) ...
176 +1/2*rhoAr*(lr^2*(Nci2*transpose (d1Nci2)+d1Nci2*transpose (Nci2))...
177 +2/3*lr^3*d1Nci2*transpose (d1Nci2))+mml*(Nci2*transpose (Nci2) ...
178 +d1Nci2*transpose (d1Nci2)*h^2)+1/2*rhoAl*(-ll^2*(Nci2...
179 *transpose (d1Nci2)+d1Nci2*transpose (Nci2))+2/3*ll^3*d1Nci2...
180 *transpose (d1Nci2));
181
182 % Mass of the coupling between damper on the right and the conductor
183
184 eMrc1=rhoAr*int ((Nr*transpose (Nci1)+xr*Nr*transpose (d1Nci1)),xr,0,lr);
185
186 eMrc2=rhoAr*int ((Nr*transpose (Nci2)+xr*Nr*transpose (d1Nci2)),xr,0,lr);
187
188 Mrc1=eMrc1+mdr*(Nri*transpose (Nci1)+lr*Nri*transpose (d1Nci1))...
189 +Ir*d1Nri*transpose (d1Nci1);
190
191 Mrc2=eMrc2+mdr*(Nri*transpose (Nci2)+lr*Nri*transpose (d1Nci2))...
192 +Ir*d1Nri*transpose (d1Nci2);
193
194 %Mass of the coupling between damper on the left and the conductor
195
196 eMlc1=rhoAl*int ((Nl*transpose (Nci1)-xl*Nl*transpose (d1Nci1)),xl,0,ll);

```

```

197 eMlc2=rhoAl*int((Nl*transpose(Nci2)-xl*Nl*transpose(d1Nci2)),xl,0,ll);
198
199 Mlc1=mdl*(Nli*transpose(Nci1)+ll*Nli*transpose(d1Nci1))...
200     +I1*d1Nli*transpose(d1Nci1)+eMlc1;
201
202 Mlc2=mdl*(Nli*transpose(Nci2)+ll*Nli*transpose(d1Nci2))...
203     +I1*d1Nli*transpose(d1Nci2)+eMlc2;
204
205 Mcl1=transpose(Mlc1);
206 Mcr1=transpose(Mrc1);
207
208 Mcl2=transpose(Mlc2);
209 Mcr2=transpose(Mrc2);
210
211 %Mass of the damper on the left
212 eMll=rhoAl*int((Nl*transpose(Nl)),xl,0,ll);
213 Mll=mdl*Nli*transpose(Nli)+I1*d1Nli*transpose(d1Nli)+eMll;
214
215 %Mass of the damper on the right
216 eMrr=rhoAr*int((Nr*transpose(Nr)),xr,0,lr);
217 Mrr= mdr*Nri*transpose(Nli)+Ir*d1Nri*transpose(d1Nri)+ eMrr;
218 Mlr=zeros(4);
219 Mrl=transpose(Mlr);
220
221 % Element mass matrice with damper
222 % Mass element from ld(1)Note that this is 12x12 matrice
223 m1=[Mcc1 Mcr1 Mcl1;Mrc1 Mrr Mrl;Mlc1 Mlr Mll];
224 m2=[Mcc2 Mcr2 Mcl2;Mrc2 Mrr Mrl;Mlc2 Mlr Mll];
225
226 % Reducing this 12x12 matrice to 10x10 leads to Md
227 % conductor element with damper1
228 Md1=[m1(1:6,1:6) m1(1:6,7)+m1(1:6,9) m1(1:6,8)+m1(1:6,10)...
229     m1(1:6,11:12);m1(7,1:6)+m1(9,1:6) m1(7,7)+m1(7,9)+m1(9,7)...
230     +m1(9,9) m1(7,8)+m1(7,10)+m1(9,8)+m1(9,10) m1(7,11:12)...
231     +m1(9,11:12);m1(8,1:6)+m1(10,1:6) m1(8,7)+m1(8,9)+m1(10,7)...
232     +m1(10,9) m1(8,8)+m1(8,10)+m1(10,8)+m1(10,10) m1(8,11:12)...
233     +m1(10,11:12);m1(11:12,1:6) m1(11:12,7)+m1(11:12,9)...
234     m1(11:12,8)+m1(11:12,10) m1(11:12,11:12)];
235 %conductor element with damper1
236 Md2=[m2(1:6,1:6) m2(1:6,7)+m2(1:6,9) m2(1:6,8)+m2(1:6,10)...
237     m2(1:6,11:12);m2(7,1:6)+m2(9,1:6) m2(7,7)+m2(7,9)+m2(9,7)...
238     +m2(9,9) m2(7,8)+m2(7,10)+m2(9,8)+m2(9,10) m2(7,11:12)...
239     +m2(9,11:12);m2(8,1:6)+m2(10,1:6) m2(8,7)+m2(8,9)+m2(10,7)...
240     +m2(10,9) m2(8,8)+m2(8,10)+m2(10,8)+m2(10,10) m2(8,11:12)...
241     +m2(10,11:12);m2(11:12,1:6) m2(11:12,7)+m2(11:12,9)...
242     m2(11:12,8)+m2(11:12,10) m2(11:12,11:12)];
243
244 % Element stiffness matrices
245
246 Kc=int(EIc*(d2Nc*transpose(d2Nc))+T*(d1Nc*transpose(d1Nc)),xc,0,lc);
247
248 K=Kc;
249
250 Krr=int(EIr*(d2Nr*transpose(d2Nr)),xr,0,lr);
251
252 Kll=int(EI1*(d2N1*transpose(d2N1)),xl,0,ll);

```

```

253
254 Krc=zeros(4);Kcr=zeros(4);Klr=zeros(4);
255 Klc=zeros(4);Kcl=zeros(4);Krl=zeros(4);
256
257 % stiffness matrce of the element with damper is K
258
259 k=[Kc Kcr Kcl; Krc Krr Krl; Klc Klr Kll];
260
261 %The 10x10 stiffness matrce is Kd
262
263 Kd= [k(1:6,1:6) k(1:6,7)+k(1:6,9) k(1:6,8)+k(1:6,10) k(1:6,11:12);...
264      k(7,1:6)+k(9,1:6) k(7,7)+k(7,9)+k(9,7)+k(9,9) k(7,8)+k(7,10) ...
265      +k(9,8)+k(9,10) k(7,11:12)+k(9,11:12);k(8,1:6)+k(10,1:6) ...
266      k(8,7)+k(8,9)+k(10,7)+k(10,9) k(8,8)+k(8,10)+k(10,8)+k(10,10) ...
267      k(8,11:12)+k(10,11:12);k(11:12,1:6) k(11:12,7)+k(11:12,9) ...
268      k(11:12,8)+k(11:12,10) k(11:12,11:12)];
269
270 % The non conservative force F (wind force)
271
272 F=P*int(Nc,xc,0,lc);
273
274 % The conservative force obtained from the potential energy
275
276 G1=g*[mdr*(Nci1-lr*d1Nci1)+mdl*(Nci1+ll*d1Nci1);mdr*Nri;mdl*Nli];
277 %is 12x1
278 G2=g*[mdr*(Nci2-lr*d1Nci2)+mdl*(Nci2+ll*d1Nci2);mdr*Nri;mdl*Nli];
279 %is 12x1
280
281 % Reduce the above into a 10x10
282
283 Fg1=[G1(1:6,1);G1(7,1)+G1(9,1);G1(8,1)+G1(10,1);G1(11:12,1)];
284
285 Fg2=[G2(1:6,1);G2(7,1)+G2(9,1);G2(8,1)+G2(10,1);G2(11:12,1)];
286
287 return
288
289
290 %-----
291
292 % Assemble KM subroutine assembles the element mass and stiffness
293 % matrices. This program assembles the mass and stiffness matrices.
294 % First This subroutine looks for the element that contains the
295 % damper. Once this element is found, the element mass and stiffness
296 % corresponding to the element with the damper is called and the
297 % assembly is done in four groups. The first group, the 4x4 matrix on
298 % the top left corner of the 10x10, is assembled. Next, this
299 % subroutine assembles the second group, which is the 4x6 on the top
300 % right corner. Then, the inverse of the 4x6, which is the 6x4 at
301 % the bottom left, is called for assemblage and finally the 6x6 on
302 % the left is assembled. The AssemleKM.m calls the element without
303 % the damper at every other time.
304
305 %-----
306 function [ksys,msys,fsys,fgsys]=fassforsim(fsys,fgsys,ksys,msys,F,...
307      Fg1,Fg2,M,Md1,Md2,K,Kd,Ld1,Ld2,n,lc,edofc,edofd,neld1,...
308      sdof1,sdof2,neld2)

```

```

309
310 % Intialize count (ct1, ct2...)
311 ct1=0;
312 ct2=0;
313 ct3=0;
314 ct4=0;
315
316 %Starting program for damper1
317
318 if (Ld1/lc>(n-1) && Ld1/lc<n) % get element matrice with damper
319
320 % Get the top-right 4x4 matrix
321 for k1=1:edofc
322     for j1=1:edofc
323
324         msys (sdof1+k1-1, sdof1+j1-1)=msys (sdof1+k1-1, ...
325             sdof1+j1-1)+Md1 (k1, j1);
326         ksys (sdof1+k1-1, sdof1+j1-1)=ksys (sdof1+k1-1, ...
327             sdof1+j1-1)+Kd (k1, j1);
328     end
329
330 % Wind force on the damper element
331 fsys (sdof1+k1-1, 1)=fsys (sdof1+k1-1, 1)+F (k1, 1);
332
333 % Force due to gravity
334 fgsys (sdof1+k1-1, 1)=fgsys (sdof1+k1-1, 1)+Fg1 (k1, 1);
335 end
336
337 for m1=1:neld1
338     sdof3=4*m1-3;
339     for k=1:edofd
340         ct2=ct2+1;
341         for j=1:edofd
342             ct1=ct1+1;
343
344             % Assemble top-left 6x4 matrix
345
346             if (ct1>4&&ct2<=4)
347                 msys (sdof1+k-1, sdof1+sdof2+sdof3+j-2)=msys...
348                     (sdof1+k-1, sdof1+sdof2+sdof3+j-2) ...
349                     +Md1 (k, j);
350                 ksys (sdof1+k-1, sdof1+sdof2+sdof3+j-2)=ksys...
351                     (sdof1+k-1, sdof1+sdof2+sdof3+j-2) ...
352                     +Kd (k, j);
353                 % Assemble bottom-left 4x6 matrix
354             elseif (ct1<=4 && ct2>4)
355                 msys (sdof1+sdof2+sdof3+k-2, sdof1+j-1)=msys...
356                     (sdof1+sdof2+sdof3+k-2, sdof1+j-1)+Md1 (k, j);
357                 ksys (sdof1+sdof2+sdof3+k-2, sdof1+j-1)=ksys...
358                     (sdof1+sdof2+sdof3+k-2, sdof1+j-1)+Kd (k, j);
359                 % Assemble bottom-left 6x6 matrix
360             elseif (ct1>4 && ct2>4) % all greater
361
362                 msys (sdof1+sdof2+sdof3-2+k, sdof1+sdof2+sdof3...
363                     -2+j)=msys (sdof1+sdof2+sdof3-2+k, sdof1+sdof2...
364                     +sdof3-2+j)+Md1 (k, j);

```

```

365
366             ksys (sdof1+sdof2+sdof3-2+k, sdof1+sdof2+sdof3...
367             -2+j)=ksys (sdof1+sdof2+sdof3-2+k, sdof1+sdof2...
368             +sdof3-2+j)+Kd (k, j);
369
370         end
371     end
372
373     fgsys (sdof1+sdof2+sdof3-2+k, 1)=fgsys (sdof1+sdof2+...
374     sdof3-2+k, 1)+Fg1 (k, 1);
375     %Force of damper1 due to gravity
376     ct1=0;
377
378     end
379     ct2=0;
380 end
381 % Repeat the same procedure descibed for damper1
382
383 % starting program for damper 2
384
385 elseif (Ld2/lc>n && Ld2/lc<(n+1)) % get 2nd element with damper
386
387     for k11=1:edofc
388         for j11=1:edofc
389
390             msys (sdof1+k11-1, sdof1+j11-1)=msys (sdof1+k11-1, ...
391             sdof1+j11-1)+Md2 (k11, j11);
392
393             ksys (sdof1+k11-1, sdof1+j11-1)=ksys (sdof1+k11-1, ...
394             sdof1+j11-1)+Kd (k11, j11);
395
396         end
397     end
398
399     for m2=1:neld2
400         sdof4=4*m2-3; sdof5=2*(2*neld2+1);
401         for k2=1:edofd
402             ct4=ct4+1;
403             for j2=1:edofd
404                 ct3=ct3+1;
405
406                 if (ct3>4&&ct4≤4)
407                     msys (sdof1+k2-1, sdof1+sdof5+sdof4+sdof2+j2...
408                     -2)=msys (sdof1+k2-1, sdof1+sdof5+sdof4...
409                     +sdof2+j2-2)+Md2 (k2, j2); ksys (sdof1+k2-1, ...
410                     sdof1+sdof5+sdof4+sdof2+j2-2)=ksys (sdof1...
411                     +k2-1, sdof1+sdof5+sdof4+sdof2+j2-2) ...
412                     +Kd (k2, j2);
413
414                 elseif (ct3≤4 && ct4>4)
415                     msys (sdof1+sdof2+sdof5+sdof4+k2-2, sdof1+j2...
416                     -1)=msys (sdof1+sdof2+sdof5+sdof4+k2-2, ...
417                     sdof1+j2-1)+Md2 (k2, j2);
418
419                     ksys (sdof1+sdof2+sdof5+sdof4+k2-2, sdof1+j2...
420                     -1)=ksys (sdof1+sdof2+sdof5+sdof4+k2-2, ...

```

```

421         sdof1+j2-1)+Kd(k2, j2);
422
423         elseif (ct3>4 && ct4>4)
424
425             msys(sdof1+sdof2+sdof5+sdof4-2+k2, sdof1+...
426                 sdof5+sdof2+sdof4-2+j2)= msys(sdof1+sdof2+...
427                 sdof5+sdof4-2+k2, sdof1+sdof5+sdof2+sdof4...
428                 -2+j2)+Md2(k2, j2);
429
430
431             ksys(sdof1+sdof2+sdof5+sdof4-2+k2, sdof1...
432                 +sdof5+sdof2+sdof4-2+j2)=ksys(sdof1+sdof2+...
433                 sdof5+sdof4-2+k2, sdof1+sdof5+sdof2+sdof4...
434                 -2+j2)+Kd(k2, j2);
435
436         end
437     end
438     % Force from damper2 due to gravity
439     fgsys(sdof1+sdof2+sdof5+sdof4-2+k2, 1)=fgsys(sdof1+...
440         sdof2+sdof5+sdof4-2+k2, 1)+Fg2(k2, 1);
441     ct3=0;
442 end
443 ct4=0;
444 end
445
446
447
448 % Assemble all the elements without dampers
449
450 else % get element matrice w/o damper
451     for k=1:edofc
452         for j=1:edofc
453             msys(sdof1+k-1, sdof1+j-1)=msys(sdof1+k-1, sdof1+j...
454                 -1)+M(k, j);
455             ksys(sdof1+k-1, sdof1+j-1)=ksys(sdof1+k-1, sdof1+j...
456                 -1)+K(k, j);
457
458         end
459         fsys(sdof1+k-1, 1)=fsys(sdof1+k-1, 1)+F(k, 1);
460     end
461 end
462
463 end
464
465 %-----
466 % Apply BC subroutine is used for applying boundary condition
467
468 function [ksys,msys,fsys,fgsys]=feaplycsf(ksys,msys,fsys,fgsys,bcdof)
469
470 %-----
471 % Purpose:
472 %     Apply constraints to eigenvalue matrix equation
473 %     [kk]{x}=lamda[mm]{x}
474 %
475 % Synopsis:
476 %     [kk,mm]=feaplycs(kk,mm,bcdof)

```

```

477 %
478 % Variable Description:
479 %     kk – system stiffness matrix before applying constraints
480 %     mm – system mass matrix before applying constraints
481 %     bcdof – a vector containing constrained d.o.f
482 %-----
483
484 n=length(bcdof);
485 dofsys=size(ksys);
486 fprintf(1,'Print length of bcdof %d\n',n);%
487 for i=1:n
488     c=bcdof(i);
489     for j=1:dofsys
490         ksys(c,j)=0;
491         ksys(j,c)=0;
492         msys(c,j)=0;
493         msys(j,c)=0;
494     end
495     fsys(c,1)=0;
496     fgsys(c,1)=0;
497     ksys(c,c)=1;
498     msys(c,c)=1;
499 end
500
501
502 %-----
503 % Free Vibration analysis
504 %-----
505 for n=1:nel           %loop for the total number of elements
506     sdof1=2*n-1; sdof2=(nel-n)*2; %adding sdof2 in the global
507     %matrice would skip all dofs after 2nd node of damper element
508     [K,M,Kd,Md1,Md2 F,Fg1 Fg2]=fematriKM( Ir,I1,h,rhoAr,...
509     rhoAl,lc,ld1,ld2,lr,ll,EIc,T,rhoAc,EI1,EI2,mdr,mdl,...
510     mmr, mml,P,g);
511
512     [ksys,msys,fsys,fgsys]=AssembleKM(fsys,fgsys,ksys,msys,F,...
513     Fg1,Fg2,M,Md1,Md2,K,Kd,Ld1,Ld2,n,lc,edofc,edofd,neld1,...
514     sdof1,sdof2,neld2);
515 end
516
517 [ksys,msys]=applyBC(ksys,msys,bcdof); %apply the boundary conditions
518 fsol=eig(ksys,msys); % Solve for the natural frequency (^2)
519 fsol=sqrt(fsol); %Determine natural frequencies in rad/s
520 herz=fsol/2/pi; %Determine natural frequencies in Hz
521 [m,n]=size(fsol);
522 break
523
524 fprintf(1,'
525           natural frequencies\n');
526 fprintf(1,'mode           (Hz)
527           rad\n');
528 for i=3:m % ignore the 1st 2 natural frequencies
529     fprintf(1,'%2d           %6.4e
530           %6.4e \n',(i-2),herz(i),fsol(i));
531 end
532 return
533
534 %-----
535 % Force vibration analysis

```

```

533
534 %-----
535 % The Linearize subroutine converts second order ODE into the first
536 % This program converts the problem to a system of first order ODE
537 function Xdot=linearize(t,q)
538
539 global mu fg f gdof
540
541 w=2*pi*41.45; % 9.53 is the excitation frequency
542 % M*dotdot(q)+K*q=F+Fg; dotdot(q)+mu*q=f+fg;
543 % x1=q; x2=dotq; and dotx2=dot(dotq)
544 % Note that q is the displacement and dotq is the velocity and
545 % dot(dotq) is the acceleration. In this case q(1) is the
546 % displacement and q(2) is the velocity
547
548 X1dot=q(gdof+1:2*gdof,1); % the velocity q(2); q[q(1);q(2)]
549 X2dot=f*sin(w*t)+fg-mu*q(1:gdof,1);
550 Xdot=[X1dot;X2dot];
551 return
552
553 %-----
554 % MainSimulation determine the response
555 %-----
556
557 for n=1:nel %loop for the total number of elements
558     sdof1=2*n-1; sdof2=(nel-n)*2; %adding sdof2 in the global
559     %matrice would skip all dofs after 2nd node of damper element
560     [K,M,Kd,Md1,Md2 F,Fg1 Fg2]=fematriKM(Ir,Il,h,rhoAr,...
561     rhoAl,lc,ld1,ld2,lr,ll,EIc,T,rhoAc,EIl,EIr,mdr,mdl,...
562     mnr,mml,P,g);
563
564     [ksys,msys,fsys,fgsys]=AssembleKM(fsys,fgsys,ksys,msys,F,...
565     Fg1,Fg2,M,Md1,Md2,K,Kd,Ld1,Ld2,n,lc,edofc,edofd,neld1,...
566     sdof1,sdof2,neld2);
567 end
568
569 [ksys,msys]=applyBC(ksys,msys,bcdof); %apply the boundary conditions
570
571 % Divide all the terms in the eom by the mass matrix
572 mu=msys\ksys; % inv(msys)*ksys
573 f=msys\fsys*P; % x Lc because of the force per unit length P
574 fg=msys\fgsys;
575 %c=alpha*msys+beta*ksys; % Conductor selfDamping ratio
576 %from ref.[10] ( Dyanmical analysis of t.l
577 endtime=10; % Time for the simulation
578 tspan=[0 endtime];
579
580 % Intial Condition
581 q01=zeros(gdof,1); % initial displacement vector
582 q02=zeros(gdof,1); % initial velocity vector
583 q0=[q01;q02];
584 [t,q]=ode45('linearize',tspan,q0);
585
586
587 x=length(t); % number of iteration i.e number of ΔTs
588

```

```

589 q1=q(1:x,1:2*nel); % q1 is the displacement vector
590 % ( 2 dof vertical displacement and rotation)
591 y_max=max(max(abs(q1))); %find the maximum displacement of the
592 %conductor (this will always be the max
593 %vertical displ since the rotation is
594 %much smaller than this) maximum relative
595 %displacement of the conductor peak to peak
596 %max. amplitude
597 % find dof corresponding to maximum displ.
598 for tmax=1:x % i.e only q1 (displacement)
599     for nmax=1:2*nel
600         if (q1(tmax,nmax)==y_max || q1(tmax,nmax)==-y_max)
601             locate=nmax; % locate the dof corresponding to the
602 % maximum displacement
603         end
604     end
605 end
606 locate
607 yc_pp=2*y_max
608 xmid=2*max(abs((q1(1:x,nel+1))))
609 maxval_Ymdr1=2*max(abs((q(1:x,gdof-7))))
610 maxval_Ymdl1=2*max(abs((q(1:x,gdof-11))))
611 maxval_Ymdr2=2*max(abs((q(1:x,gdof-1))))
612 maxval_Ymdl2=2*max(abs((q(1:x,gdof-5))))
613 m_y2=2*max(abs((q1(1:x,3))))
614 m_yf=2*max(abs((q1(1:x,2*nel-1))))
615
616 % Initialize the relative displacement vectors
617
618 xmid=zeros(x,1); % Mid-span displacement
619 Ymax=zeros(x,1); % Maximum displacement
620 Y_2=zeros(x,1); % Displacement of the second node
621 Y_f=zeros(x,1); % Displacement of the penultimate node
622 Y_mdr=zeros(x,1); % Displacement of right-side damper
623 Y_mdl=zeros(x,1); % Displacement of left-side damper
624
625 for is=1:x % loop for all deta T
626
627     xmid(is)=1/D*q1(is,nel+1); % the displacement in the midspan
628 % (This is only correct provided nel
629 % is even)
630
631     Y_2(is)=1/D*q1(is,3); %relative displacement of the second
632 %node for all dT
633     Y_f(is)=1/D*q1(is,2*nel-1); %relative displacement of the
634 %penultimate node
635
636     Y_mdr1=1/D*q1(is,gdof-1); % relative displ. of
637 %the damper on the right
638     Y_mdl1=1/D*q1(is,gdof-5); % relative displacement of the left
639     Ymax(is)=1/D*q1(is,locate); %relative max displ for each ΔT
640
641 end
642 hold on
643
644 % Plot displacement vectors vs time

```

```
645 plot(t, xmid, '-')
646 hold on
647 plot(t, Ymax, '-')
648 hold on
649 plot(t, Y_2, '-')
650 hold on
651 plot(t, Y_f, '-')
652 hold on
653 plot(t, Y_mdr)
654 hold on
655 plot(t, Y_md1)
656 legend('Response of midpoint (for Ld=1.1) m_{dr}=0.856 & m_{dl}=1.5');
657 ylabel('Relative maximum displacement (Ymax/D)');
658 xlabel('time in second')
659 plot(t, q(:, 1)); plot(t, q(:, 2), ':')
660 legend('x1', 'x2'); ylabel('Amplitude'); xlabel('time')
```

Bibliography

- [1] EPRI. 2006. *Transmission Line Reference Book*, Wind Induced Conductor Motion, Palo Alto, California: Electrical Power Research institute.
- [2] Helix. 2008. Montreal, Quebec, Canada.
- [3] M.S. Dhotard, N. Ganesan and B.V.A. Rao. 1978. *Transmission Line Vibration*, Department of Applied Mechanics, India Institute of Technology, Journal of Sound and Vibration, 60(2), pp. 217-237.
- [4] R. Claren and G. Diana. 1969. *Mathematical Analysis of Transmission Line Vibration*, Institute of Electrical and Electronics Engineers, Transactions on Power Apparatus and Systems, 60(2), pp. 1741-1771.
- [5] Hydro One Inc. 2008. Toronto, Ontario.
- [6] D. Havard. 2008. *Assessment of the Cowal JCT x Longwood TS for Vibration Control*, Toronto, Ontario.
- [7] D. Havard. 2005. *Conductor Fatigue and Damper Damage on the Sarnia-Scott TS x Lucasville JCT*, Toronto, Ontario.
- [8] P. McCarthy and M. Melsness. 1996. *Severe Weather Elements Associated With September 5, 1996 Hydro Tower Failures Near Grosse Isle, Manitoba, Canada*, Manitoba Environment Service Center, Environment Canada, 48(6), pp. 21.
- [9] CIGRE Meeting. 2009. *Conductor Motion*, Toronto, Ontario.

- [10] N. Barbieri, O. Honorato de Souza and R. Barbieri. 2004. *Dynamical Analysis of Transmission Lines Cables*, Part1-Linear Theory, Mechanical System and Signal Processing, 18(3), pp. 659-669.
- [11] O. Nigol and H.J. Houston. 1985. *Aeolian Vibration of Single Conductor and Its Control*, IEEE Transactions on Power Apparatus and Systems, 104(11), pp. 3245-3254.
- [12] D. Feldman. 2000. *Aeolian Vibration: Possible Effects of Non Linear Behaviour of Stockbridge Dampers*, Electricité de France.
- [13] A. Leblond and C. Hardy. 2000. *Assessment of Safe Design Tension with Regard to Aeolian Vibrations Of Single Overhead Conductors*, IEEE Transaction Power Delivery 34C-TPC-14.
- [14] G.E. Braga, R. Nakamura, and T.A Furtado. 2004. *Aeolian Vibration of Overhead Transmission Line Cables: Endurance Limits*, IEEE Transmission and Distribution Conference: Latin America.
- [15] C. Hardy and A. Leblond. 1992. *Comparison Of Conductor Self-Damping Measurements*, CIGRE General Session, Paris.
- [16] G. Stockbridge. 1925. *Vibration Damper Patent No.1675391*, USA Patent Office.
- [17] W.B. Buchanan and G.B. Tebo. 1940. *Torsional Damper for Line Conductor Patent No. 2,215541*, USA patent office.
- [18] H. Wagner, V. Ramamurti, R. Sastry and K. Hartman. 1973. *Dynamic of Stockbridge Dampers*, Journal of Sound and vibration, 30(2), pp. 207-220.
- [19] M. Markiewicz. 1994. *Optimum Dynamic Characteristic of Stockbridge Dampers for Dead-End Spans*, Journal of Sound and Vibration, 188(2), pp. 243-256.
- [20] H.J. Krispin. 2007. *Optimization of the Efficiency of Aeolian Vibration Dampers*, IEEE Power Africa Conference and Exposition Johannesburg, South Africa.

- [21] J. Vecchiarelli. 1997. *Aeolian vibration of a conductor with a Stockbridge Type Damper*, Ph.D. Thesis, University of Toronto.
- [22] B. Shafer. 1984. *Dynamic Modeling of Wind Induced Vibration of Over Head Lines*, Int. Non Linear Mechanics, 19(5), pp. 455-467.
- [23] G. Diana, M. Falco, A. Cigada and A. Manenti. 2000. *On The Measurement of Over Head Transmission Lines Conductor Self-Damping*, IEEE Transactions on Power Apparatus and Systems, 15(1), pp. 285-292
- [24] R. Bishop and A. Hassan. 1964. *The Lift And Drag Forces On a Circular Cylinder Oscillating In a Flowing Fluid*, Proceedings of Royal Society, London, Series A, 277(3), pp. 51-75.
- [25] P.W. Bearman and I.G. Curie. 1979. *Pressure-Fluctuation Measurements On An Oscillating Circular Cylinder*, Journal of Fluid Mechanics, 91(4), pp. 661-677.
- [26] O. Griffin and G. Koopmann. 1977. *The vortex-excited lifts and reaction forces on resonantly vibrating cylinders*, Journal of Sound and Vibration, 54(3), pp. 435-448.
- [27] M. Kraus and P. Hagedorn. 1991. *Aeolian Vibration: Wind Energy Input Evaluated From Measurements on an Energized Transmission Lines*, IEEE transaction, 6(3), pp. 1264-1270.
- [28] H. Verma and P. Hagerdorn. 2005. *Wind Induced Vibration of Long Electrical Overhead Transmission Line Spans: A Modified Approach*, Journal of Wind and Structures, 8(2), pp. 89-106.
- [29] A. Oliveira and D.G. Preire. 1994. *Dynamical Modeling and Analysis of Aeolian Vibration of Single Conductors*, IEEE Transaction Power Delivery, 9(3), pp. 1685-1693 .
- [30] W. Kwon and H. Bang. 1997. *The Finite Element Method Using MATLAB*, Boca Raton, FL: CRC Press.

- [31] D. Sauter and P. Hagdorn. 2002. *On the Hysteresis of Wire Cables in Stockbridge Damper*, International journal of non-linear Mechanics, 37(8), pp. 1453-1459.
- [32] A.Y. Shehata, A.A. ElDamatty and E. Savory. 2005. *Finite element analysis and design*, Department of Civil and Environment Engineering Western Ontario, 42(1), pp. 71-89.
- [33] D.J. Inman. 2001. *Engineering Vibration*, 2nd Ed. Prentice-Hall, N.J.
- [34] D. Dempse and H. White. 1996. *Winds Wreak Havoc on Lines*. Transmission and Distribution World, 48(6), pp. 32-37.